ISSN
2395-6992

International Journal of Engineering Research & Science

www.ijoer.com
www.adpublications.org

Volume-4! Issue-1! January, 2018 www.ijoer.com ! info@ijoer.com

Preface

We would like to present, with great pleasure, the inaugural volume-4, Issue-1, January 2018, of a scholarly journal, *International Journal of Engineering Research & Science*. This journal is part of the AD Publications series *in the field of Engineering, Mathematics, Physics, Chemistry and science Research Development*, and is devoted to the gamut of Engineering and Science issues, from theoretical aspects to application-dependent studies and the validation of emerging technologies.

This journal was envisioned and founded to represent the growing needs of Engineering and Science as an emerging and increasingly vital field, now widely recognized as an integral part of scientific and technical investigations. Its mission is to become a voice of the Engineering and Science community, addressing researchers and practitioners in below areas

Chemical Engineering	
Biomolecular Engineering	Materials Engineering
Molecular Engineering	Process Engineering
Corrosion Engineering	
Civil Engineering	
Environmental Engineering	Geotechnical Engineering
Structural Engineering	Mining Engineering
Transport Engineering	Water resources Engineering
Electrical Engineering	
Power System Engineering	Optical Engineering
Mechanical Engineering	
Acoustical Engineering	Manufacturing Engineering
Optomechanical Engineering	Thermal Engineering
Power plant Engineering	Energy Engineering
Sports Engineering	Vehicle Engineering
Software Engineering	
Computer-aided Engineering	Cryptographic Engineering
Teletraffic Engineering	Web Engineering
System Engineering	
Mathematics	
Arithmetic	Algebra
Number theory	Field theory and polynomials
Analysis	Combinatorics
Geometry and topology	Topology
Probability and Statistics	Computational Science
Physical Science	Operational Research
Physics	
Nuclear and particle physics	Atomic, molecular, and optical physics
Condensed matter physics	Astrophysics
Applied Physics	Modern physics
Philosophy	Core theories

Chemistry	
Analytical chemistry	Biochemistry
Inorganic chemistry	Materials chemistry
Neurochemistry	Nuclear chemistry
Organic chemistry	Physical chemistry
Other Engineering Areas	
Aerospace Engineering	Agricultural Engineering
Applied Engineering	Biomedical Engineering
Biological Engineering	Building services Engineering
Energy Engineering	Railway Engineering
Industrial Engineering	Mechatronics Engineering
Management Engineering	Military Engineering
Petroleum Engineering	Nuclear Engineering
Textile Engineering	Nano Engineering
Algorithm and Computational Complexity	Artificial Intelligence
Electronics & Communication Engineering	Image Processing
Information Retrieval	Low Power VLSI Design
Neural Networks	Plastic Engineering

Each article in this issue provides an example of a concrete industrial application or a case study of the presented methodology to amplify the impact of the contribution. We are very thankful to everybody within that community who supported the idea of creating a new Research with IJOER. We are certain that this issue will be followed by many others, reporting new developments in the Engineering and Science field. This issue would not have been possible without the great support of the Reviewer, Editorial Board members and also with our Advisory Board Members, and we would like to express our sincere thanks to all of them. We would also like to express our gratitude to the editorial staff of AD Publications, who supported us at every stage of the project. It is our hope that this fine collection of articles will be a valuable resource for *IJOER* readers and will stimulate further research into the vibrant area of Engineering and Science Research.

Mukesh Arora

(Chief Editor)

Board Members

Dr. S.R.Boselin Prabhu

Ph.D, Wireless Sensor Networks, M.E. Network Engineering, Excellent Professional Achievement Award Winner from Society of Professional Engineers Biography Included in Marquis Who's Who in the World (Academic Year 2015 and 2016). Currently Serving as Assistant Professor in the department of ECE in SVS College of Engineering, Coimbatore.

Dr. Maheshwar Shrestha

Postdoctoral Research Fellow in DEPT. OF ELE ENGG & COMP SCI, SDSU, Brookings, SD Ph.D, M.Sc. in Electrical Engineering from SOUTH DAKOTA STATE UNIVERSITY, Brookings, SD.

Zairi Ismael Rizman

Senior Lecturer, Faculty of Electrical Engineering, Universiti Teknologi MARA (UiTM) (Terengganu) Malaysia Master (Science) in Microelectronics (2005), Universiti Kebangsaan Malaysia (UKM), Malaysia. Bachelor (Hons.) and Diploma in Electrical Engineering (Communication) (2002), UiTM Shah Alam, Malaysia

Dr. D. Amaranatha Reddy

Ph.D.(Postdocteral Fellow,Pusan National University, South Korea), M.Sc., B.Sc. : Physics.

Dr. Dibya Prakash Rai

Post Doctoral Fellow (PDF), M.Sc.,B.Sc., Working as Assistant Professor in Department of Physics in Pachhuncga University College, Mizoram, India.

Dr. Pankaj Kumar Pal

Ph.D R/S, ECE Deptt., IIT-Roorkee.

Dr. P. Thangam

BE(Computer Hardware & Software), ME(CSE), PhD in Information & Communication Engineering, currently serving as Associate Professor in the Department of Computer Science and Engineering of Coimbatore Institute of Engineering and Technology.

Dr. Pradeep K. Sharma

PhD., M.Phil, M.Sc, B.Sc, in Physics, MBA in System Management, Presently working as Provost and Associate Professor & Head of Department for Physics in University of Engineering & Management, Jaipur.

Dr. R. Devi Priya

Ph.D (CSE),Anna University Chennai in 2013, M.E, B.E (CSE) from Kongu Engineering College, currently working in the Department of Computer Science and Engineering in Kongu Engineering College, Tamil Nadu, India.

Dr. Sandeep

Post-doctoral fellow, Principal Investigator, Young Scientist Scheme Project (DST-SERB), Department of Physics, Mizoram University, Aizawl Mizoram, India- 796001.

Mr. Abilash

MTech in VLSI, BTech in Electronics & Telecommunication engineering through A.M.I.E.T.E from Central Electronics Engineering Research Institute (C.E.E.R.I) Pilani, Industrial Electronics from ATI-EPI Hyderabad, IEEE course in Mechatronics, CSHAM from Birla Institute Of Professional Studies.

Mr. Varun Shukla

M.Tech in ECE from RGPV (Awarded with silver Medal By President of India), Assistant Professor, Dept. of ECE, PSIT, Kanpur.

Mr. Shrikant Harle

Presently working as a Assistant Professor in Civil Engineering field of Prof. Ram Meghe College of Engineering and Management, Amravati. He was Senior Design Engineer (Larsen & Toubro Limited, India).

Table of Contents

Two-Dimensional Numerical Simulation of Bed Level Variation around Vertical Wall Bridge Abutments

Evangelia D. Farsirotou

Department of Civil Engineering T.E., Faculty of Applied Sciences, Technological Educational Institute of Thessaly, 411 10 Larissa, Greece.
Email: efars@teilar.gr

Abstract*—An accurate prediction of bed level variation and especially of the mechanism of local scour hole development around bridge abutments is of paramount importance, in river engineering, for a safe design of the construction. In the present research work, a two-dimensional, explicit, finite-volume numerical algorithm, which combines the hydrodynamic equations of viscous, unsteady, free-surface flow in rivers with the continuity equation for the conservation of sediment mass is used to simulate scour depth variation in the region of vertical wall abutments. The capabilities of the applied numerical model are demonstrated by comparing the computed results with available measurements of bed formation in the region of three orthogonal abutments, with different widths, normal to the flow direction. All the experimental results were conducted in a laboratory flume in Technological Educational Institute of Thessaly and scouring depths were obtained in the vicinity of each construction, for different inflow discharges and flow duration. Numerical simulation results of the maximum scour depth and of the developed scour whole area are satisfactorily compared with the experimental measurements. Comparisons show the accuracy and the validity of the applied two dimensional, movable bed numerical techniques.*

Keywords*—*Abutment, Local scour, Two-dimensional sediment transport model.

I. INTRODUCTION

The most common cause of bridge failures is from floods scouring bed material from around bridge foundations. Scour is the engineering term for the erosion caused by water of the soil surrounding a bridge foundation, piers and abutments. The basic mechanism causing local scour at piers or abutments is the formation of vortices at their base which removes bed material from around the base of the construction. Extensive research has been conducted to determine the depth and location of the scour hole that develops from the vortex that occurs at the abutment, and numerous abutment scour equations have been developed to predict this scour depth [5]. Numerous experimental investigations have been performed on the study of the flow, the bed level variation and mainly the scour mechanism in rivers and especially around bridge piers and abutments [9], [13], [7], [11], [2], [4] and others.

Besides experimental studies, several numerical investigations using Reynolds averaged Navier-Stokes equations of the flow have been developed to examine the flow structure in the hole of local scour and the development of local scour. Three-dimensional model provides the most realistic simulation of flow field under turbulence conditions adjacent to bridge piers and abutments. The development of the three-dimensional scour hole around a cylinder by solving simultaneously water flow field with sediment calculation was numerically simulated [12]. A 3-D time-accurate RANS solver with a nonlinear k-ε closure with wall functions was used to predict the scour evolution around an isolated vertical abutment (spur dike) in a channel [10]. Local scour depth around bridge pier and abutment, using the commercial solver Fluent with a user defined function for the calculation of channel bed elevation changes, was also numerically simulated [8].

The objective of this research work is to investigate bed formation in alluvial channels as well as in regions around vertical wall bridge abutments. For this purpose a two-dimensional, fully coupled hydrodynamic-sediment transport model was applied using an explicit finite-volume numerical technique [3]. The results of the model are verified by comparing them with available measurements of bed level variation around vertical wall abutments in uniform sediments under clear water scour conditions. The range of water discharge and width of the abutment was sufficient in order new and existing codes properly depict their capabilities against the satisfactorily compared results.

II. TWO DIMENSIONAL HYDRODYNAMIC AND SEDIMENT TRANSPORT MODEL

A two-dimensional, subcritical, supercritical or mixed flow regime, fully coupled, free-surface flow and movable bed numerical model was developed to simulate flow–field and bed morphology variations in alluvial channels. Vertically averaged free-surface flow equations in conjunction with sediment transport equation were numerically solved using an

explicit, finite-volume scheme in integral form. Hydrostatic pressure distribution was assumed throughout the flow field and incompressible flow was simulated with wind and Coriolis forces neglected. The two-dimensional, unsteady, free-surface flow in channels with sediment transport and movable bed was described by a system of non-linear, parabolic, partial differential equations using the flowing equations [6]:

The water continuity equation:

$$-\frac{\partial h}{\partial t}=\frac{\partial(hu)}{\partial x}+\frac{\partial(hv)}{\partial y} \tag{1}$$

The flow momentum equation in the longitudinal direction:

$$-\frac{\partial(hu)}{\partial t}=\frac{\partial\left(gh^2/2+hu^2\right)}{\partial x}+\frac{\partial(huv)}{\partial y}+gh\left(S_{ox}+S_{fx}\right)-\frac{\partial}{\partial x}\left[\nu_t\left(\frac{\partial(hu)}{\partial x}+\frac{\partial(hu)}{\partial x}\right)\right]-\frac{\partial}{\partial y}\left[\nu_t\left(\frac{\partial(hu)}{\partial y}+\frac{\partial(hv)}{\partial x}\right)\right] \tag{2}$$

The flow momentum equation in the transverse direction:

$$-\frac{\partial(hv)}{\partial t}=\frac{\partial\left(gh^2/2+hv^2\right)}{\partial y}+\frac{\partial(huv)}{\partial x}+gh\left(S_{oy}+S_{fy}\right)-\frac{\partial}{\partial x}\left[\nu_t\left(\frac{\partial(hu)}{\partial y}+\frac{\partial(hv)}{\partial x}\right)\right]-\frac{\partial}{\partial y}\left[\nu_t\left(\frac{\partial(hv)}{\partial y}+\frac{\partial(hv)}{\partial y}\right)\right] \tag{3}$$

The continuity equation of sediments :

$$-\frac{\partial\left[(1-p)z_b\right]}{\partial t}=\frac{\partial q_{sx}}{\partial x}+\frac{\partial q_{sy}}{\partial y} \tag{4}$$

where x and y represent the Cartesian co-ordinate positions in the longitudinal and transverse directions, respectively,

t is the time,

u and v are the average velocity components in the x and y directions,

h is the water depth,

g is the gravity acceleration,

ν_t is the kinematic viscosity (summation of molecular and eddy kinematic viscosity),

z_b is the bed elevation,

p is the sediment porosity,

q_{sx} and q_{sy} are the sediment discharges per unit width in the x and y directions,

$S_{0x}=\frac{-\partial z_b}{\partial x}$ and $S_{0y}=\frac{-\partial z_b}{\partial y}$ are the channel slopes and

S_{fx} and S_{fy} are the friction slopes which were defined as [6]:

$$S_{fx}=\frac{n^2u\sqrt{u^2+v^2}}{h^{4/3}} \text{ and } S_{fy}=\frac{n^2v\sqrt{u^2+v^2}}{h^{4/3}} \tag{5}$$

where n is the Manning's flow friction coefficient. In the two-dimensional numerical model the frictional resistance was expressed as function only of the bottom friction. The kinematic viscosity, ν_t, was defined in a similar way to the work of [14] as:

$$\nu_t=\frac{g}{C^2}h\sqrt{\left(u^2+v^2\right)} \tag{6}$$

where $C = \frac{h^{1/6}}{n}$ is the Chezy's, friction coefficient for free surface flow. The sediment discharge may be predicted by different knowing from the bibliography empirical bed-load formulae [3].

In the current numerical method the equations (1)-(4) were solved in an integral form and applied to a series of finite volumes with adjacent volumes sharing a common face. At the end of each time step Δt, the net flux into each elemental volume is zero, so that overall water mass flow and sediment transport are conserved, and the changes in momentum are equal to the forces imposed by the boundaries of the system. The flow equations were solved along with the sediment transport equation simultaneously using current values of flow and sediment variables, which have mutual interaction. Two convergence criteria were used and if they are not satisfied, then the iterations within the same time step continue. The above criteria require that: (a) the averaged over the flow field relative error based on the axial velocity drops below 10^{-6} and (b) the relative averaged change in sediment transport drops below 10^{-6}. As with all marching in time methods, the theoretical maximum stable time step Δt was specified according to the Courant–Friedrichs–Lewy (CFL) criterion[3].

III. BED LEVEL VARIATION AROUND VERTICAL WALL ABUTMENTS

Bridge abutments projecting into a river system produce bed level variation and deep scour holes in the region of the construction. Intense erosion develops upstream of the abutment and deposition of bed material occurs downstream of the obstruction. Local scour around abutments results from flow disturbances introduced by the presence of the structure. Experimental measurement tests were carried out in the Hydraulics Laboratory of Civil Engineering T.E. Department at the Technological Educational Institute of Thessaly [4]. An experimental flume of 6.0 m long and 0.078m wide was utilized. Three different geometries of orthogonal abutments with vertical walls were placed at the one side of the flume. The streamwise length of each abutment was equal to 0.10m and the lengths of the abutments transverse to the flow, abutment width, B, were constructed equal to 0.036m, 0.048m and 0.051m. The bottom of the tested experimental area was carefully covered with material, consisted of sand, producing a uniform layer of sediment of 0.15 m thickness. The used bed material had a mean diameter D_{50} of 2.0 mm, a specific weight S_g of 1.60 and was assumed to be uniform as the geometric standard deviation σ_g, computed by $(d_{84}/d_{16})^{0.5}$ was equal to 1.26. The experimental inflow discharges were equal to 0.0004 m^3/s, 0.0005 m^3/s, 0.0006 m^3/s, 0.0007 m^3/s, 0.0008 m^3/s and 0.00095 m^3/s.

In the two dimensional numerical simulation model, after a sensitivity analysis, the Manning's roughness coefficient n was estimated at 0.022 and the porosity p of the sediment bed layer was set equal to 0.4.The channel was carrying an initial uniform flow discharge, Q, equal to the experimental discharges with a uniform flow depth, h_0, presented in Table 1. The slope of the flume bed was initially set equal to zero. There was no sediment discharge entering the channel at the upstream end while at the downstream end, the bed elevation was free to change. The flow and geometry conditions resulted into subcritical throughout the flow field as the Froude number, Fr<1.0 (Table 1). A constant value of water depth at the downstream end was set for all $t \geq 0$. The time step Δt was computed according to the CFL criterion for stability.

TABLE 1
HYDRAULIC CONDITIONS

a/a	Q (m^3/s)	Fr	h_0 (m)
1	0.0004	0.28	0.0320
2	0.0005	0.33	0.0335
3	0.0006	0.37	0.0350
4	0.0007	0.38	0.0385
5	0.0008	0.41	0.0400
6	0.00095	0.47	0.0430

The unit sediment discharges q_{sx} and q_{sy} were numerically predicted using the empirical relation developed by Engelund and Hansen [1]:

$$q_{sx} = \frac{uC_{bx}h}{pS_g}$$

$$q_{sy} = q_{sx}\frac{u}{v}$$

where C_{bx} is the sediment concentration in the x-direction as:

$$C_{bx} = \frac{50\, S_g u u_*^2}{h g^2 D_{50} (S_g - 1)^2}$$

and the shear velocity $u_* = \sqrt{gh\sqrt{(S_{fx}^2 + S_{fy}^2)}}$.

The validity of several empirical bed load relations, available in the model, was tested and comparisons between experimental measurements show that the Engelund and Hansen formula gives accurate results. Direct comparisons between two- dimensional numerical simulation predictions and experimental measurements of scour depth variation are shown in Fig. 1(a)-(f), along the flow line located at a constant distance of 0.005m to the streamwise face of the abutment parallel to the flow direction, in an area extending 0.06 m upstream to the abutment to 0.06 m downstream to it, for abutment width B=0.036 m, for different inflow discharges and after flow duration t=6 min and t=30 min. The abutment construction starts at an axial distance x=0.06 m to x=0.16 m. Fig. 2(a)-(f) and 3(a)-(f) present comparisons of scour depth variation, in the region of the abutment, for different inflow discharges and for abutment widths B=0.048 m and B=0.051 m, respectively. The scour hole development and the maximum scour depth evolution in the region of each abutment are adequately predicted by the numerical technique for all discharges. High viscous effects in the regions immediately upstream and downstream to the abutment give rise to substantial differences between predictions and measurements. It is in these regions that high viscous effects combined with three-dimensional flow restrict a two dimensional model to predict exactly flow behavior and the maximum scour depth value. Maximum measured scour depths along the abutment are under predicted by the current method and this is the rule for all results. Erosion upstream of the abutment and deposition of the sediments at the downstream region, along the streamwise face of the abutment, which is the area of the maximum scour depths, are satisfactorily numerically simulated. The impact of flow duration, flow discharge and width of the abutment, normal to the flow direction, on scour depth variation was accurately predicted by the two-dimensional numerical model.

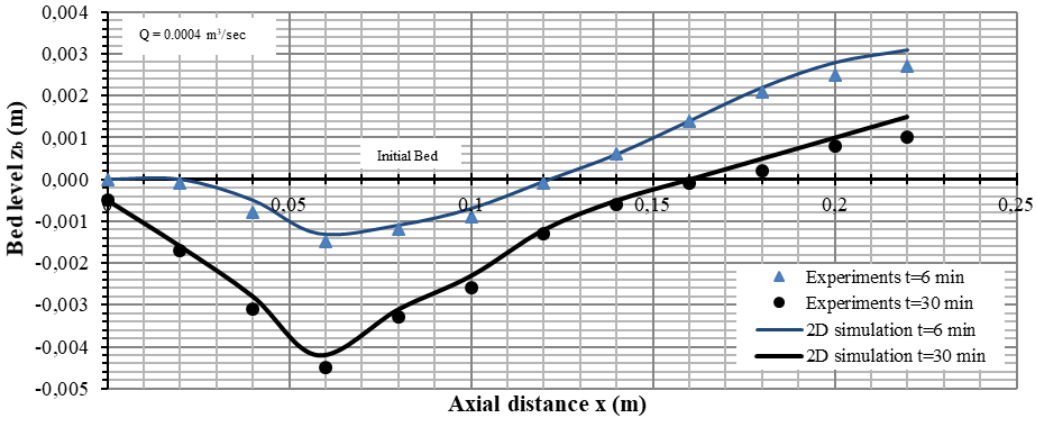

(a)

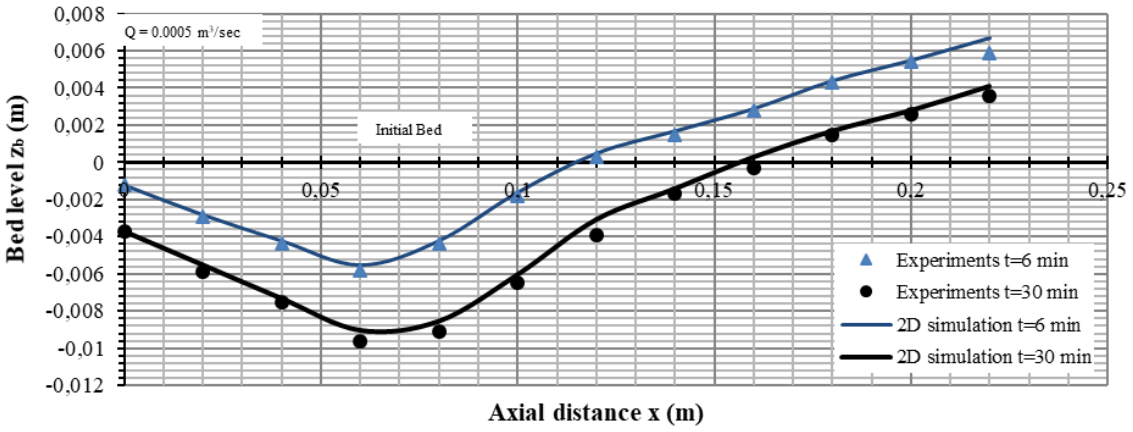

(b)

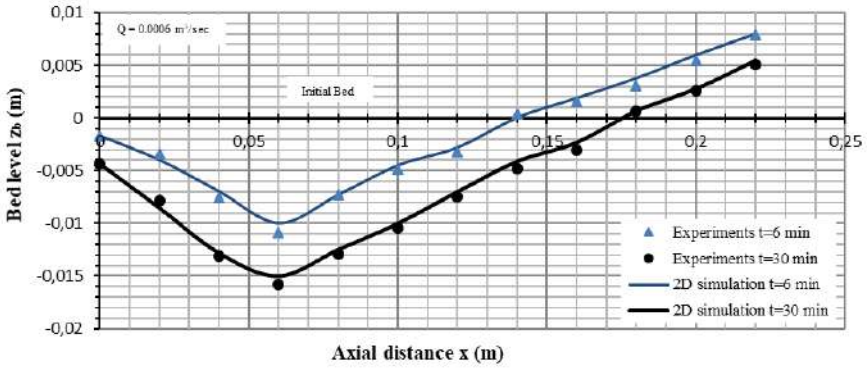

(c)

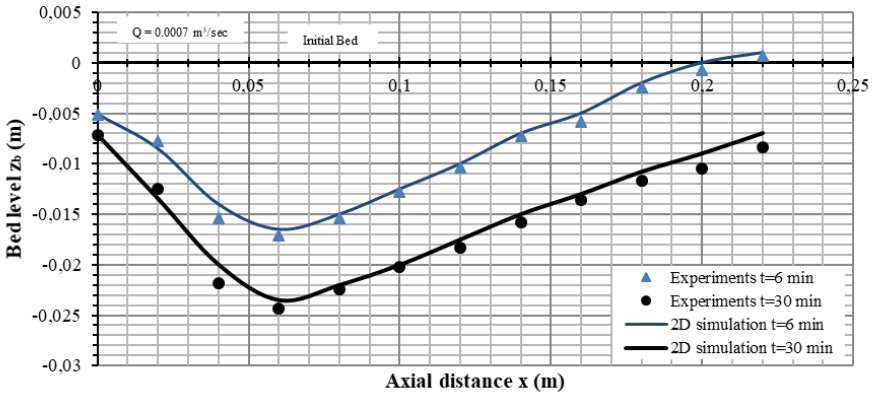

(d)

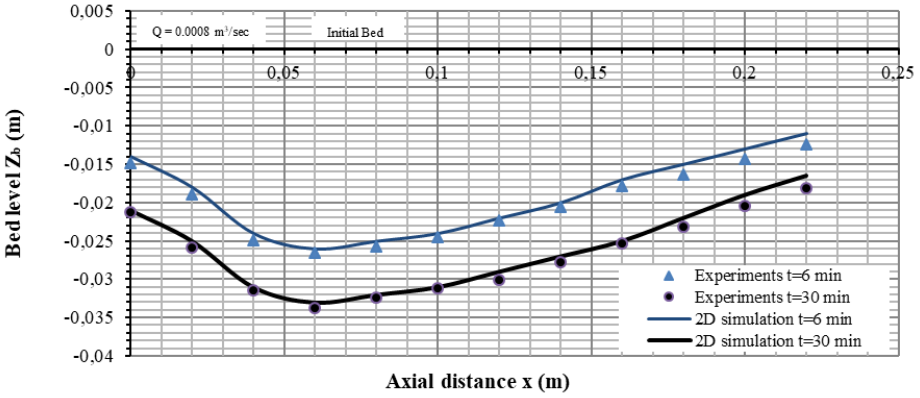

(e)

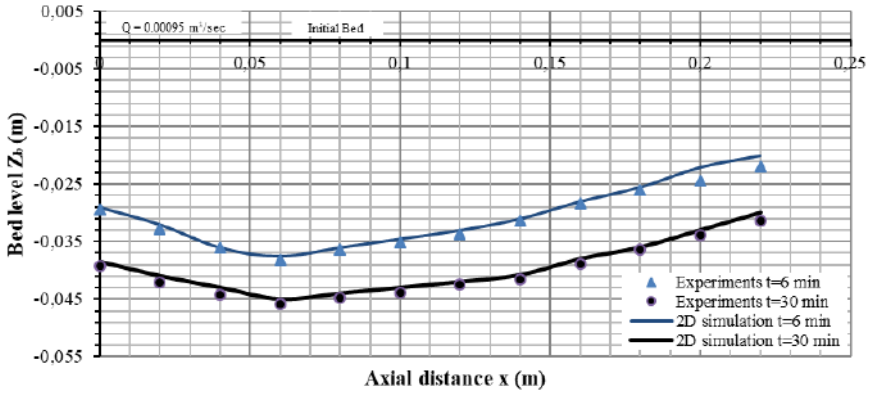

(f)

FIG. 1. COMPARISON BETWEEN COMPUTED AND MEASURED BED LEVEL VARIATION ALONG THE STREAMWISE FACE OF THE ABUTMENT, FOR B=0.036 M AND DIFFERENT INFLOW DISCHARGES

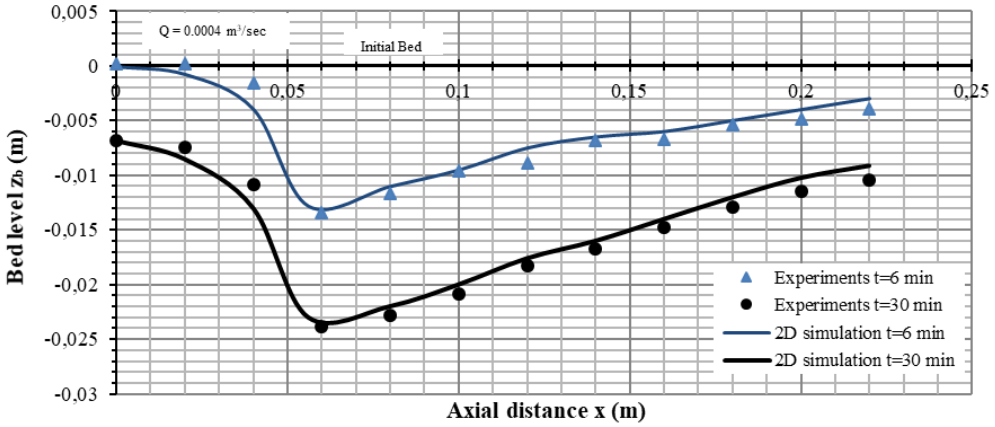
Q = 0.0004 m³/sec
Initial Bed
Bed level zb (m)
Axial distance x (m)
Experiments t=6 min
Experiments t=30 min
2D simulation t=6 min
2D simulation t=30 min

(a)

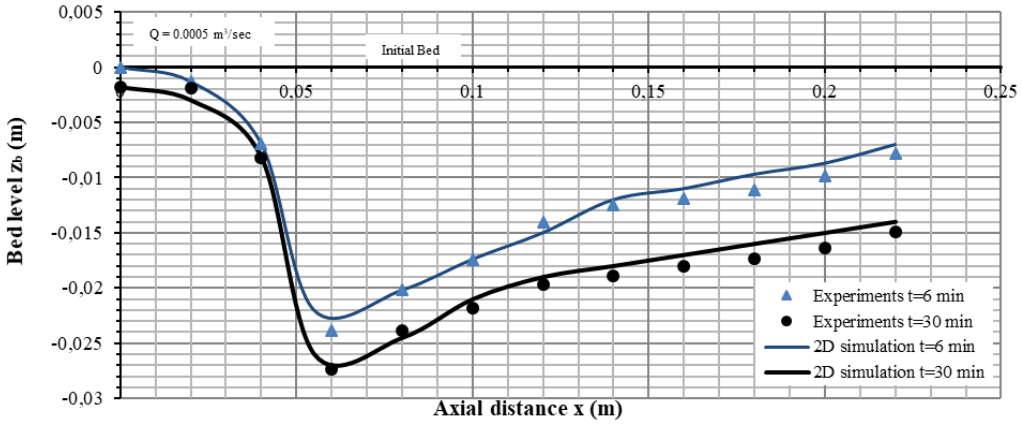
Q = 0.0005 m³/sec
Initial Bed
Bed level zb (m)
Axial distance x (m)
Experiments t=6 min
Experiments t=30 min
2D simulation t=6 min
2D simulation t=30 min

(b)

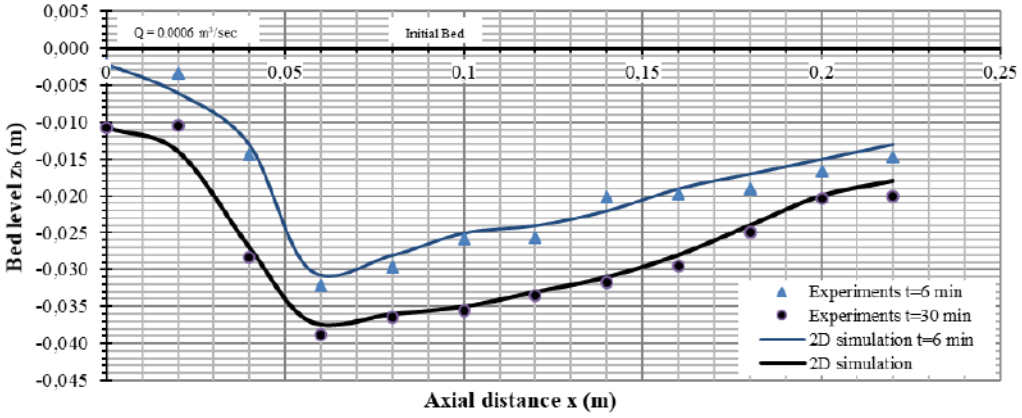
Q = 0.0006 m³/sec
Initial Bed
Bed level zb (m)
Axial distance x (m)
Experiments t=6 min
Experiments t=30 min
2D simulation t=6 min
2D simulation

(c)

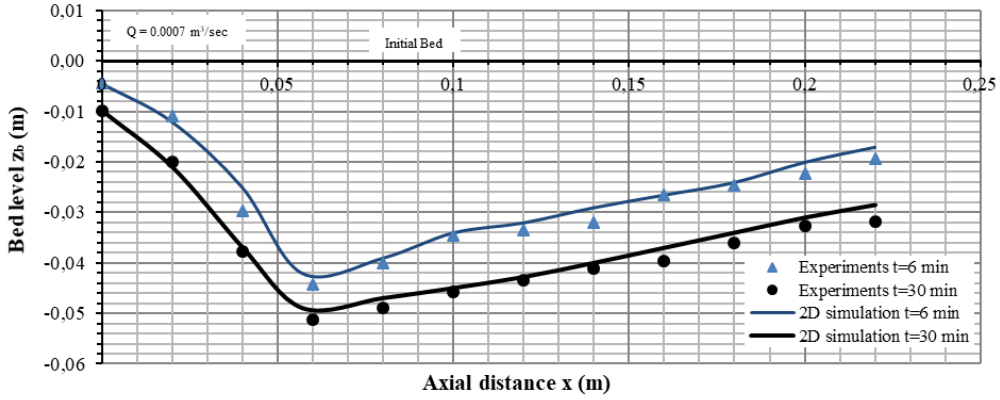
Q = 0.0007 m³/sec
Initial Bed
Bed level zb (m)
Axial distance x (m)
Experiments t=6 min
Experiments t=30 min
2D simulation t=6 min
2D simulation t=30 min

(d)

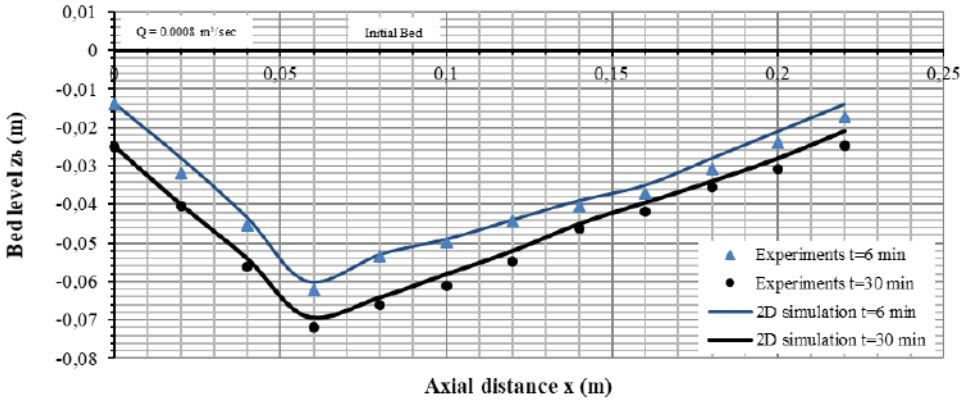

(e)

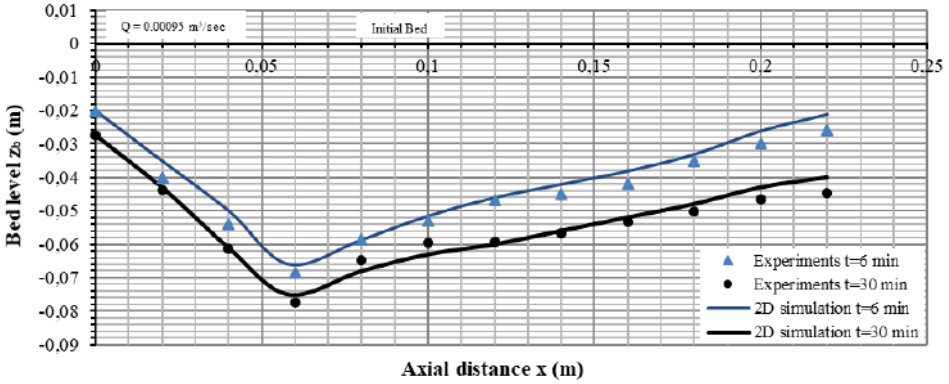

(f)

FIG. 2. COMPARISON BETWEEN COMPUTED AND MEASURED BED LEVEL VARIATION ALONG THE STREAMWISE FACE OF THE ABUTMENT, FOR B=0.048 M AND DIFFERENT INFLOW DISCHARGES

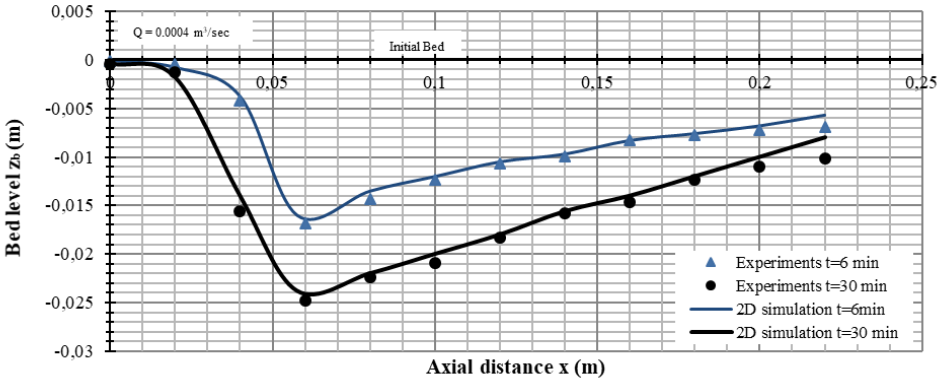

(a)

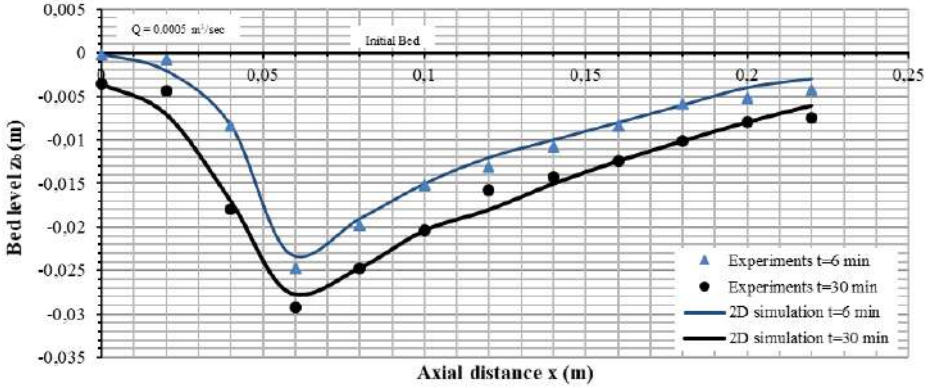

(b)

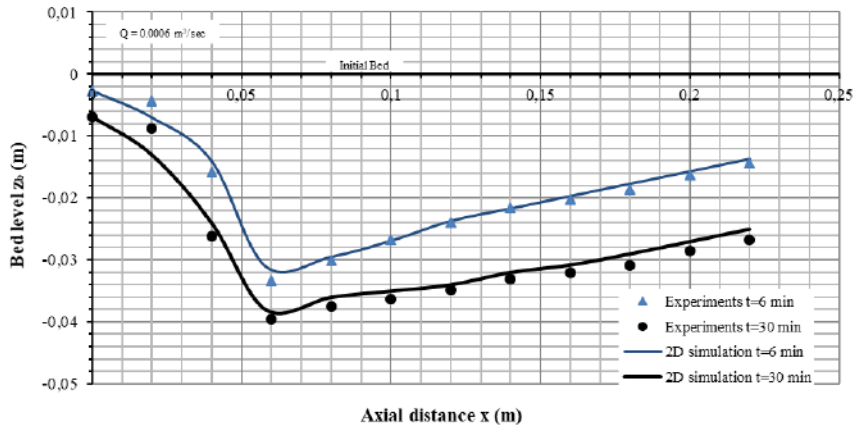

(c)

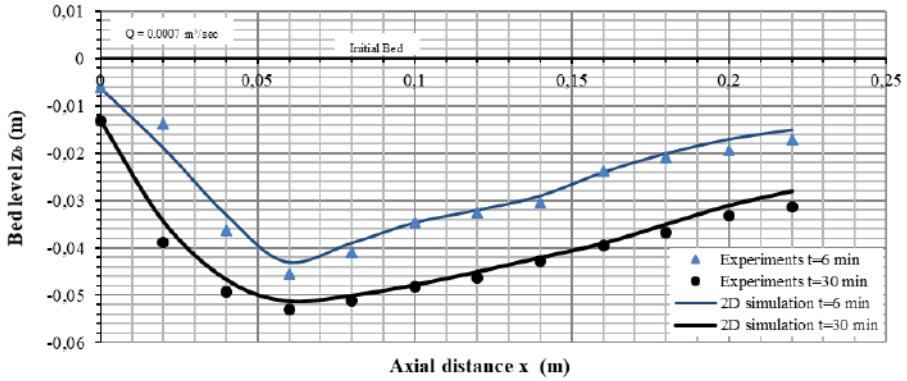

(d)

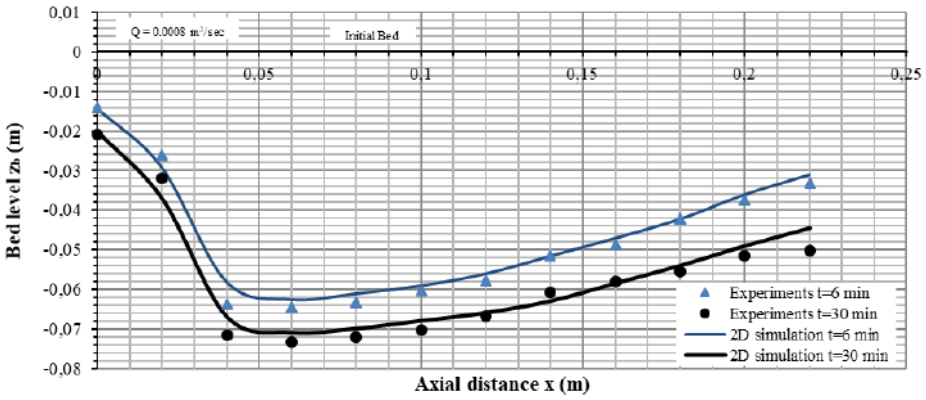

(e)

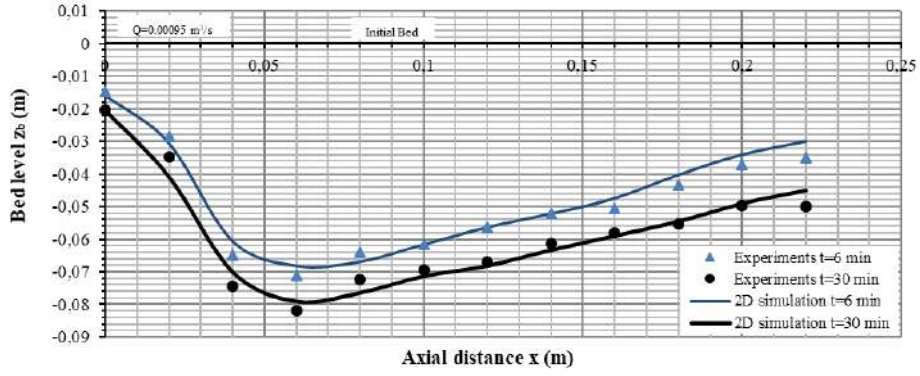

(f)

FIG. 3. COMPARISON BETWEEN COMPUTED AND MEASURED BED LEVEL VARIATION ALONG THE STREAMWISE FACE OF THE ABUTMENT, FOR B=0.051M AND DIFFERENT INFLOW DISCHARGES

IV. CONCLUSION

A two-dimensional, explicit, finite-volume numerical model has been applied to simulate bed level variation and maximum scour around bridge abutments in alluvial channels. The numerical predictions were backed by available experimental measurements and a sensitivity analysis was performed in order to test which is the most convenient empirical bed-load formula for the current hydraulic and sediment transport conditions. The applied numerical technique, directly coupling hydrodynamic and bed morphology equations, proved to be computational time consuming. It is stable, reliable, and accurate and can be applied to problems with complicated geometries. The numerical technique itself turned out to be flexible concerning its response to handle rapid changes of sediment transport at the boundaries and especially at regions of bridge constructions. Comparisons between computed results with measurements of scour depths at the region of vertical-wall abutments, in uniform sediments under clear water scour conditions, are graphically presented and can be used by other researchers to assist in the development of new and the refinement of existing codes for computing river bed morphology variations.

REFERENCES

[1] F. Engelund and E. Hansen, "A monograph on sediment transport in alluvial streams", Teknish Vorlag, Copenhagen, 1967.

[2] S. Coleman, Chr. Lauchlan and B. Melville, "Clear water scour development at bridge abutments", Journal of Hydraulic Research, vol. 41(5), 2003, pp. 521-531.

[3] E. Farsirotou, V. Dermissis and J. Soulis, "A numerical method for two-dimensional bed morphology calculations" Journal of Computational Fluid Dynamics, vol. 16(3), 2002, pp. 187-200.

[4] E. Farsirotou and N. Xafoulis, "An experimental study of local scour depth around bridge abutments", International Journal of New Technology and Research, vol. 3(9), 2017, pp. 01-10.

[5] Federal Highway Administration U.S. Department of Transportation, "Evaluating Scour at Bridges", Publication No. FHWA-HIF-12-003, 2012.

[6] Kassem and M. Chaudhry, "Comparison of coupled and semi-coupled numerical models for alluvial channels", Journal of Hydraulic Engineering, ASCE, vol. 124, 1988, pp. 794-802.

[7] J. Kandasamy and B. Melville, "Maximum local scour depth at bridge piers and abutments", Journal of Hydraulic Research, vol. 36(2), 1998, pp. 183-198.

[8] S. Liu, Yi Yang and X. Wu, "Simulations of local scour around a cylindrical bridge pier and a semicircular abutment using unsteady k-ε model combined with σ- Grid", The Open Civil Engineering Journal, vol. 11(613), 2017, pp. 598-614.

[9] B. Melville, "Local scour at bridge abutments", Journal of Hydraulic Engineering, vol. 118(4), 1992, pp. 615-631.

[10] N. Nagata, T. Hosoda, T. Nakato and Y. Muramoto, "Three-dimension numerical model for flow and bed deformations around river hydraulic structures", Journal of Hydraulic Engineering, vol.131(12), 2005, pp. 1074-1087.

[11] G. Olivet and W. Hager, "Temporal evolution of clear water pier and abutment scour", Journal of Hydraulic Engineering, vol. 128(9), 2002, pp. 811-820.

[12] N. Olsen M. and Kjellesvig M., "Three-dimensional numerical flow modeling for estimation of maximum local scour depth", Journal of Hydraulic Research, vol. 36(4), 1998, pp. 579-590.

[13] Ricky T. Kw An and B. Melville, "Local scour and flow measurements at bridge abutments", Journal of Hydraulic Research, vol. 32(5), 1994, pp.661-673.

[14] B. Ylistiyanto, Y. Zech and W. Graf, "Flow around a cylinder: shallow-water modeling with diffusion-dispersion", Journal of Hydraulic Engineering, ASCE, vol.124, 1998, pp. 419-429.

Material characterisation and parameter effects on bulk solid dissolution rate of paracetamol in a stirred tank vessel using an in situ UV-ATR probe

Arabella McLaughlin[1*], John Robertson[2] and Xiong-Wei Ni[3]

[*1,3]EPSRC Centre for Continuous Manufacturing and Crystallisation (CMAC), Centre for Oscillatory Baffled Reactor Applications (COBRA), School of Engineering and Physical Science, Heriot-Watt University, Edinburgh, EH14 4AS, UK
[2]EPSRC Future Continuous Manufacturing and Advanced Crystallisation Research Hub, University of Strathclyde, Technology and Innovation Centre, 99 George Street, Glasgow, G1 1RD, U.K.
[*]the corresponding author, tel: 00441314513590

Abstract— *The progress from batch to continuous manufacture of pharmaceuticals has highlighted the requirement for dosing solid feed material directly, efficiently and accurately into continuous flow systems. Solids are currently dissolved in batch vessels before feeding into a flow system. This study focuses on gaining scientific understanding on rate kinetics of solid dissolution and parameters affecting solid dosing in current batch systems as a starting point; the knowledge gained will inform future continuous solid dosing work. Paracetamol was the model compound and the mixtures of water/ IPA the solvent systems. An in situ UV spectrometer was used to quantify the concentration of solute in solution during dissolution. In this paper, we present the dissolution kinetics results from a parametric study of effects of temperature, solvents, mixing and particle sizes on dissolution characteristics in a stirred tank vessel. The dissolution profiles from our system are similar to that of published work, with the fastest kinetics for the micronised particles, albeit problematic when dosing as a single shot. Dissolution rate is increased with increasing temperature, solvent content (solubility), mixing intensity and decreasing particle size.*

Keywords— Dissolution, Solid dosing, Continuous Work up, Batch manufacturing, Continuous Pharmaceutical Manufacture, Stirred tank reactor, UV Spectrometry.

I. INTRODUCTION

Traditionally batch manufacture is used to produce pharmaceutical products from synthesis and work up to reaction and from isolation to tableting. Although the introduction of continuous manufacture and crystallisation into the pharmaceutical industry has been gathering momentum (1, 2), work up technology and inventory in pharmaceutical manufacture still remain batch operation (3); "charging solids into a tank of solvent and leaving it stirred for hours" has been the norm in industrial work up operation (4-6) that are too large to use and too inflexible to change for continuous crystallisation (7, 8). As a result, there has generally been a lack of scientific understanding in terms of solid dissolution, dosing and associated operations in batch processes (9, 10). This is also reflected by the very limited publications in this area, as academic researchers largely regard the work up being a technical problem. With the realization of benefits of consistent crystal properties that continuous crystallisation has brought about (11-13), investigations on continuous work up have been identified as an unmet need, this work is one of the earliest research in this area. The ultimate purpose is to be able to feed solute solid particles and the selected solvent concurrently, accurately and continuously into a plug flow system for unit operations; this would require knowledge and understanding of dissolution kinetics, mechanisms and parameters affecting these. The current work addresses this very subject.

Dissolution research began in 1897 when Noyes and Whitney (14) conducted the first dissolution experiments of two sparingly soluble compounds, benzoic acid and lead chloride; noticed that the rate of dissolution was proportional to the difference between the instantaneous concentration, C at time t, and the saturation solubility Cs. The authors attributed the mechanism of dissolution to a thin diffusion layer which was formed around the solid surface and through which the molecules diffused to the bulk aqueous phase.

Higuchi (15) reviewed the diffusion layer model that considered interfacial transport was the limiting step due to a high activation energy level. Danckwerts (16) proposed an alternative mechanism by constantly renewing macroscopic packets of solvent to reach the solid surface and absorb molecules of solute, delivering them to the solution. In the 1950s the pharmaceutical sciences used the concept of in vitro dissolution when it became clear that the dissolution rate was the limiting step. This led to the development of the basket-stirred-flask United States Pharmacopeia (USP) apparatus 1, as an

official dissolution test kit. Since then the factors affecting the dissolution rates in USP apparatus were studied extensively and the degree of agitation, solubility and the surfaces exposed in the solvent were identified as the important factors in determining dissolution; while temperature was previously identified as a factor in dissolution rate (17) in bulk solids dissolution. All of the above factors will be investigated in this study with paracetamol in water/ IPA as the model system.

The solubility of paracetamol in water- propan-2-ol mixtures was evaluated by Hojjati and Rohani (18) using an ATR-FTIR method, in comparison with measurements taken gravimetrically. The results were in good agreement, which also agrees with data from other literature. Granberg and Rasmuson (19) used a gravimetric technique to determine the solubilities of paracetamol in 26 different pure solvents including propan-2-ol and water over the temperature range from -5 to +30°C. Fujiwara et al (20) measured the solubility of paracetamol in water from 20 to 50°C using in situ ATR-FTIR probe and chemometric techniques. The agreement among the aforementioned solubilities was good. The solubility data for paracetamol in water- propan-2-ol mixtures (18) is used in this study and verified using a gravimetric technique.

While solubility was measured and reported in previous research work, dissolution kinetics were largely ignored, but it is the kinetics that governs the dissolution process. This work focuses on a parametric study of the effects of temperature, solvent composition, mixing intensity and particle size on dissolution rates in a stirred tank vessel (STV). Solute concentration was measured using an in situ ATR-UV probe, were extracted to obtain dissolution kinetics. This work serves as a baseline for developing dissolution of solids in a continuous flow system.

II. EXPERIMENTAL PREPARATION AND PROCEDURES

2.1 Materials

Three grades (micronised, powder and granular) of paracetamol (99% purity) were supplied by Mallinckrodt Chemical Limited (UK). Table 1 shows the characteristics of the three grades.

TABLE 1
PARTICLE SIZES OF THREE TYPES OF PARACETAMOL

	40 Mesh (425µm)	60 Mesh (250µm)	80 Mesh (180µm)	100 Mesh (150µm)	400 Mesh (38µm)
Micronised				99% min	95% min
Powder	1% max	7% max		5% - 19%	
Granular	1% max	64% min	10% max		

Propan-2-ol (IPA) (>99.5% purity) was supplied by Sigma-Aldrich (Gillingham, UK). Deionised water was produced using the in-house Millipore Milli-Q system.

2.2 Solubility Measurement

Three different solvent systems were used in this study: 100% deionised water, 80% deionised water: 20% IPA, and 20% deionised water: 80% IPA. Solubility of paracetamol has been determined by a gravimetric method and compared to previously published work (18). In the gravimetric technique, a known weight of paracetamol was added to a conical flask containing 100g of solvent mixture. The flask was placed in a water bath to maintain the temperature and stirred until all solids had dissolved. Further known weights of paracetamol were added until no further dissolution had occurred. The excess solid was filtered off, dried and weighed to determine the saturation concentration. Each measurement was repeated three times.

2.3 Particle Size Analysis

The mean particle size and particle size distributions were analysed by a Mastersizer 3000™ (HYDRO, Malvern) device and given in Table 2 and Figure 1.

TABLE 2
PARTICLE SIZE DISTRIBUTION OF THREE TYPES OF PARACETAMOL

	Dx (10) (µm)	Dx (50) (µm)	Dx (90) (µm)
Micronised	11	26.1	51.4
Powder	12.6	44.9	124
Granular	263	374	516

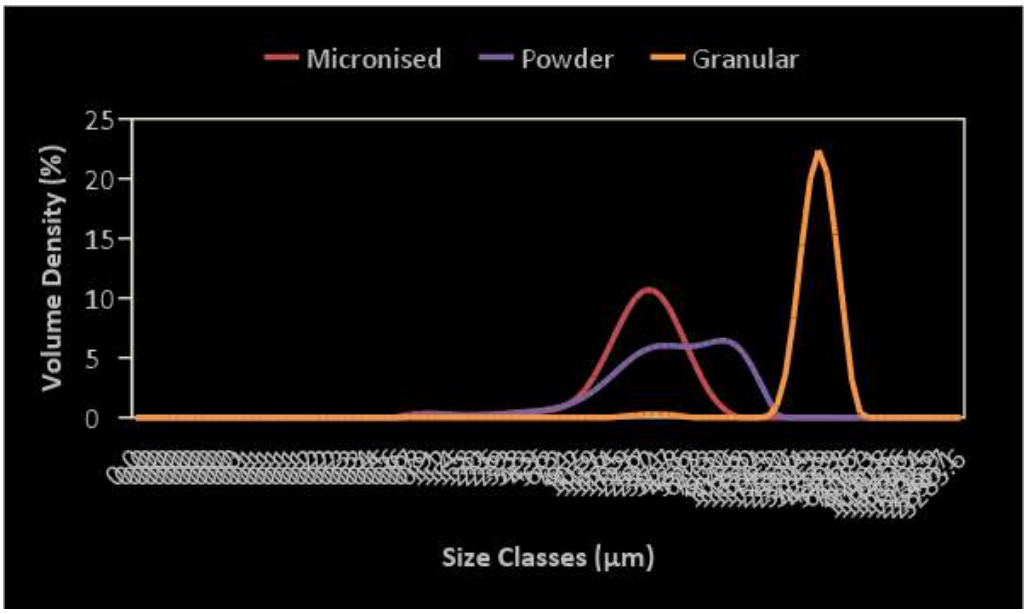

FIGURE 1: PARTICLE SIZE DISTRIBUTION OF PARACETAMOL - MICRONISED, POWDER, GRANULAR

Scanning Electron Microscope (SEM) images (provided by Remedies Project) for each grade of paracetamol are given in Figure 2.

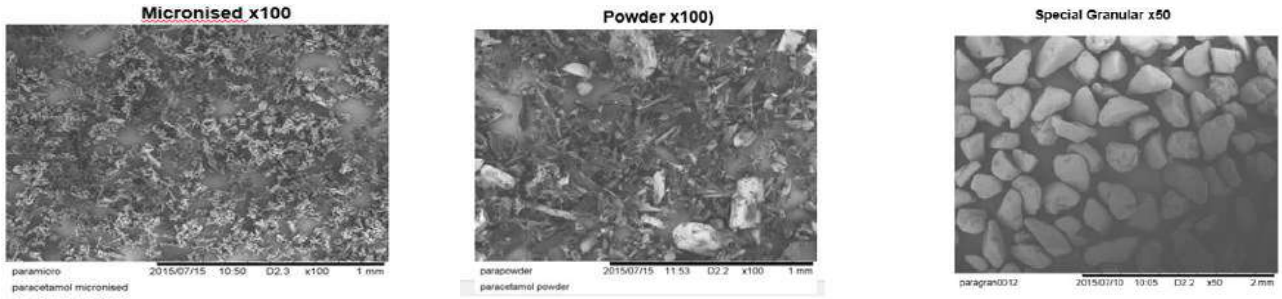

FIGURE 2: SEM IMAGES OF PARACETAMOL MICRONISED PARTICLES, POWDER AND GRANULAR

2.4 Surface area

SMS-iGC 2000 from Surface Measurement Systems Ltd was used to measure the surface area and surface energy of each of the paracetamol grades. Approximately 1 g of each sample was packed by gentle tapping into a 4 mm ID silanised glass column capped with glass wool in each end. Samples were pre-conditioned at 25°C and 0% RH for 1 hour under flowing helium prior to measurements. BET surface area was determined using octane as the vapour probe. The Dorris-Gray calculation method (21) and the peak centre of mass were used to analyse iGC- SEA results to identify the wettability, hydrophilicity and surface energy.

2.5 STV

The STV was a jacketed glass vessel of 1 litre in volume, with a PTFE four-blade pitched impeller to generate mixing. The impeller was attached to an overhead motor to control the rotation speeds. The vessel was fitted with a 5 port PTFE lid which enables the insertion of PAT probes and the dosing funnels. Different temperatures within the vessel were achieved by controlling the jacket temperature using a water bath (Grant Instruments GP 200/R2). UV-ATR, turbidity and temperature (PT100) probes (CrystalEyes system from HEL, UK) were inserted into the vessel to monitor and record the solute concentration, the cloudiness and temperatures of the solution during dissolution. The system was interfaced with a Carl Zeiss MC600 Spectrometer and PC for real-time display, logging and data analysis. The UV spectra were collected continuously over the spectral range of 220 – 280nm, using Aspect Plus software. The schematic illustration of the STV is given in Figure 3.

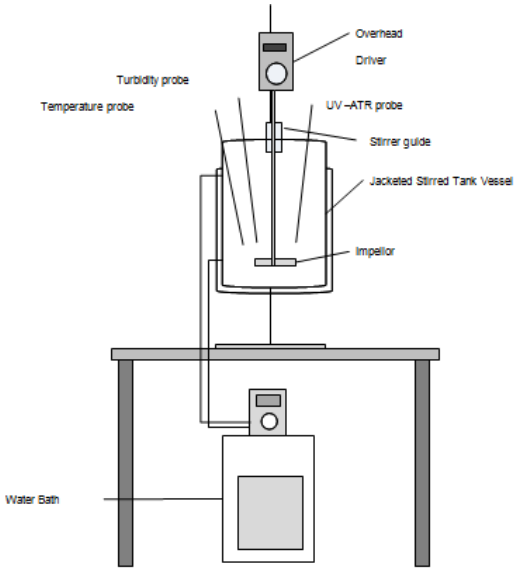

FIGURE 3: SCHEMATIC ILLUSTRATION OF STV SET-UP

For each experimental run, the volume of one litre of solvent was added to the STV and heated/cooled to the desired temperature (20°C, 30°C, or 40°C). The dissolution was carried out isothermally. A specified amount (see Supplementary Material) of technical grade paracetamol was weighed using an electronic balance and was poured into the vessel using a funnel, to minimise loss. It was decided to use a solid loading of 95% of the solubility, in order to obtain an undersaturated solution. The solution was held at temperature and stirred under a fixed rotational speed until dissolution was complete. Dissolution experiments were carried out to determine the parameter effects of temperature (20 ˚C, 30 ˚C, 40 ˚C), mixing intensity (250rpm, 500rpm, 750rpm), solvent composition (water/ IPA mixtures), and particle size (micronised, powder, granular) on the dissolution rate.

III. RESULTS AND DISCUSSION

3.1 Dissolution Studies in STV

3.1.1 Calibration for concentration measurement

To quantify the solute concentration in the solution, calibration graphs were generated from known quantities of paracetamol in solvents based on the Beer's Law where a linear relationship is obeyed between the absorbance and the concentration of an absorbing species. A maximum absorbance peak can be seen at 247nm (for deionised water) indicating that the paracetamol has dissolved (see Figure 4). Calibration curves were generated for each solvent system at each temperature in this parametric study. The data show that the temperature dependence of UV spectra is weak in the range of experimental temperatures. This indicates that temperature should not significantly influence solution concentration measurement which supports previously published work by Zhang et.al. (22). Once the calibration curve has been established, each individual sample can be analysed.

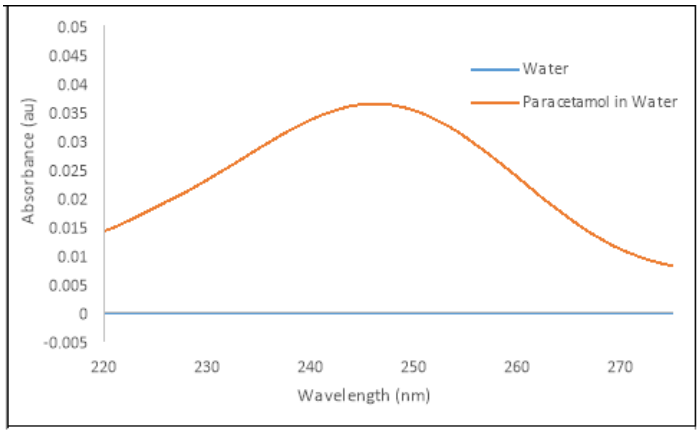

FIGURE 4 UV SPECTROSCOPY OF PARACETAMOL DISSOLUTION IN WATER

3.1.2 Dissolution Kinetics

The dissolution rate kinetics were evaluated by the slopes of the plot of concentration of dissolved paracetamol as a function of time as shown in Figure 5. We see that the slope (i.e. the rate) is relatively steep initially and then levels off monotonously as t increases (see Figure 5). This is the typical behaviour of solid particles whose size and surface area gradually decrease as dissolution proceeds which is called the attrition mechanism (23). The curve flattens off as we are running out of material and dissolution is complete. Under highly under saturated conditions, all dissolution surface sites actively participate in the dissolution reaction, while it is only certain faces of the materials with lower activation energies of dissolution that contribute to the dissolution process as the solution becomes more saturated, as demonstrated by Guidry and Mackenzie (24) for alkali feldspars.

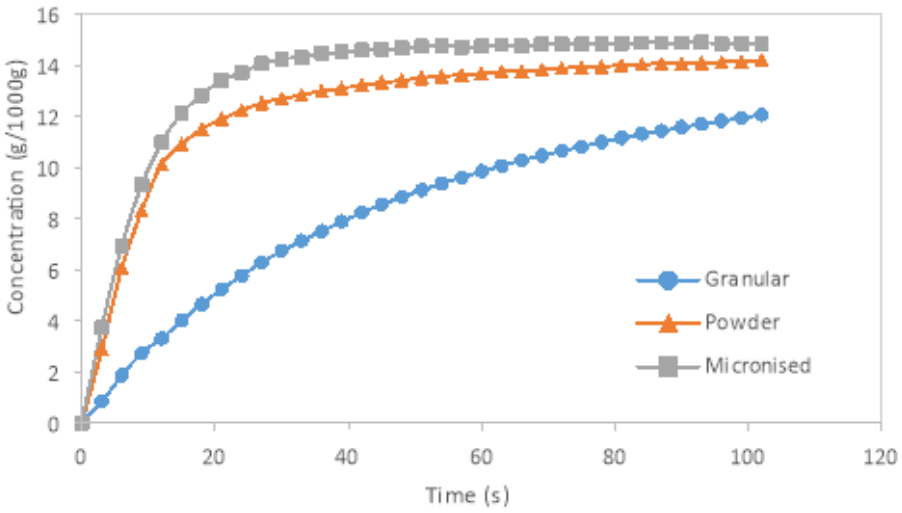

FIGURE 5: DISSOLUTION PROFILE OF PARACETAMOL IN WATER (Temperature = 30°C, Mixing Speed = 750 rpm)

For comparative purposes, the maximum dissolutions observed at the initial dissolution times, i.e. only the rising parts of the dissolution profiles, were used to extract dissolution kinetics, as

$$dC/dt = k(Cs - C)$$

where C is the concentration of paracetamol (g/1000g) at the dissolution time t, Cs is the saturation concentration of paracetamol (g/1000g) and k is the rate constant of dissolution (14).

3.2 Effect of Particle Size

Figure 6 shows the dissolution profiles for the three materials in water at a fixed temperature; for comparison purposes, the time taken to dissolve 90% of the paracetamol concentration was used for each experiment. The granular material took 201 seconds to dissolve and was the slowest; the powder dissolved faster than the granular particles, taking 45 seconds, although the dissolution slowed considerably at near equilibrium concentrations. The micronised material dissolved very fast where a full dissolution was obtained within 21 seconds.

Note that both the micronised and powder particles were difficult to dose due to static force and prone to stick to the walls of the dispensing funnel and sides of the vessel when dispensing in one shot, while dosing granular material was trouble free without loss of material, as such the total concentration of paracetamol dissolved was slightly less for micronised and powder than for granular particles, e.g. 15.6 g l^{-1} (granular), 14.8 g l^{-1} (powder) and 14.8 g l^{-1} (micronised). The data has therefore been normalised (see Figure 6) prior to analysis of the dissolution kinetics.

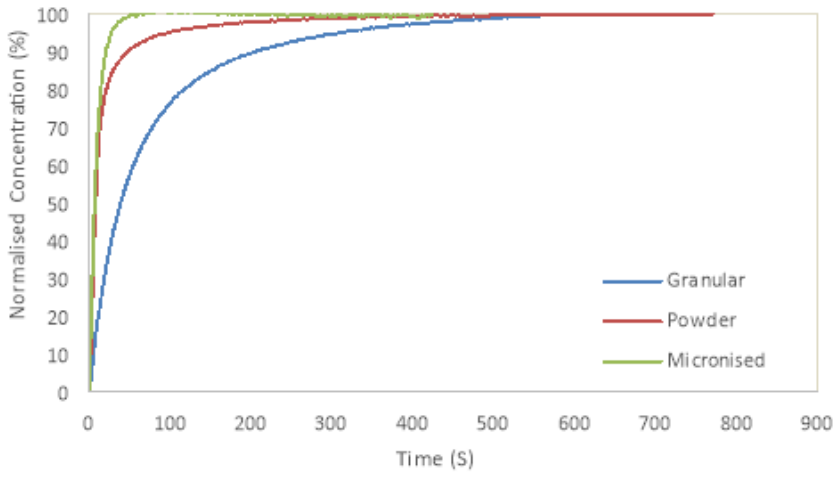

FIGURE 6 NORMALISED DATA FOR DISSOLUTION PROFILE OF PARACETAMOL IN WATER (Temperature = 30°C, Mixing Speed = 750 rpm)

First order kinetics can be seen in Figure 7 and summarised in Table 3, which agrees with previously published work by Lee T. et.al, 2013 (25).

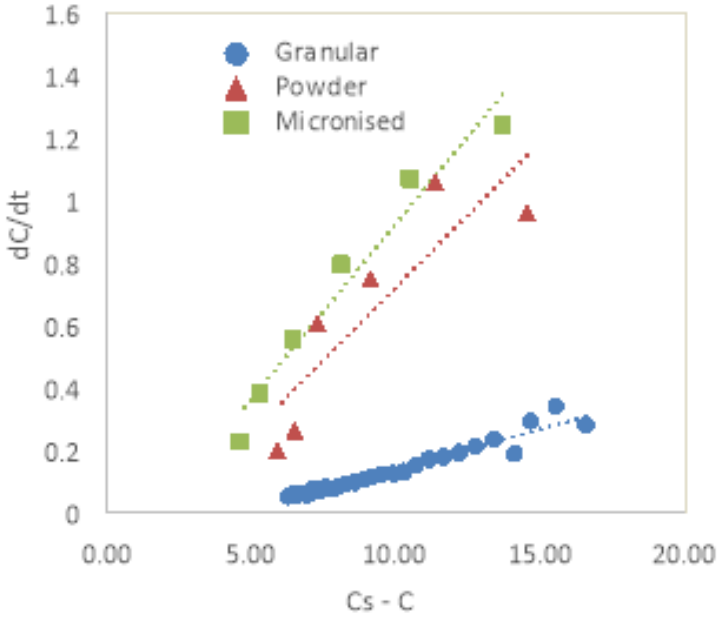

FIGURE 7: KINETIC EVALUATION

TABLE 3
DISSOLUTION RATE CONSTANTS OF PARACETAMOL

Particle Size	k (s^{-1})
Granular	0.026
Powder	0.093
Micronised	0.112

The results from our system are similar to that of literature (25), with the steepest slope for the smallest particles.

3.3 Effect of Solvent Composition

The dissolution profiles for the three solvent systems as a function of time are illustrated in Figure 8 for granular paracetamol only.

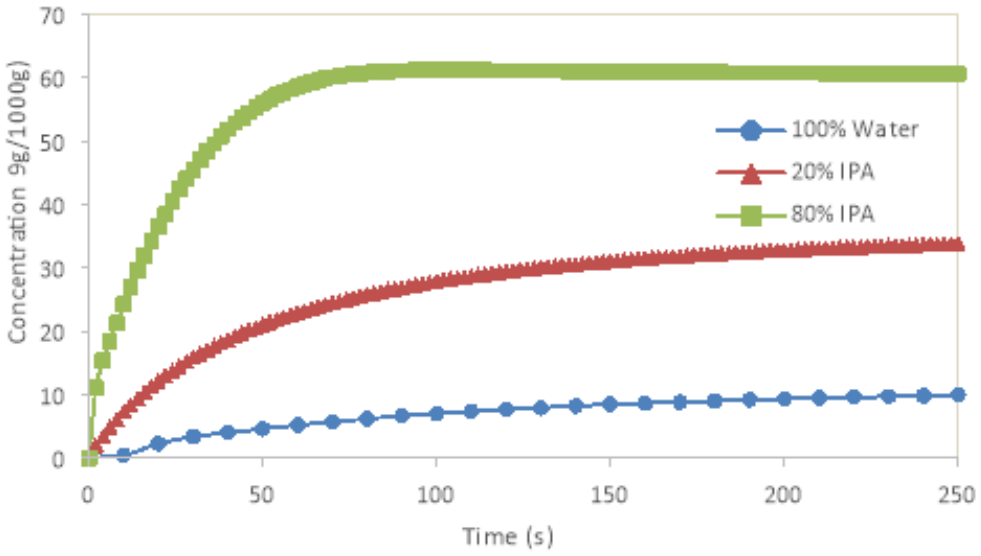

FIGURE 8 DISSOLUTION PROFILE OF GRANULAR PARACETAMOL IN WATER/IPA MIXTURES (Temp=20°C, Mixing Speed = 750 rpm)

The higher the IPA content and hence the higher the solubility, then the faster the dissolution rate, as highlighted in Table 4.

TABLE 4
TIME TO DISSOLUTION OF GRANULAR PARACETAMOL IN VARYING SOLVENT COMPOSITIONS

	Dissolution Time (s)
100% Water	440
20% IPA	18
80% IPA	2

Paracetamol has a simple molecular structure showing polar property. Barra and et al, (27) studied the hydrogen bonding ability of paracetamol as a donor and an acceptor. Water is very polar, while IPA is less polar; lower polarity of IPA reduces the interfacial tensions and surface tension between the solute and solvent; the solute moves faster through the diffusion layer of the solvent, hence increasing the dissolution rate (see Table 5).

TABLE 5
DISSOLUTION RATE CONSTANTS FOR WATER/IPA MIXTURES

Solvent Composition	k (s^{-1})
100% Water	0.01
Water/IPA (80:20)	0.06
Water/IPA (20:80)	0.79

Solvent composition comprises of varying the solubility of the system by altering the amount of IPA used in water. The magnitude of the solubility gives some clues about the mode (transport or surface reaction) that controls the dissolution rate of the solid. Lasaga (26) stated that for aqueous solutions, solids with low solubility dissolve by surface control, whereas highly soluble solutes dissolve by transport control. These mechanisms are applicable to our case. In short, solvent composition is a major factor affecting dissolution rate of solute molecules for a given particle type.

3.4 Effect of Temperature

The temperature effects were studied at three different temperatures (20°C, 30°C, and 40°C) for granular paracetamol particles in water. Increasing the temperature of the solvent increases the solubility of the drug and hence increases the dissolution rate as shown in Figure 9.

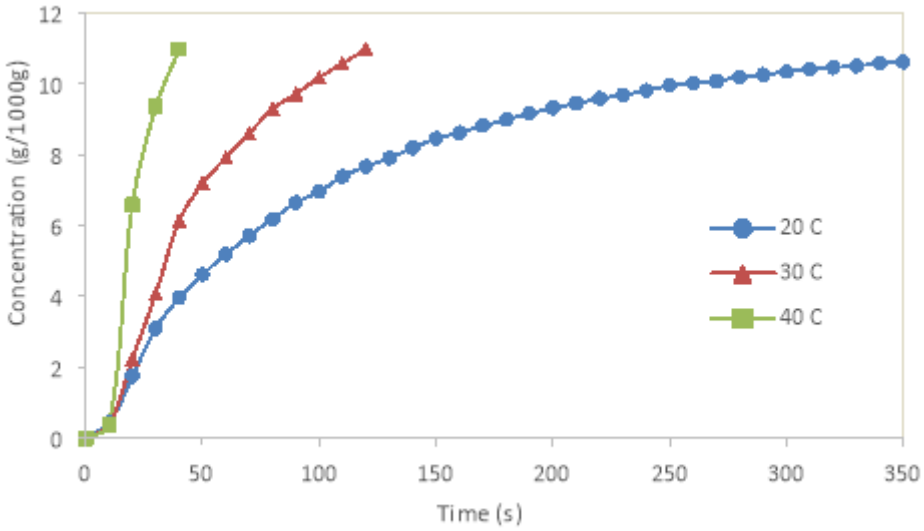

FIGURE 9 DISSOLUTION PROFILE OF GRANULAR PARACETAMOL IN WATER (MIXING SPEED = 500 RPM)

The dissolution rate constant obeys the Arrhenius equation, higher temperatures results in an increase in the rate constant (see Table 6).

TABLE 6
DISSOLUTION RATE CONSTANTS AT VARYING TEMPERATURES

Temperature	k (s^{-1})
20°C	0.01
30°C	0.03
40°C	0.09

The dissolution rate is approximately 3 times faster for every 10 degree rise in temperature which is consistent with the reduction in dissolution time by approximately 1/3 for each 10 degree increase as shown in Table 7.

TABLE 7
TIME TO DISSOLUTION OF GRANULAR PARACETAMOL IN VARYING SOLVENT COMPOSITIONS

	Dissolution Time (s)
20°C	350
30°C	100
40°C	30

Using a pair of temperatures and rate constants in Table 6, the activation energy (and the frequency factor) can be calculated for this dissolution as 19.45 kJ mol^{-1}. Sparks (28) indicated that typical values of activation energies <21 kJ mol^{-1} were for transport-controlled processes in water and 42–84 kJ mol^{-1} for surface reaction controlled at solid surfaces. It must be noted that these values were established for dissolution of minerals, and may not apply strictly to the dissolution of paracetamol particles. Nevertheless, the low value of activation energy (19.45 kJ mol^{-1}) deduced from Figure 9 indicates that paracetamol dissolution is controlled by transport processes in water.

3.5 Effect of Mixing Intensity

The intensity of the mixing was varied by increasing the agitator speed (250 rpm, 500 rpm, and 750 rpm) for dissolution of powder paracetamol particles in water at 20 ^{o}C. The impact of increasing the mixing within the STV resulted in increased dissolution rate as shown in Figure 10.

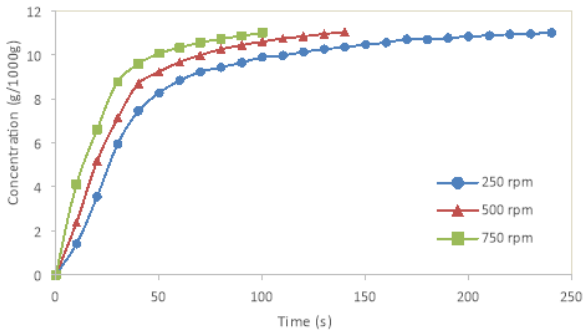

FIGURE 10 DISSOLUTION PROFILE OF PARACETAMOL POWDER IN WATER (Temperature = 20°C)

At increased mixing intensity the solvent/solute boundary layer is replenished faster with fresh solvent increasing diffusion of solute into the solvent and therefore increases the dissolution rate (see Table 8).

TABLE 8
DISSOLUTION RATE CONSTANTS AT VARYING MIXING INTENSITIES

Agitator Speed	$^{k}(s^{-1})$
250 rpm	0.022
500 rpm	0.034
750 rpm	0.059

While the dissolution rate constant increases linearly with the stirring rate (r^2 = 0.995), the overall effect of mixing intensity on dissolution is much less than either that of temperature or solvent composition.

IV. CONCLUSION

Some critical factors impacting the dissolution rate in a batch system are realised through this initial study. For the same type of particles, solvent composition (solubility) is the major parameter when dissolving bulk solids in a batch system, temperature is the 2nd contributing factor, while mixing has less effect on dissolution rates. For the same solvent and temperature, the smallest particle size has the fastest dissolution rate. The mechanism for dissolution of paracetamol in the stirred tank vessel could be the combination of both surface and transport processes. Although micronised solids increased the dissolution rate, the flowability of such material would have a negative impact in a continuous flow system, potentially leading to bridging, blockages for instance. The learning from this work is being applied to the investigation of solid dissolution in a continuous flow system using a twin screw mixer. We shall report these in a separate communication.

ACKNOWLEDGEMENTS

Authors would like to thank EPSRC, the Centre for Innovative Manufacturing in Continuous Manufacturing and Crystallisation, and GSK for their support and funding. Particular thanks and acknowledgement goes to the mentoring support provided by Gareth Alford, GSK. The helpful discussions with Deborah Bowering, University of Strathclyde is also acknowledged. The authors would like to acknowledge that this work was carried out in the CMAC National Facility, housed within the University of Strathclyde's Technology and Innovation Centre, and funded with a UKRPIF (UK Research Partnership Institute Fund) capital award, SFC ref. H13054, from the Higher Education Funding Council for England (HEFCE).

REFERENCES

[1] Lee SL, O'Connor TF, Yang X, Cruz CN, Chatterjee S, Madurawe RD, et al. Modernizing Pharmaceutical Manufacturing: from Batch to Continuous Production. Journal of Pharmaceutical Innovation. 2015;10(3):191-9.

[2] PLUMB K. Continuous Processing in the Pharmaceutical Industry Changing the Mind Set. Chemical Engineering Research and Design. 2005;83:730-8.

[3] Dimian AC, Bildea CS, Kiss AA. Chapter 11 - Batch Processes. In: Alexandre C. Dimian CSB, Anton AK, editors. Computer Aided Chemical Engineering. Volume 35: Elsevier; 2014. p. 449-88.

[4] Towler G. Preface to the Second Edition. Chemical Engineering Design (Second Edition). Boston: Butterworth-Heinemann; 2013. p. xi-xii.

[5] Koganti V, Carroll F, Ferraina R, Falk R, Waghmare Y, Berry M, et al. Application of Modeling to Scale-up Dissolution in Pharmaceutical Manufacturing. AAPS PharmSciTech. 2010;11(4):1541-8.

[6] Pangarkar VG, Yawalkar AA, Sharma MM, Beenackers AACM. Particle−Liquid Mass Transfer Coefficient in Two-/Three-Phase Stirred Tank Reactors. Industrial & Engineering Chemistry Research. 2002;41(17):4141-67.

[7] Baxendale IR, Braatz RD, Hodnett BK, Jensen KF, Johnson MD, Sharratt P, et al. Achieving Continuous Manufacturing: Technologies and Approaches for Synthesis, Workup, and Isolation of Drug Substance. May 20–21, 2014 Continuous Manufacturing Symposium. Journal of Pharmaceutical Sciences. 2015;104(3):781-91.

[8] Page T, Dubina H, Fillipi G, Guidat R, Patnaik S, Poechlauer P, et al. Equipment and Analytical Companies Meeting Continuous Challenges. May 20–21, 2014 Continuous Manufacturing Symposium. Journal of Pharmaceutical Sciences. 2015;104(3):821-31.

[9] Wood A. Generic Batch Procedures for Flexible Manufacturing. Control Engineering. 2009;56(3):P1-P5.

[10] Hörmann T, Suzzi D, Khinast JG. Mixing and Dissolution Processes of Pharmaceutical Bulk Materials in Stirred Tanks: Experimental and Numerical Investigations. Industrial & Engineering Chemistry Research. 2011;50(21):12011-25.

[11] Kaialy W, Larhrib H, Chikwanha B, Shojaee S, Nokhodchi A. An approach to engineer paracetamol crystals by antisolvent crystallization technique in presence of various additives for direct compression. International journal of pharmaceutics. 2014;464(1-2):53-64.

[12] Kwon JS-I, Nayhouse M, Christofides PD, Orkoulas G. Modeling and control of crystal shape in continuous protein crystallization. Chemical Engineering Science. 2014;107(0):47-57.

[13] Ferguson S, Morris G, Hao H, Barrett M, Glennon B. In-situ monitoring and characterization of plug flow crystallizers. Chemical Engineering Science. 2012;77:105-11.

[14] Whitney AANaWR. The Rate of Solution of Solid Substances in their own Solutions. Journal of the American Chemical Society. 1897;19(12):930-4.

[15] Higuchi T. Rate of release of medicaments from ointment bases containing drugs in suspension. Journal of Pharmaceutical Sciences. 1961;50(10):874-5.

[16] Danckwerts PVPV. I EC.43.

[17] Bruner LL. Uber die auflÃsungsgeschwindigkeit fester kÃrper. Zeitschrift fÃ¼r Physikalische Chemie.35:283-90.

[18] Rohani HHaS. Measurement and Prediction of Solubility of Paracetamol in Water-Isopropanol Solution. Part 1. Measurement and Data Analysis. Organic Process Research & Development. 2006;10:1101-9.

[19] Granberg RA, Rasmuson ÅC. Solubility of Paracetamol in Pure Solvents. Journal of Chemical & Engineering Data. 1999;44(6):1391-5.

[20] Fujiwara M, Chow PS, Ma DL, Braatz RD. Paracetamol Crystallization Using Laser Backscattering and ATR-FTIR Spectroscopy: Metastability, Agglomeration, and Control. Crystal Growth & Design. 2002;2(5):363-70.

[21] Dorris GM, Gray DG. Adsorption of n-alkanes at zero surface coverage on cellulose paper and wood fibers. Journal of colloid and interface science. 1980;77(2):353-62.

[22] Zhang Y, Jiang Y, Zhang D, Li K, Qian Y. On-line concentration measurement for anti-solvent crystallization of β-artemether using UV–vis fiber spectroscopy. Journal of Crystal Growth. 2011;314(1):185-9.

[23] Hocsman A, Di Nezio S, Charlet L, Avena M. On the mechanisms of dissolution of montroydite [HgO(s)]: Dependence of the dissolution rate on pH, temperature, and stirring rate. Journal of colloid and interface science. 2006;297(2):696-704.

[24] Guidry MW, Mackenzie FT. Experimental study of igneous and sedimentary apatite dissolution: Control of pH, distance from equilibrium, and temperature on dissolution rates. Geochimica et Cosmochimica Acta. 2003;67(16):2949-63.

[25] Lee T, Lin HY, Lee HL. Engineering reaction and crystallization and the impact on filtration, drying, and dissolution behaviors: The study of acetaminophen (paracetamol) by in-process controls. Org Process Res Dev. 2013;17(9):1168-78.

[26] Lasaga AC. Kinetic Theory in the Earth Sciences. New Jersey: Princeton University Press; 1997.

[27] Barra J, Lescure F, Doelker E, Bustamante P. The Expanded Hansen Approach to Solubility Parameters. Paracetamol and Citric Acid in Individual Solvents. Journal of Pharmacy and Pharmacology. 1997;49(7):644-51.

[28] Sparks DL, Fendorf SE, Toner CV, Carski TH. Kinetic Methods and Measurements. In: Sparks DL, Page AL, Helmke PA, Loeppert RH, editors. Methods of Soil Analysis Part 3—Chemical Methods. SSSA Book Series. Madison, WI: Soil Science Society of America, American Society of Agronomy; 1996. p. 1275-307.

SUPPLEMENTARY MATERIAL

TABLE 1
COMPARISON OF MEASURED SOLUBILITY USING GRAVIMETRIC TECHNIQUE AND REPORTED SOLUBILITY USING ATR-FTIR TECHNIQUE FOR PARACETAMOL IN WATER – IPA MIXTURES

Water Mass (%)	T (°C)	Measured Solubility (g/1000g solvent)	Reported Solubility (g/1000g solvent)	% Error
20	20	218.60	224.95	2.8
20	30	264.34	274.01	3.5
20	40	321.83	331.72	3.0
80	20	43.96	45.69	3.8
80	30	68.64	70.45	2.6
80	40	103.90	107.67	3.5
100	20	11.91	12.22	2.5
100	30	17.21	17.36	0.9
100	40	24.21	24.75	2.2

TABLE 2
SOLID LOADING OF PARACETAMOL

Solid Loading (g/l)			
Solvent System	**20˚C**	**30˚C**	**40˚C**
Water	11.61	16.49	23.51
Water/IPA (80:20)	43.41	66.93	102.29
Water/IPA (20:80)	213.70	260.31	315.13

Investigation of thermodynamic Properties Composition of Al-Fe-Ni system

Ana Kostov

Mining and Metallurgy Institute Bor, Zeleni bulevar 35, 19210 Bor, Serbia

***Abstract*—** *Thermodynamic properties of the Al-Fe–Ni system and its constituent's binary systems in a wide temperature range of 1873-1973 K and the whole range of concentrations have been studied using the FactSage.*

Keywords*— *Al-Fe-Ni, FactSage, thermodynamic properties.

I. INTRODUCTION

The ternary system Al-Fe-Ni as well as the other aluminides are of interest as high temperature structural materials due to their very high melting temperatures, good oxidation resistance and low mass density. Knowledge of Al-Fe-Ni and its constituent's binary systems, their fundamental physical and chemical properties is the necessary prerequisite for the development of technical alloys [1].

A thorough knowledge of the phase equilibria and thermodynamic properties of the Al–Fe–Ni system is of fundamental importance in many applications, such as Ni-base superalloys and Ni-base shape-memory alloys because of their good magnetic properties and high thermal stability [2]. In addition to the technological importance, the Al–Fe–Ni system attracts basic scientific interest due to the existence of the decagonal quasi-crystalline phase τ3 and the order/disorder transitions between BCC A2 and BCC B2 phases, as well as between FCC A1 and L12 phases [2].

The Al–Fe–Ni system has been critically assessed by Rivlin and Raynor [3]. According to the recent work by Eleno et al. [4] and Zhang et al. [5,6], the Al–Fe–Ni system is extremely complex due to the existence of plentiful experimental data and 16 stable phases.

Using limited experimental data, Kaufman and Nesor [7] first computed several isothermal sections from 427 to 1607 ^{0}C. Mainly based on their own experimental data and supplemented with the data reported by Bradley and Taylor [8], Jia et al. [9] carried out a thermodynamic calculation for the Al–Fe–Ni system in the Ni-rich region. The phase equilibria computed by Jia et al. [9] agree well with the experimental ones. The work by Dupin et al. [10] and Du et al. [11] indicate that it is possible to describe the thermodynamic properties of disordered and ordered phases using a single equation.

So far no thermodynamic modeling has been performed over the entire temperature and composition ranges for the Al–Fe–Ni system. Because of that, the purposes of the present work are to briefly evaluate the measured thermodynamic data available for the Al–Fe–Ni system and its constituent's binary systems and to obtain an optimal set of thermodynamic parameters for the ternary system over the whole composition and temperature ranges.

II. RESULTS

Thermodynamic properties of the Al-Fe–Ni system and its constituent's binary systems in a wide temperature range of 1873-1973 K and the whole range of concentrations have been studied using the FactSage [12].

The thermodynamic calculations in Al-Fe-Ti ternary system were carried out from each corner using 15 cross sections in total. The compositions of all investigated cross sections are given in Table 1.

The results of activities for the investigated binary systems are shown in Figs. 1-3, respectively.

TABLE 1
COMPOSITION OF Al-Fe-Ni TERNARY SYSTEMS IN THE INVESTIGATED SECTIONS

Cross section	A	B	C	D	E
$x_{Al} : x_{Fe}$	9:1	7:3	5:5	3:7	1:9
$x_{Fe} : x_{Ni}$	9:1	7:3	5:5	3:7	1:9
$x_{Ni} : x_{Al}$	9:1	7:3	5:5	3:7	1:9

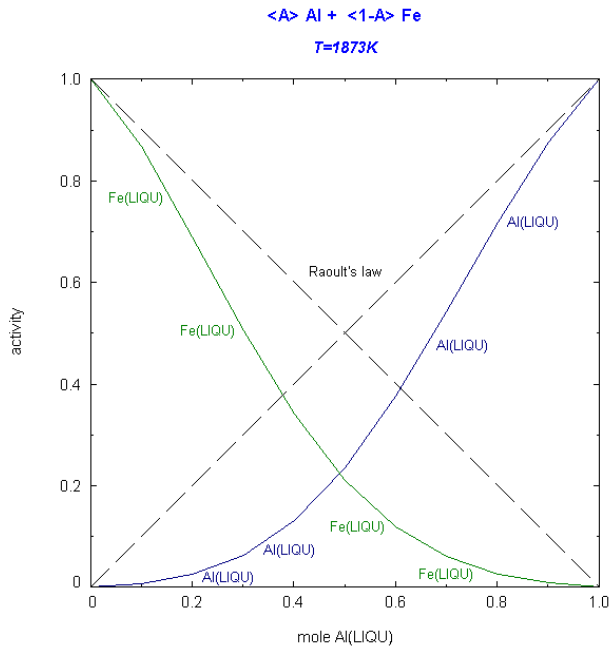

(a)

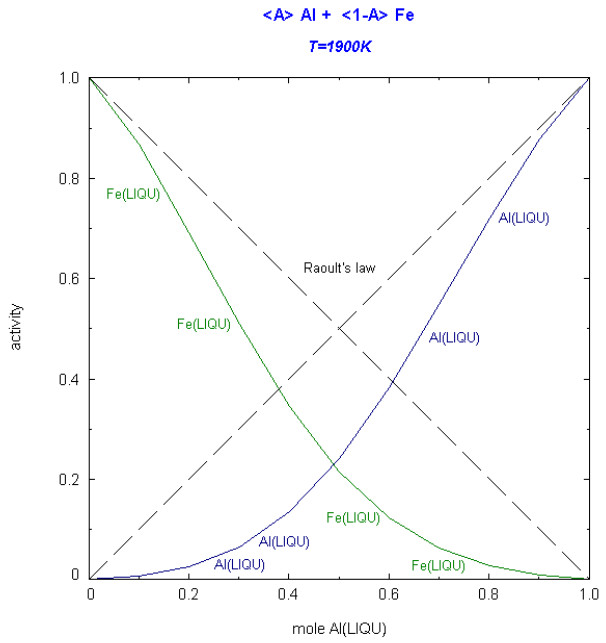

(b)

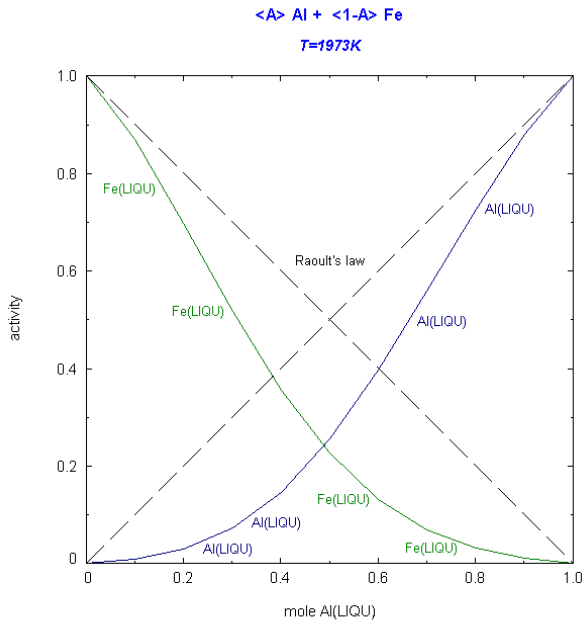

(c)

FIGURE 1. ACTIVITY OF Al AND Fe AT a) 1873K, b) 1900K, c) 1973K

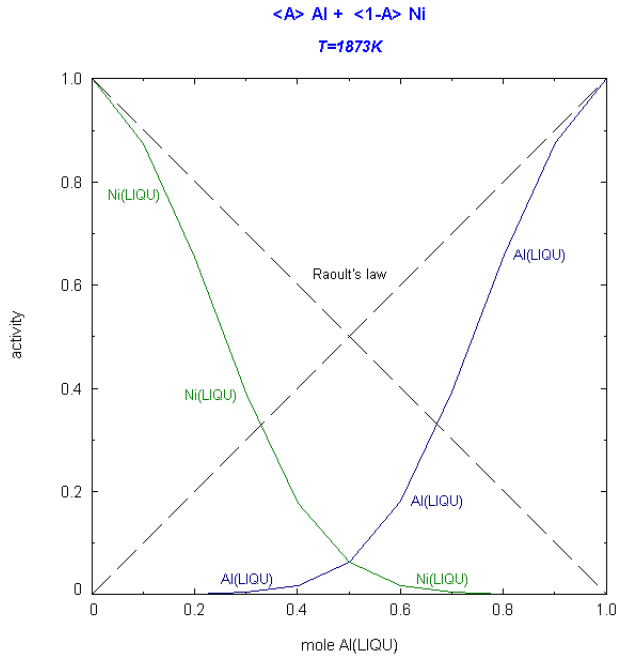

(a)

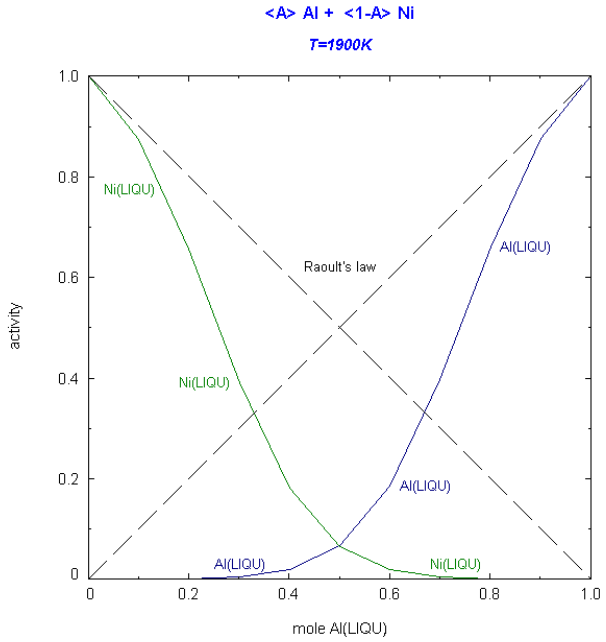

(b)

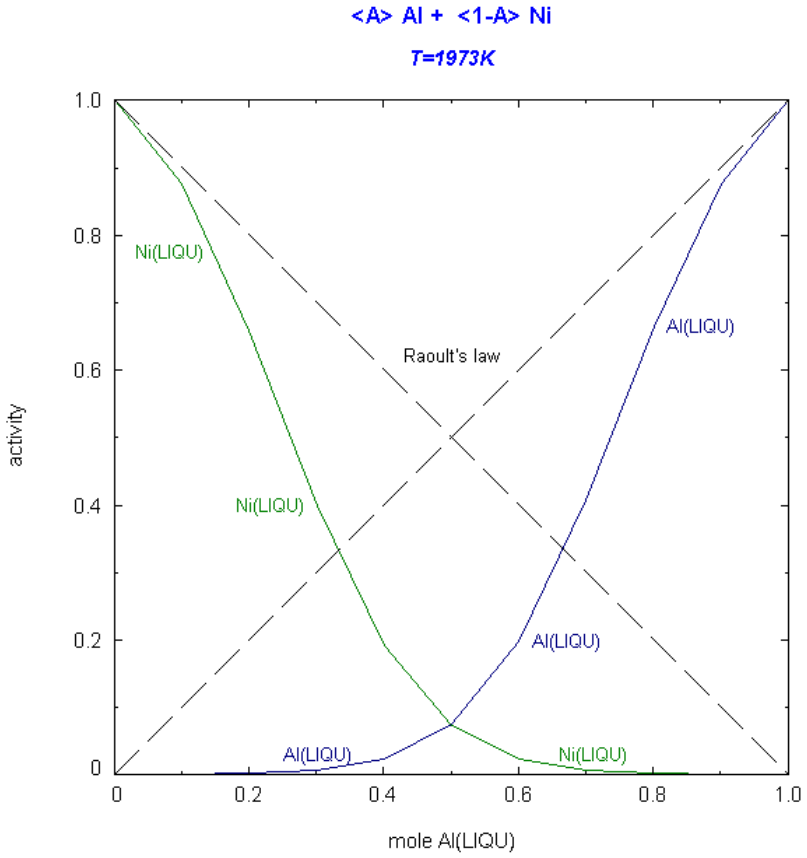

(c)

FIGURE 2. ACTIVITY OF Al AND Ni AT a) 1873K, b) 1900K, c) 1973K

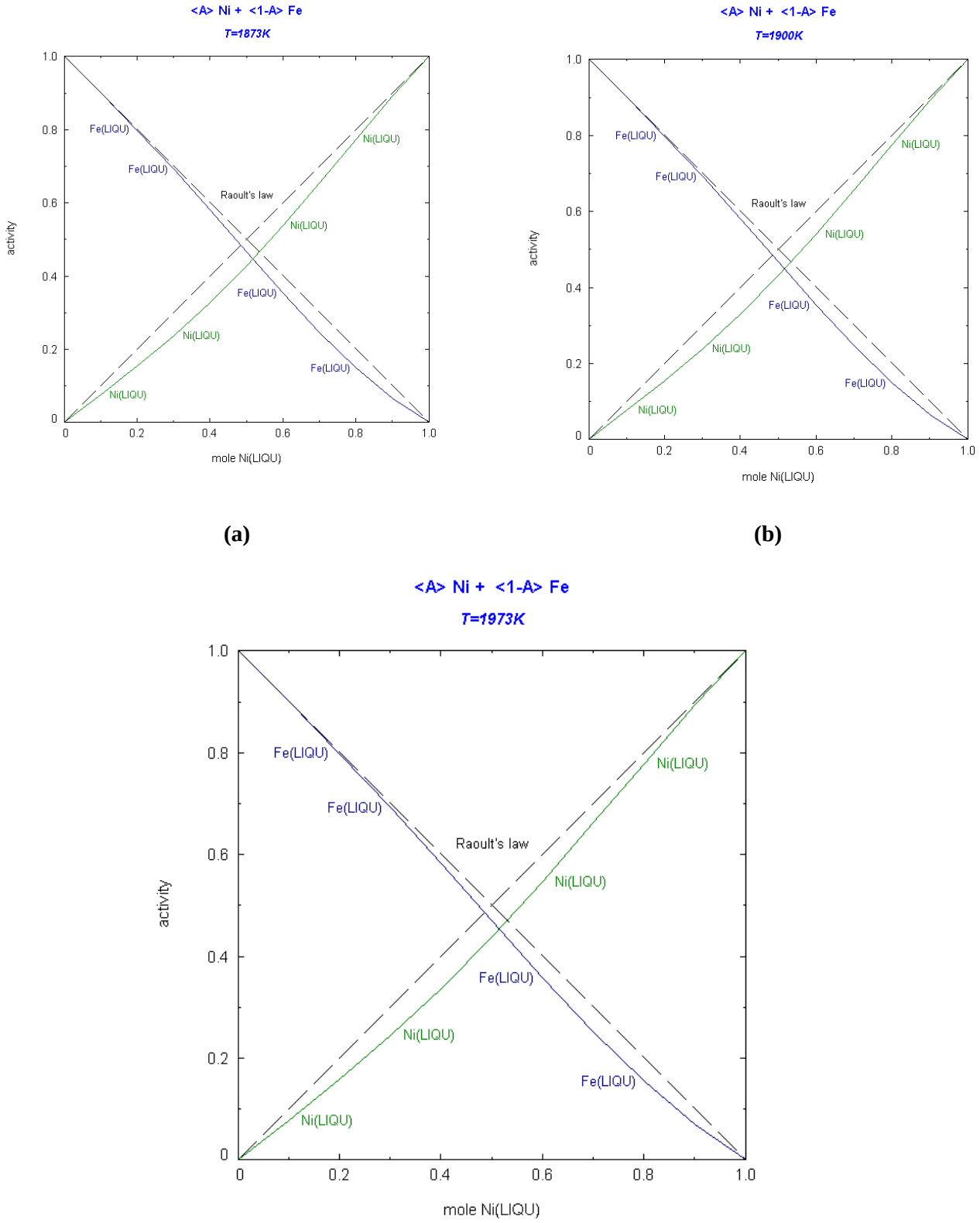

(a) **(b)**

(c)

FIGURE 1. ACTIVITY OF Ni AND Fe AT a) 1873K, b) 1900K, c) 1973K

Values for the integral Gibbs energy of mixing and integral excess Gibbs energy of Al-Fe-Ni ternary system at 1873K, 2000K and 2073K are presented in Tables 2, 3 and 4.

TABLE 2
INTEGRAL GIBBS ENERGY OF MIXING AND EXCESS GIBBS ENERGY FOR Al-Fe-Ni TERNARY SYSTEM AT 1873K

x_{Al}	x_{Fe}	x_{Ni}	ΔG^M	ΔG^E	x_{Fe}	x_{Ni}	ΔG^M	ΔG^E
Cross section A					**Cross section B**			
0	0,9	0,1	-5885	-823	0,7	0,3	-11214	-1702
0,1	0,81	0,09	-20343	-10725	0,63	0,27	-24170	-10547
0,2	0,72	0,08	-31022	-19180	0,56	0,24	-33140	-17738
0,3	0,63	0,07	-38596	-25540	0,49	0,21	-39113	-22942
0,4	0,54	0,06	-42924	-29407	0,42	0,18	-42146	-25958
0,5	0,45	0,05	-43897	-30572	0,35	0,15	-42242	-26692
0,6	0,36	0,04	-41495	-28990	0,28	0,12	-39432	-25147
0,7	0,27	0,03	-35799	-24767	0,21	0,09	-33794	-21428
0,8	0,18	0,02	-26979	-18174	0,14	0,06	-25439	-15745
0,9	0,09	0,01	-15247	-9679	0,07	0,03	-14449	-8436
1	0	0	0	0	0	0	0	0
Cross section C					**Cross section D**			
0	0,5	0,5	-12561	-1767	0,3	0,7	-10780	-1267
0,1	0,45	0,45	-24265	-9489	0,27	0,63	-21453	-7830
0,2	0,4	0,4	-31977	-15549	0,24	0,56	-28264	-12861
0,3	0,35	0,35	-36876	-19808	0,21	0,49	-32504	-16333
0,4	0,3	0,3	-39145	-22188	0,18	0,42	-34427	-18239
0,5	0,25	0,25	-38861	-22671	0,15	0,35	-34154	-18604
0,6	0,2	0,2	-36088	-21290	0,12	0,28	-31760	-17474
0,7	0,15	0,15	-30888	-18138	0,09	0,21	-27291	-14925
0,8	0,1	0,1	-23321	-13370	0,06	0,14	-20757	-11062
0,9	0,05	0,05	-13359	-7217	0,03	0,07	-12039	-6026
1	0	0	0	0	0	0	0	0
Cross section E								
0	0,1	0,9	-5513	-450				
0,1	0,09	0,81	-15452	-5833				
0,2	0,08	0,72	-21752	-9910				
0,3	0,07	0,63	-25762	-12706				
0,4	0,06	0,54	-27770	-14253				
0,5	0,05	0,45	-27913	-14589				
0,6	0,04	0,36	-26264	-13759				
0,7	0,03	0,27	-22850	-11819				
0,8	0,02	0,18	-17634	-8829				
0,9	0,01	0,09	-10431	-4862				
1	0	0	0	0				

TABLE 3
INTEGRAL GIBBS ENERGY OF MIXING AND EXCESS GIBBS ENERGY FOR Al-Fe-Ni TERNARY SYSTEM AT 1900K

x_{Al}	x_{Fe}	x_{Ni}	ΔG^M	ΔG^E	x_{Fe}	x_{Ni}	ΔG^M	ΔG^E
Cross section A					**Cross section B**			
0	0,9	0,1	-5936	-801	0,7	0,3	-11309	-1659
0,1	0,81	0,09	-20405	-10648	0,63	0,27	-24265	-10445
0,2	0,72	0,08	-31049	-19036	0,56	0,24	-33201	-17576
0,3	0,63	0,07	-38577	-25333	0,49	0,21	-39134	-22730
0,4	0,54	0,06	-42865	-29152	0,42	0,18	-42133	-25712
0,5	0,45	0,05	-43816	-30299	0,35	0,15	-42212	-26438
0,6	0,36	0,04	-41418	-28733	0,28	0,12	-39403	-24912
0,7	0,27	0,03	-35747	-24557	0,21	0,09	-33780	-21236
0,8	0,18	0,02	-26962	-18030	0,14	0,06	-25445	-15610
0,9	0,09	0,01	-15256	-9608	0,07	0,03	-14467	-8367
1	0	0	0	0	0	0	0	0
Cross section C					**Cross section D**			
0	0,5	0,5	-12676	-1726	0,3	0,7	-10891	-1241
0,1	0,45	0,45	-24377	-9388	0,27	0,63	-21566	-7746
0,2	0,4	0,4	-32058	-15394	0,24	0,56	-28353	-12729
0,3	0,35	0,35	-36924	-19610	0,21	0,49	-32568	-16163
0,4	0,3	0,3	-39167	-21966	0,18	0,42	-34470	-18049
0,5	0,25	0,25	-38868	-22444	0,15	0,35	-34183	-18408
0,6	0,2	0,2	-36091	-21080	0,12	0,28	-31781	-17290
0,7	0,15	0,15	-30897	-17963	0,09	0,21	-27311	-14767
0,8	0,1	0,1	-23339	-13244	0,06	0,14	-20778	-10944
0,9	0,05	0,05	-13381	-7150	0,03	0,07	-12061	-5960
1	0	0	0	0	0	0	0	0
Cross section E								
0	0,1	0,9	-5578	-443				
0,1	0,09	0,81	-15532	-5775				
0,2	0,08	0,72	-21823	-9810				
0,3	0,07	0,63	-25818	-12573				
0,4	0,06	0,54	-27811	-14098				
0,5	0,05	0,45	-27941	-14424				
0,6	0,04	0,36	-26284	-13599				
0,7	0,03	0,27	-22866	-11676				
0,8	0,02	0,18	-17650	-8718				
0,9	0,01	0,09	-10447	-4798				
1	0	0	0	0				

TABLE 4
INTEGRAL GIBBS ENERGY OF MIXING AND EXCESS GIBBS ENERGY FOR Al-Fe-Ni TERNARY SYSTEM AT 1973K

x_{Al}	x_{Fe}	x_{Ni}	ΔG^M	ΔG^E	x_{Fe}	x_{Ni}	ΔG^M	ΔG^E
Cross section A					**Cross section B**			
0	0,9	0,1	-6075	-743	0,7	0,3	-11565	-1545
0,1	0,81	0,09	-20570	-10438	0,63	0,27	-24522	-10171
0,2	0,72	0,08	-31124	-18650	0,56	0,24	-33364	-17140
0,3	0,63	0,07	-38526	-24773	0,49	0,21	-39188	-22154
0,4	0,54	0,06	-42702	-28463	0,42	0,18	-42099	-25047
0,5	0,45	0,05	-43596	-29560	0,35	0,15	-42132	-25751
0,6	0,36	0,04	-41210	-28037	0,28	0,12	-39325	-24277
0,7	0,27	0,03	-35607	-23987	0,21	0,09	-33741	-20714
0,8	0,18	0,02	-26916	-17641	0,14	0,06	-25458	-15246
0,9	0,09	0,01	-15282	-9416	0,07	0,03	-14515	-8180
1	0	0	0	0	0	0	0	0
Cross section C					**Cross section D**			
0	0,5	0,5	-12986	-1616	0,3	0,7	-11191	-1170
0,1	0,45	0,45	-24680	-9114	0,27	0,63	-21870	-7519
0,2	0,4	0,4	-32277	-14972	0,24	0,56	-28595	-12370
0,3	0,35	0,35	-37054	-19074	0,21	0,49	-32741	-15707
0,4	0,3	0,3	-39225	-21364	0,18	0,42	-34586	-17534
0,5	0,25	0,25	-38886	-21831	0,15	0,35	-34260	-17880
0,6	0,2	0,2	-36100	-20512	0,12	0,28	-31838	-16791
0,7	0,15	0,15	-30921	-17490	0,09	0,21	-27365	-14338
0,8	0,1	0,1	-23386	-12903	0,06	0,14	-20836	-10624
0,9	0,05	0,05	-13439	-6969	0,03	0,07	-12118	-5784
1	0	0	0	0	0	0	0	0
Cross section E								
0	0,1	0,9	-5754	-422				
0,1	0,09	0,81	-15751	-5619				
0,2	0,08	0,72	-22014	-9540				
0,3	0,07	0,63	-25967	-12214				
0,4	0,06	0,54	-27919	-13680				
0,5	0,05	0,45	-28017	-13980				
0,6	0,04	0,36	-26337	-13164				
0,7	0,03	0,27	-22908	-11288				
0,8	0,02	0,18	-17692	-8417				
0,9	0,01	0,09	-10491	-4626				
1	0	0	0	0				

III. CONCLUSION

The thermodynamic properties of the investigated Al-Fe-Ni ternary system and its constituent's binary systems at 1873K, 1900K and 1973K were determined. Investigated systems have negative values for integral excess Gibbs energy. Activity values of the components are less than unity and show negative deviation from the Raoult's law.

The liquidus projection and the reaction scheme for the whole concentration range in the investigated systems have been constructed, which are of interest for engineering applications, as well as for further basic materials researches.

ACKNOWLEDGEMENTS

The author would like to thank the Alexander von Humboldt Foundation, Bonn, Germany, for supporting and sponsoring this research work at the IME Institute for Process Metallurgy and Metal Recycling, RWTH Aachen, Germany.

REFERENCES

[1] D. Raj, L. Bencze, D. Kath, W.A. Oates, J. Herrmann, L. Singheiser, K. Hilpert, Intermetallics 11 (2003) 1119–1124.
[2] L. Zhang, Y. Du, Computer Coupling of Phase Diagrams and Thermochemistry, 31 (2007) 529–540.
[3] V.G. Rivlin, G.V. Raynor, Int. Met. Rev. 25 (1980) 79–93.
[4] L. Eleno, K. Frisk, A. Schneider, Intermetallics 14 (2006) 1276–1290.
[5] L.J. Zhang, Y. Du, H.H. Xu, C.Y. Tang, H.L. Chen, W.Q. Zhang, J. Alloys Compd. 454 (2008) 129-135.
[6] L.J. Zhang, J. Wang, Y. Du, R. Hu, P. Nash, X.-G. Lu, C. Jiang, Acta Materialia, Vol. 57, 18 (2009) 5324-5341.
[7] L. Kaufman, H. Nesor, Metall. Trans. 5A (1974) 1623–1629.
[8] A.J. Bradley, A. Taylor, Proc. Roy. Soc. 166A (1938) 353–375.
[9] C.C. Jia, K. Ishida, T. Nishizawa, J. Univ. Sci. Technol. Beijing 7 (2000)277–281.
[10] N. Dupin, I. Ansara, B. Sundman, CALPHAD 25 (2001) 279–298.
[11] Y. Du, Y.A. Chang, W.P. Gong, B.Y. Huang, H.H. Xu, Z.P. Jin, F. Zhang, S.L. Chen, Intermetallics 11 (2003) 995–1013.
[12] C.W. Bale, P. Chartrand, S.A. Degterov, G. Eriksson, K. Hack, R.B. Mahfoud, J. Melancon, A.D. Pelton, S. Petersen, CALPHAD 26 (2002) 189-228.

Degradation on 2,4,6-Trinitrophenol by cold plasma technology

Nguyen Van Hoang[1], Nguyen Cao Tuan[2]

Institute of New Technology, 17 Hoang Sam Street, Cau giay, Hanoi, Vietnam

Abstract**—** *Cold plasma exhibits many advantages in environmental treatment without additive reagent required. The 2,4,6-Trinitrophenol (TNP) might be degraded with high efficiency using cold plasma. The main factors influencing the TNP degradation have been studied. The kinetics of the TNP process proposed fits to the pseudo- first order reaction. The overall reaction rate expression was established to be - r= 0.024C_{TNP} at low TNP concentration*

Keywords**— Cold plasma, 2,4,6-Trinitrophenol, degradation by plasma.***

I. INTRODUCTION

Since the late of 20th century, plasma field as a new study filed has been interested in the great attention of many scientists in over the word [1]. The plasma chemistry is focused on studying about the energetic particles (electrons and ions) in plasma participated in chemical reactions. The plasma can be divided into two kinds such as thermal plasma and cold plasma depending on the electron temperature and ion temperature [1,2]. According this principle, thermal plasma has electron temperature equal to ion temperature, while for cold plasma, the electron temperature is higher than the ion temperature. The cold plasma produced in water solutions forms the basis of an innovative advanced oxidation technology of water treatment. So that recently cold plasma has been considered to be a useful method in environmental pollution treatment technology concluding solid, liquid and gas wastes [3,4]. Because, the degradation of these substances has been based on the strongly active species (free radicals) generated from cold plasma process. Cold plasma is produced by gas discharge or combined with air in atmosphere that results in highly oxidative species such as electrons, ions, radicals, excited atoms and molecules [5]. So that use of cold plasma technique is an environmentally friendly and cost – effective alternative due to without any additional chemical reagents used and therefore their disposal is not required. Cold plasma can be classified into many types in which dielectric barrier discharge (DBD) is one of these. In this paper cold plasma with DBP (shortly called cold plasma) used to degrade 2,4,6 –Trinitrophenol will be presented in detail.

2,4.6-Trinitro phenol TNP (picric acid) is an organic compound with the formula $(O_2N)_3C_6H_2OH$, mass molecule 229.10 g·mol^{-}, pka = 0.38, which used in munitions explosives or in medicine and dyes [6]. 2,4.6-Trinitrophenol is toxic that causes headache, vertigo, nausea, vomiting, diarrhea, inflammation of kidney and acute hepatitis and red colored urine may be produced [7].

In this paper the 2,4,6-trinitrophenol in waste water treated by cold plasma (DBD) will be studied in detail including degradation efficiency and the experimental conditions under that provides the highest efficiency.

II. EXPERIMENTAL PART

2.1 Chemical

The experimental method was carried out based on the previous work published in previous paper. It includes the following items:

- 2,4,6-Trinitrophenol with analytical purity grade purchased from China.

Other chemicals such as methanol (Merck, Germany), and NaOH, H_2SO_4, H_2O_2 with analytical purity grade purchased from China too.

2.2 Apparatus

- HPLC Model HP 1100, using *diode-array detector*. (DAD), Agilent (USA),
- Spectrophotometer UV- Vis Agilent 8453 (USA),
- The schematic structure of plasma reactor shown in the Fig 1.

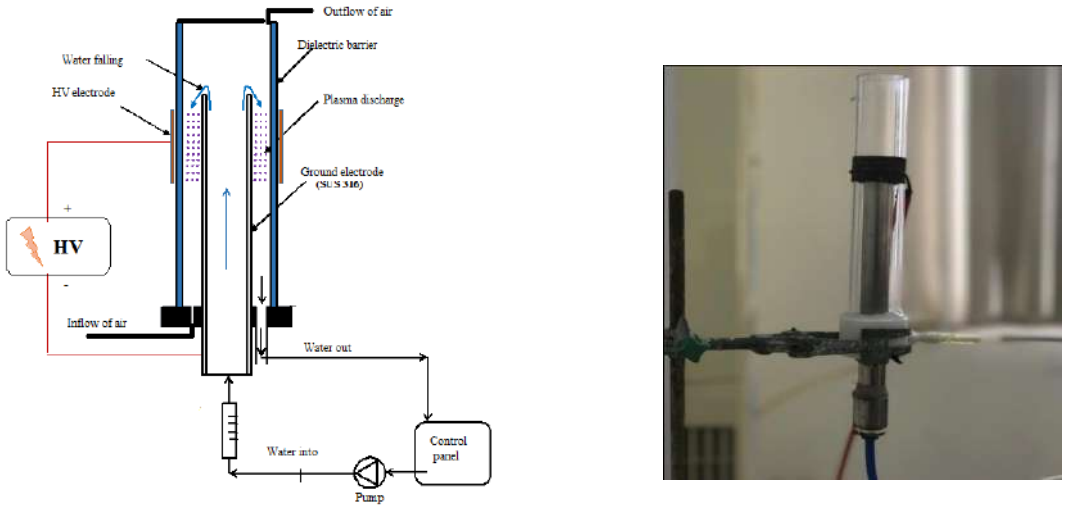

FIG.1. SCHEMATIC STRUCTURE OF PLASMA REATOR

2.3 Experimental procedure

The experimental procedure is focused on studying the following items:

2.3.1 Formation of cold plasma

The appearance of cold plasma will carried out under conditions like electric current varying from 3.5 to 22 mA and electrode potential increasing from 7 to 21 kV (HV). Plasma intensity appeared is recognized by the naked eyes and through TNP degradation efficiency.

2.3.2 Degradation of TNP from water in varying electric power

To increase the degradation of process, the plasma is in direct contact with the thin film of water falling via a grounded electrode. The TNP contaminated water sample is always circulated through reactor during the reaction proceeding, with the rate of 415 mL/minute and the air rate blowing with 3 liter/min. The degradation of TNP is carried out under the conditions such as: volume of sample is 500 mL containing a certain concentration of TNP, pH of samples from 3.2 to 11 at different electric powers. After an interval of reaction time, a certain volume of sample is taken out to measuring the TNP concentration left, by HPLC method as suggested in [9].The removal of efficiency of TNP is calculated using the expression:

$$H = \frac{(C_0 - C_t)}{C_0} \times 100, (\%)$$

Here H is removal efficiency of TNR. C_0 and C_t are concentrations of TNP at the initial and t reaction time in mg/L.

The average rate of TNP degradation (r) is also calculated by the expression:

$$- r = \frac{(C_{t2} - C_{t1})}{\Delta t}, mg/L.\min$$

Here r denoted the average reaction rate (mg/l.min), Δt is the time interval from t1 to t2, min.

2.3.3 Study on increasing degradation efficiency of TNP

The experimental method was implemented like 2.3.2 but adding H_2O_2

2.3.4 Study on other factors influencing degradation efficiency of TNP

- Influence of initial concentration of TNP, the experiments are carried out like in 2.3.2 but varying initial concentration of TNP.
- Influence of pH, the experiments was implemented like in 2.3.2, but the pH varying from 3.2 to 11.

III. RESULTS AND DISCUSSION

3.1 Influence of electric powers on TNP degradation

The results of TNP degradation efficiency and reaction rate, under the varying electric powers such as varying U and I were presented in Table 1 and in Fig.2**.** Under the conditions such as U =21 kV, I = 22 mA, the plasma discharge can reach the highest power. The results of influence of electric power are presented in Table 1 and Fig.2.

TABLE 1
INFLUENCE OF ELECTRIC POWERS ON TNP DEGRADATION

Reaction times, min	TNP/plasma								
	I=10mA, U=16kV			I=16mA, U=19kV			I=22mA, U=21kV		
	C_t, mg/L	H, %	r, mg/L.min	C_t, mg/L	H, %	r, mg/L.mim	C_t, mg/L	H, %	r, mg/L.min
0	135.30			135.30			135,30		
30	109.01	19.43	0.88	84.20	37.77	1.70	41.86	69.21	3.11
60	89.20	34.07	0.66	50.19	62.90	1.13	11.65	91.54	1.01
90	68.59	49.31	0.69	25.08	81.47	0.84	2.11	98.59	0.32
120	52.82	60.96	0.53	13.05	90.36	0.40	0.70	99.63	0.05

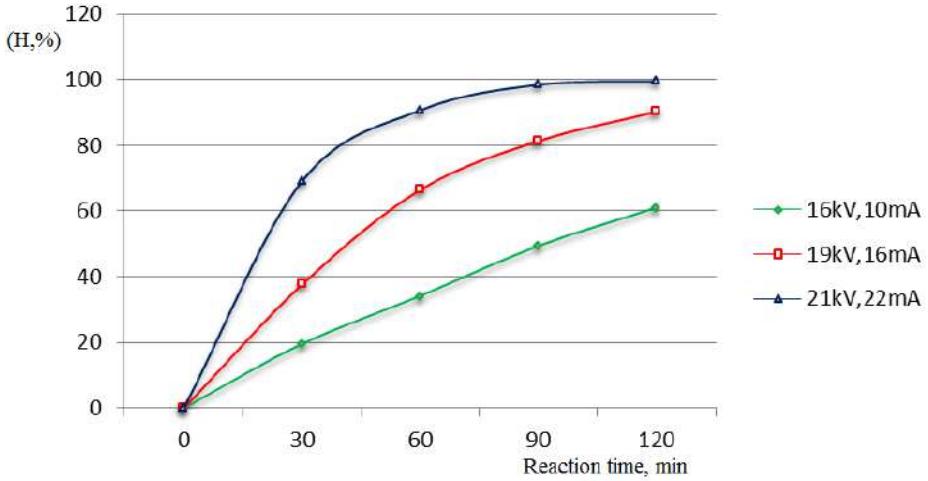

FIG.2. INFLUENCE OF ELECTRIC POWER ON TNP DEGRADATION

The obtained experimental data showed that the degradation efficiency and degradation rate for the same TNP concentration (135.30 mg/L) were enhanced with the increase of the used voltage. This is due to at higher voltage, electrons at the cathode surface are produce easily so that could increase the solution's electric field intensity and generate more oxidative, active particles such as O_3, $O^{\bullet}$,$^{\bullet}OH$, H_2O_2, so increasing degradation of TNP. This phenomena were explained in the work [8 -12].

3.2 Influence of the initial pH on the TNP degradation

As known, during discharge, plasma would be formed, producing oxidative particles including O_3, $O^{\bullet}$,$^{\bullet}OH$, H_2O_2at the gas - water interface in the reactor. These active particles must dissolve into water sample to initiate oxidation process to degrade TNP. The chemical activity of these particles in water sample depends on the pH-water. In water, the O_3- formation in plasma can react with H_2O molecules to form$^{\bullet}OH$, but O_3 would be decomposed at high pH and fairly stable at low pH [8]. The $^{\bullet}OH$-existence is higher in neutral or alkaline media than in an acidic one [13], so $^{\bullet}OH$ radical would be formed more at higher pH. Owing to these reason, the TNP degradation efficiency would higher in the weak or neutral reaction medium. The results of pH influencing the TNP degradation by cold plasma were presented in Table 2 and Fig.3.

TABLE 2
INFLUENCE OF pH ON TNP DEGRADATION

Reaction time, min	TNP/plasma								
	pH = 3.2			pH = 7.0			pH = 11.0		
	C_t, mg/L	H, %	r, mg/L.min	C_t, mg/L	H, %	r, mg/L.min	C_t, mg/l	H, %	r, mg/L.min
0	135.30			135.30			135.30		
30	84.10	37.84	1.71	86.20	38.29	1.64	90.66	32.99	1.49
60	50.19	62.90	1.13	50.00	63.05	1.21	54.74	59.54	1.20
90	25.08	81.47	0.84	26.00	82.78	0.80	30.35	77.57	0.81
120	13.05	90.36	0.40	11.30	91.65	0.49	16.10	88.10	0.48

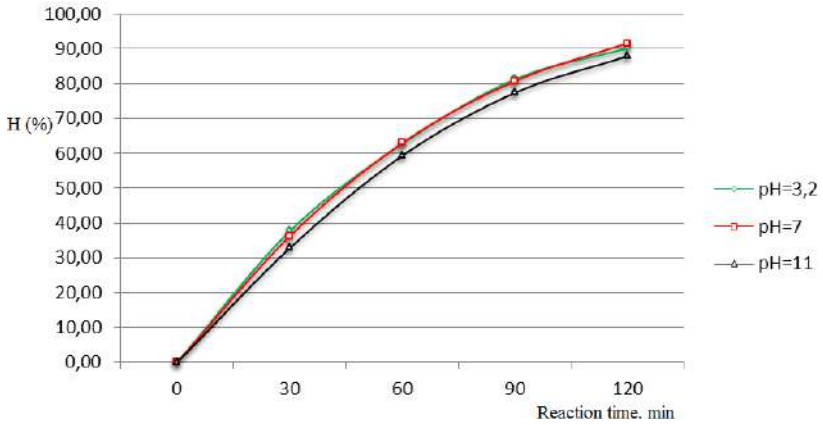

FIG. 3. INFLUENCE OF Ph ON TNP DEGRADATION

The experimental data showed that the TNP degradation efficiencies are higher in the pH range of 3.2 -7.0 than from 7 to 11. This is in accordance with the theory suggested above.

3.3 Influence of TNP initial concentration on degradation

Here there are three series of the initial TNP concentrations were selected for study their influence on the degradation reaction rate such as:

C_{TNP} = 91.02, mg/L, C_{TNP} =135.3, mg/L, C_{TNP} = 210.17, mg/L and

C_{TNP}= 50.46, mg/L C_{TNP}= 84.10, mg/L C_{TNP}= 149.67, mg/L

C_{TNP}= 25.26, mg/L C_{TNP}= 50.19, mg/L C_{TNP}= 105.00, mg/L

The TNP degradation rate was measured for 30 minute reaction listed in Table 3.

TABLE 3
INFLUENCE OF TNP-INITIAL CONCENTRATION ON DEGRADATION REACTION RATE

Series I	**TNP concentration, mg/L**	91.02	135.3	210.17
	Reaction rate, r mg/L/min	1.35	1.71	2.02
Series II	**TNP concentration, mg/L**	50.46	84.10	149.67
	Reaction rate, r mg/L/min	0.84	1.13	1.62
Series III	**TNP concentration, mg/L**	25.26	50.19	105.00
	Reaction rate, r mg/L/min	0.49	0.84	1.22

In the previous study [ ], the degradation rate expression of TNR by cold plasma fitted to the equation:

$$- r = \frac{k_1 C_{TNR}}{1 + k_2 C_{TNR}}$$

Using this expression, the rate expression corresponding the every series of the initial TNP concentration was calculated, resulted in as following:

For series I. $$-r = \frac{0.0247 C_{TNP}}{1 + 0.0073 C_{TNP}}$$

For series II $$-r = \frac{0.0231 C_{TNP}}{1 + 0.0080 C_{TNP}}$$

For series III. $$-r = \frac{0.0243 C_{TNP}}{1 + 0.0098 C_{TNP}}$$

The obtained rate expression showed that when C_{TNP} is small meaning the product of 0.0073, 0.0080 and 0.0089 with C_{TNP} very small the 1, the above rate expressions become:

For series I, $-r = 0.0247 C_{TNP}$,

For series II, $-r = 0.0231 C_{TNP}$

Fore series III,$-r = 0.0243 C_{TNP}$

The overall rate expression could be resulted in:

This rate expression is fitted to the experimental data suggested in Table 3.

3.4 Increase of TNP degradation efficiency by plasma discharge combined with H_2O_2

The addition H_2O_2 into reactor with plasma might enhance TNP degradation, presented in Fig.4

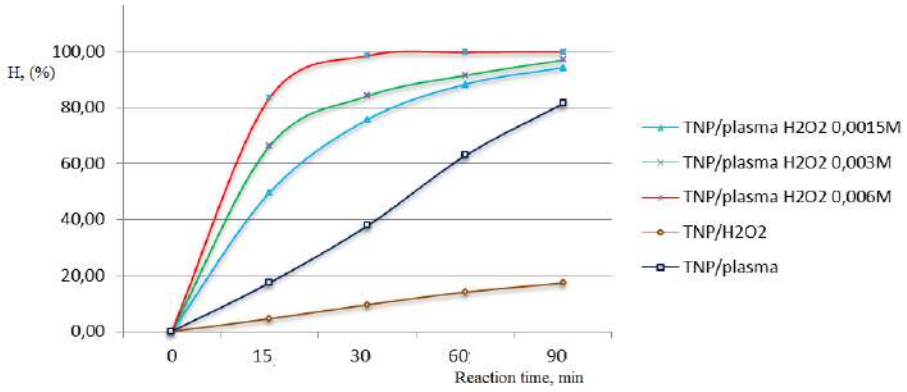

FIG. 4. INFLUENCE OF H_2O_2 ADDITION ON DEGRADATION EFFICIENCIES

The obtained experimental data have shown the presence of H_2O_2 increases the TNP degradation efficiency. The high efficiency might explain by the activation of H_2O_2 by plasma (UV) in plasma reactor to produce hydroxyl radical as following

$$H_2O_2 + h\nu \rightarrow HO^{\bullet} + {}^{\bullet}OH$$

The increase of hydroxyl radical leads to increase the TNP degradation efficiency. This was suggested in previous work.

3.5 Proposed kinetic TNP degradation by cold plasma

As suggested above the TNP degradation rate by constant plasma obeyed the equation:

$$-r = \frac{k_1 C_{TNP}}{1 + k_2 C_{TNP}}$$

At the low TNP concentration (when $1>>k_2C_{TNP}$) , the reaction rate becomes

$$- r = k_1C_{TNP} = 0.024C_{TNP}$$

It means the reaction follows a pseudo-first order kinetic. The experiment was carried out with the TNP concentration of 91.02 mg/L to degrade by constant condition of plasma for the different times listed in Table 4 as follows:

TABLE 4
THE CHANGE OF TNP CONCENTRATION FOR THE TIME

Reaction time, min	0	30	60	90
TNP conc. mg/L	91.02	50.46	25.26	10.71

Using these data, the integral expression corresponding the pseudo-first order reaction was determined:

$$\ln(C/C_0) = - 0.0244t$$

and its plot was presented in Fig.5.

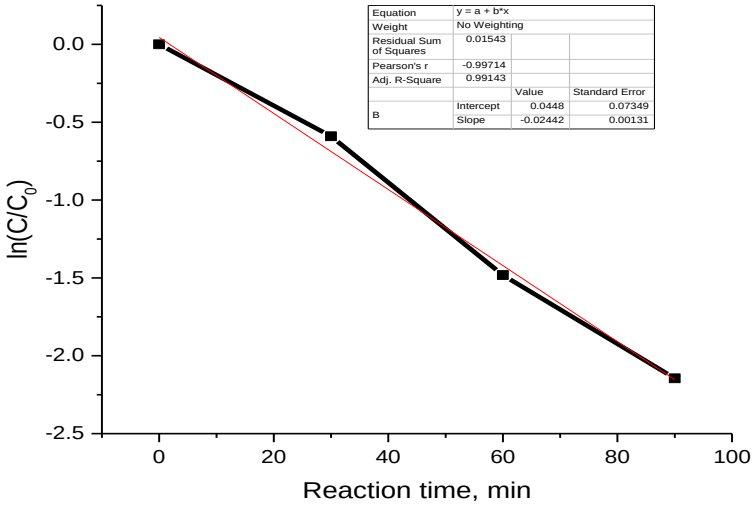

FIG.5. THE PLOT OF $\ln(C/C_0)$ VS. TIME

The obtained reaction rate constant is similar with the author [14].

IV. CONCLUSION

Cold plasma technology has been applied in environmental treatment with the many advantages. The main principle of cold plasma technology is based on the oxidative particles including free radical $^{\bullet}OH$ and active ions or molecules generating in situ under the high electric voltage to degrade pollutants from wastewater. The cold plasma has been used to degrade TNP in water samples resulting in high efficiency. The influence of main factors such as pH, reaction time, additive H_2O_2, TNP concentration was studied. The cold plasma used to degrade TNP yielded high efficiency at the range of pH 3.2-11 and its efficiency enhancing with additive H_2O_2. The kinetics of the TNP degradation under cold plasma has been suggested, following the pseudo - first order reaction at the low TNP concentration.

ACKNOWLEDGEMENTS

We thank prof. Dr. Dang Kim Chi at Hanoi University of Science and Technology for assistance with particular technique, methodology, and for comments that greatly improved the manuscript.

REFERENCES

[1] Jinzhang Gao. 2006, A novel Technique for wastewater Treatment by contact glow- discharge electrolysis, Pakistan Journal of Biological Sciences, 9(2) 323- 329.

[2] Von Engel, A. and Cozens, J.R. (1976) "Flame Plasma" in *Advances in electronics and electron physics*, L. L. Marton (ed.), Academic Press, ISBN 978-0-12-014520-1, p. 99

[3] Lukeš, P., M. Čplupek, V. Babickŷ, P. Šunka, G. Winterová and V. Janda . 2003, Non-thermal plasma induced decomposition of 2-chlorophenol in water. Acta Phy. Slovaca, 53(6) 423-428

[4] 4. Šunka, P., V. Babickŷ, M. Čplupek, P. Lukeš, M. Šimek, J. Schmidt and M. Černák, 1999 Generation of chemically active species by electrical discharges in water. Plasma Sources Sci. T., 8(2), 258-265 .

[5] Locke, B.R., M. Sato, P. Sunka, M.R. Hoffmann Cheng et al. 2006: Review for Non-thermal plasma 433 and J.S. Chang, Electrohydraulic discharge and non-thermal plasma for water treatment. Ind. Eng. Chem. Res., 45(3), 882-905.

[6] https://en.wikipedia.org/wiki/Picric_acid.

[7] Wyman JF, Serve MP, Hobson DW, Lee LH, Uddin DE, 1992. Acute toxicity, distribution, and metabolism of 2,4,6-trinitrophenol (picric acid) in Fischer 344 rats.J Toxicol Environ Health. 1992 Oct;37(2):313-27.

[8] Chen, Y.S., X.S. Zhang, Y.C. Dai and W.K. Yuan, 2004. Pulsed high-voltage discharge plasma for degradation of phenol in aqueous solution. Sep. Purif. Technol., 34(1-3), 5-12 .

[9] Sun, B., M. Sato and J.S. Clements,2000. Oxidative processes occurring when pulsed high voltage discharges degrade phenol in aqueous solution. Environ. Sci. Technol., 34(3) 509-513.

[10] Ruan, J.J., W. Li, Y. Shi,Y. Nie, X. Wang and T.E. Tan, Decomposition simulated odors in municipal wastewater treatment plants by wire-plate pulse corona reactor. Chemosphere, 59(3), 327-333 (2005).

[11] Nifuku, M., M. Horvath, J. Bodnar, G. Zhang, T. Tanaka, E. Kiss, G. Woynarovich and H. Katoh, A study on the decomposition of volatile organic compounds by pulse corona. J. Electrostat. 40-41, 687-392 (1997.

[12] Yan, J.H., C.M. Du, X.D. Li, B.G. Cheron, M.J. Ni and K.F. Cen,2006. Degradation of phenol in aqueous solutions by gas-liquid gliding arc discharges. Plasma Chem. Plasma P., 26(1), 31-41.

[13] Sun, B., M. Sato and J. S. Clement, 1997, Optical study of active species produced by a pulsed streamer corona discharge in water. J. Electrostat., 39(3), 189-202 .

[14] *www.cc.ntut.edu.tw/~wwwoaa/oaa-nwww/oaa-bt/bt-data/97_phd/paper/15.pdf*

by HH Cheng. Liquid-phase non-thermal plasma technology for degradation of two high strength phenols in aqueous solution

Characterization of Copper-Based Shape Memory Alloy with Zinc and Aluminum

Ana Kostov[1], Aleksandra Milosavljevic[2], Zdenka Stanojevic Simsic[3], Corneliu Craciunescu[4]

[1,2,3]Mining and Metallurgy Institute Bor, Zeleni bulevar 35, 19210 Bor, Serbia
[4]Politehnica University of Timisoara, Bd. Mihai Viteazul 1, RO-300006 Timisoara, Romania

Abstract— *Copper-based shape memory alloy with zinc and aluminum was manufactured, plastically deformed, heat treated and characterized in terms of physico-mechanical, structural and micro-structural investigation. Typical martensitic microstructure with twins is revealed by optical and electron microscopy. The presence of the martensite in the structure was further confirmed through X-ray diffraction. Toughness and hardness of the alloy are investigated too. Optimal properties are obtained for the condition of the alloy that was subjected to heat treatment according to the following scheme: annealing at 850 ^{0}C and 900 ^{0}C (10 min) + quenched in water + aging at 400 ^{0}C (1 hour) + air cooling.*

Keywords— shape memory, SEM-EDS, hardness, copper-zinc-aluminum alloy, martensitic structure.

I. INTRODUCTION

The effect of shape memory is ability of some metals and alloys deformed in martensite state or at temperature interval of martensitic transformation to regain their original shape during the heating process due to complete or almost complete absence of deformation [1,2].

The heating process causes restoration of crystals in high-temperature phase called beta or parent phase and the removal of plastic deformation. In the same time, all physical and mechanical properties are restored.

During the shape recovering process, the alloys can produce a displacement or a force, or combination of the two, as a function of temperature. The starting force of recovering shape process is difference between free energies of parent and martensitic phases during the reverse transformation. The complete shape recovering is only notice if the martensitic transformation is crystallography reverses and if the deformation process is done without plane shearing [2,3].

Shape memory effect has been studied for many binary and ternary alloys, as well as for some pure metals. However, wide application can be found only for nitinol (Ni-Ti alloys) and copper-based alloys that show shape memory effect. Copper-based alloys, compared to nitinol alloys, possess somewhat lower mechanical properties due to their larger grain size and elastic anisotropy [4]. But, they can be improve, considerably without deterioration of shape memory effect, by small grain, method of rapid solidification, sinter metallurgy or by adding the elements such as Zr, V, B, Ti, Cr, etc. [5].

II. COPPER-BASED SHAPE MEMORY ALLOYS

Copper-based alloy with shape memory effect are very commercial and they are mainly alloys with zinc, aluminum and nickel. Figure 1 shows the liquidus projection in copper-based alloys with zinc and aluminum, while the Table 1 gives a review of the possible invariant reaction in the same system of alloy [6].

TABLE 1
CALCULATED INVARIANT REACTIONS IN Cu-Zn-Al SYSTEM OF ALLOY

Reaction	Temperature, K	Composition of liquid phase
L+θ→(Al)+τ	698	Cu8,6Zn50,5Al40,9
L+τ→(Al)+ε	694	Cu6,8Zn60,1Al33,1
L→(Al)+(Zn)+ε	654	Cu1,6Zn87,2Al11,2
L+β→ε+τ	917	Cu27,4Zn39,5Al33,1
L+η→τ+θ	853	Cu31,2Zn2Al66,8
L+ε`→τ+η	893	Cu34,3Zn2Al62,8
L+β→τ+ε`	1010	Cu43,5Zn6,9Al49,6
L+γ°→β+γ	1226	Cu56,4Zn28,6Al15
L+γ+γ°→β	1197	Cu54,6Zn12,6Al32,8

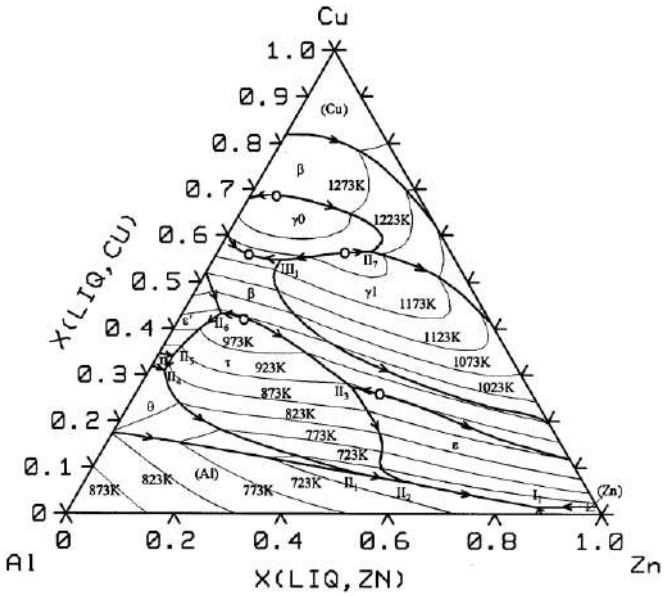

FIGURE 1. CALCULATED LIQUIDUS PROJECTION IN Cu-Zn-Al SYSTEM OF ALLOY

The possibility of shape memory effect depends upon the alloy ability to undergo the thermo-elastic martensite deformation. The alloy is first cooled and transferred to the martensitic phase, when there is possibility of mechanical deformation. As long as the lower temperature, the alloy is deformed or if heated, martensite again deformed into the austenite and the alloy returns to its original shape.

Martensitic transformation does not occur at a certain temperature, yet there is whole temperature range which is different for each monitored system.

Various deformation temperatures and the corresponding voltage curves for copper-based alloy with zinc and aluminum are shown in Figure 2.

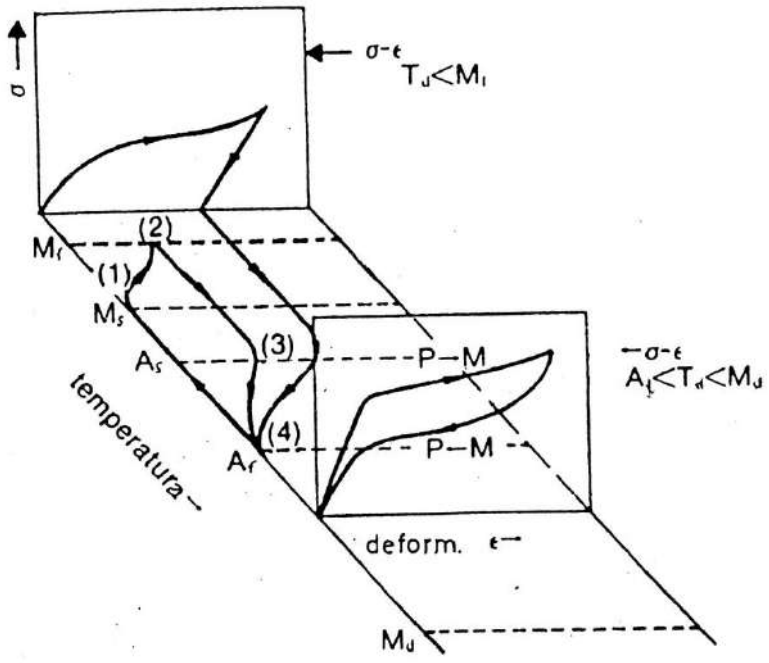

FIGURE 2. SCHEMATIC OVERVIEW OF THE VOLTAGE CURVES DEPENDING ON DEFORMATION TEMPERATURE (MS-TEMPERATURE OF BEGINNING MARTENSITE FORMATION AT COOLING; MF-TEMPERATURE OF THE MARTENSITIC TRANSFORMATION ENDING; AS-STARTING TEMPERATURE OF HIGH TEMPERATURE PHASE FORMATION; AF-ENDING TEMPERATURE OF HIGH TEMPERATURE PHASE FORMATION AT HEATING; MD-BELOW THIS TEMPERATURE MARTENSITE CAN BE REVERSED INTO THE ORIGINAL PHASE)

In the upper left corner in Figure 2, the alloy deformation below the Mf temperature is shown, while alloy is fully in martensitic condition. For a relatively low stress there is a possibility when the deformation can be deposited in the martensite structure at certain stress. When unloading once, the elastic distance can be observed in any metal. Heating to Af temperature, martensite with added deformation disappears and the original structure returns.

In contrast, in the lower right corner in Figure 2, the curve corresponding to the alloy deformed between the temperatures the Af and Md is shown, while the alloy is in the initial phase at high temperature. Here is a tensile martensite before the applied deformation (P→M). After release, martensitic structure is unstable and is converted to the original phase (P←M). During this reversible process each deformation which was incorporated into the tensile-martensite disappears and the material returns to its original shape. This behavior of materials was called the pseudo-elasticity.

Copper-based shape memory alloys with zinc and aluminum are widely used in the industry as thermostats, control equipment, connectors, etc. The most obvious examples are the various types of springs with different systems for remote regulation and control. The shape memory alloys based on copper also have wide applications in home use as constitutive elements of various assemblies. Their great advantage over the other types of smart materials alloys is low price, as well as the role of environmental friendly materials.

III. EXPERIMENTAL

The copper-based shape memory alloy with zinc and aluminum are usually obtained by classical method of melting, casting and manufacturing. Generally, all alloys with martensite structure have heavy plastically deformation, which is consist of few cycles of rolling at hot and drawing at cold with series of intermediate annealing treatments, from ingots to rods and wires of small cross-section. However, it is necessary to keep chosen composition of alloy during the production process, which is difficult by zinc evaporation during casting process. Also, plastically deformation of these alloys is heavy, with a lot of operations of rolling, drawing and intermediate annealing treatments.

Because of that, the copper-based shape memory alloy with zinc and aluminum is obtained by using technology of continuous casting of wire and profiles of small diameters, which is developed in Mining and Metallurgy Institute Bor for some pure metals [7].

The principle of this method of continuous casting is used the procedure of crystallization above the melt for directly obtaining of the copper-based shape memory 8 mm wire. The principle of technology is as follows [7]: The cooler for copper-based shape memory wire casting is dipped into the melt to the depth of h. The protection shell made of heat-resistant material, which does not react with molten alloy and layer of heat-insulation material, protect the cooler from the influence of the melt and high temperatures. Hydrostatic pressure of surrounding melt drives the molten alloy into graphite crucible. The molten alloy hardens in the crucible by heating exchange through primary part of the crystallizer, which is water-cooled. Hardened wire leaves graphite crucible at a high temperature. For prevention of oxidation of cast wire caused by high temperature on its surface, vacuum is used. Apart from above mentioned role, vacuum serves also for provision of required differential pressure inside cooler, which enables penetration of molten alloy into graphite crucible. For prevention of oxidation of cast wire after leaving the cooler, temperature on its surface should be below 60 ^{0}C. Cooling provides this cast wire in the secondary part of crystallizer. Cast wire drawing is done according to the drag-pause schematic. Process stability is ensured by adjustment of wire drawing speed and heat removal from its side surface.

IV. RESULTS AND DISCUSSION

The chemical composition of obtaining 8 mm wire is: Cu-69.7%, Zn-26.3% and Al-4%. The samples of wires are treated in the aim to obtain the wire of 1.8 mm with the shape memory effect as follows: 2 h of homogenization at 800 ^{0}C in low oxidation atmosphere, then drawing to the dimension 4x4, with thermal treatment: 15 min of annealing at 400 ^{0}C, quenching in water, 120 min annealing at 550 ^{0}C, cooling in furnace to 450 ^{0}C and air cooling and drawing to the dimension 1.8 mm. In the aim to reach the martensite structure, samples are heating 5 min in nitrogen atmosphere at 800 ^{0}C and quenched in cold water and in martensite state the alloy was memorized.

In the aim to determine the characteristics of obtained shape memory alloy, investigations of mechanical properties, structural and micro-structural analysis, as well as SEM-EDS and X-ray are done. Obtained results are shown in Table 1 and Figs 3-8 respectively.

TABLE 2
RESULTS OF PHYSIC-MECHANICAL PROPERTIES TOUGHNESS AND HARDNESS BY VICKER'S METHOD

N^0	Condition of materials	Toughness	Hardness
		J/cm^2	HV
0	As-cast condition	20	314
1	Hot-rolled at 850 ^{0}C	40	354
2	Annealing at 850 ^{0}C (10 min), quenched in water	34	379
3	Annealing at 900 ^{0}C (10 min), quenched in water	33	368
4	(2.) + ageing at 400 ^{0}C (1 h) + air cooling	22	492
5	(2.) + ageing at 450 ^{0}C (1 h) + air cooling	16	475
6	(2.) + ageing at 500 ^{0}C (1 h) + air cooling	26	448
7	(2.) + ageing at 450 ^{0}C (1 h) + cooling in furnace	21	454
8	(3.) + ageing at 400 ^{0}C (1 h) + air cooling	20	504
9	(3.) + ageing at 450 ^{0}C (1 h) + air cooling	19	478
10	(3.) + ageing at 500 ^{0}C (1 h) + air cooling	18	464
11	(3.) + ageing at 450 ^{0}C (1 h) + cooling in furnace	23	479

According to the results of mechanical investigation shown in Table 2, it is noticed that optimal characteristics of alloy are obtained for the follow state of materials: annealing, quenched in water, ageing at 400 ^{0}C 1 hour, and then air cooling. This conclusion is verified by metallography, Figs. 3-8.

FIGURE 3. MICROSTRUCTURE OF AS-CAST ALLOY, (X960)

FIGURE 4. MICROSTRUCTURE OF ALLOY, HOT DEFORMED (X960)

FIGURE 5. MICROSTRUCTURE OF ALLOY, ANNEALED AT 850 ^{O}C FOR 10 MIN AND WATER QUENCHED (X960)

FIGURE 6. MICROSTRUCTURE OF ALLOY, ANNEALED AT 900 ^{O}C FOR 10 MIN AND WATER QUENCHED (X960)

FIGURE 7. MICROSTRUCTURE OF ALLOY QUENCHED FROM 850^{O}C AND AGED AT 400^{O}C FOR 1h (X960)

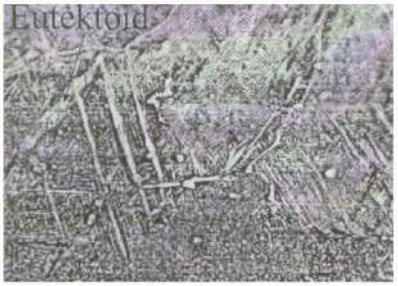

FIGURE 8. MICROSTRUCTURE OF ALLOY QUENCHED FROM 900^{O}C AND AGED AT 400 ^{O}C FOR 1h (X960)

Microstructure of cast alloy consists of a lot of big bright crystal α-solid solution in the dark basically β-crystals (Fig. 3). In appearance, this structure corresponds with the martensite structure with notable locality Widmanstatten structure. This structure is not favourable for cold plastic deformation, because the present structure is very brittle, and therefore the only possible deformation is at elevated temperatures.

Hot-processed alloy sample consists of bright crystals of α-solid solution surrounding the crystals of dark β-phase. Between the crystals of α-solid solution in the dark based β-phase particles extracted notice precipitate, but in a very small volume shares (Fig. 4). Compared to as-cast structure, the microstructure is somewhat finer, because the α-solid solution is better deployed in the β-base as a result of deformations in hot condition.

The microstructure of annealed state of alloy is given in Figures 5 and 6. It is noted that the large polygonal grains formed with the present of eutectoid and precipitate deposited on the grain boundaries. Due to higher temperatures (Fig. 6) there was a complete transformation of martensite structure.

Microstructure of aging state of alloy consists of large polygonal grains with separate participate and eutectoid on the grain boundaries. In the sample of alloy that is quenched in water from 850 ^{0}C observed the appearance of residual martensite structure with a fine needle (Fig. 7), while the sample quenched from 900 ^{0}C and subsequently ageing at 400 ^{0}C, noted the presence of residual martensite and eutectoid, but there has been a phenomenon of thermal deposition in the grain boundaries and within each grain (Fig. 8). In this sample the observed martensite structure with Widmanstatten schedule, since the α-solid solution separated in the form of martensitic needles.

The typical martensite twins were also observed on scanning electron microscope image (Fig. 9 and Fig. 10), while the elemental analysis (EDS) detailed in Fig. 11 locates the manufactured alloy in the compositional range for the shape memory alloys in the Cu-Zn-Al system.

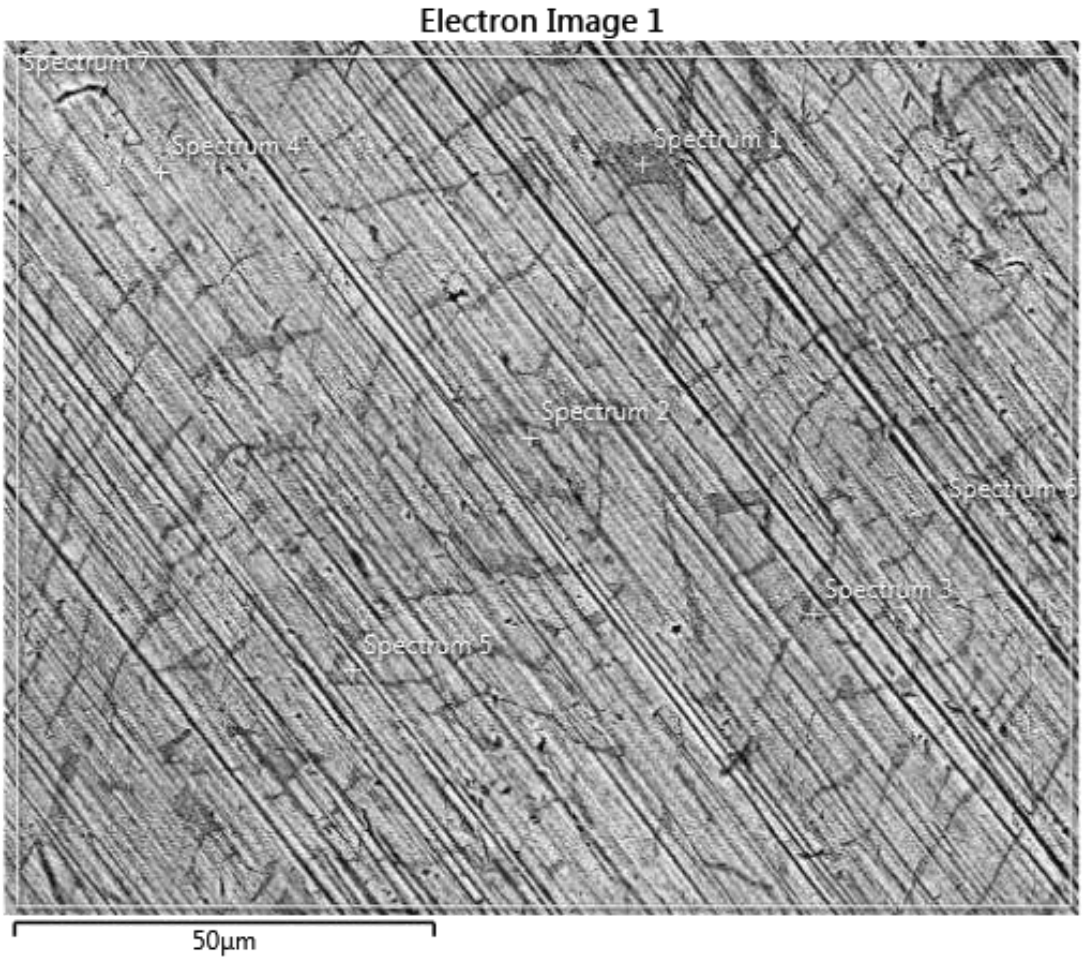

FIGURE 9. SEM OF ALLOY QUENCHED FROM 900 ^{0}C AND AGED AT 400 ^{0}C FOR 1 h

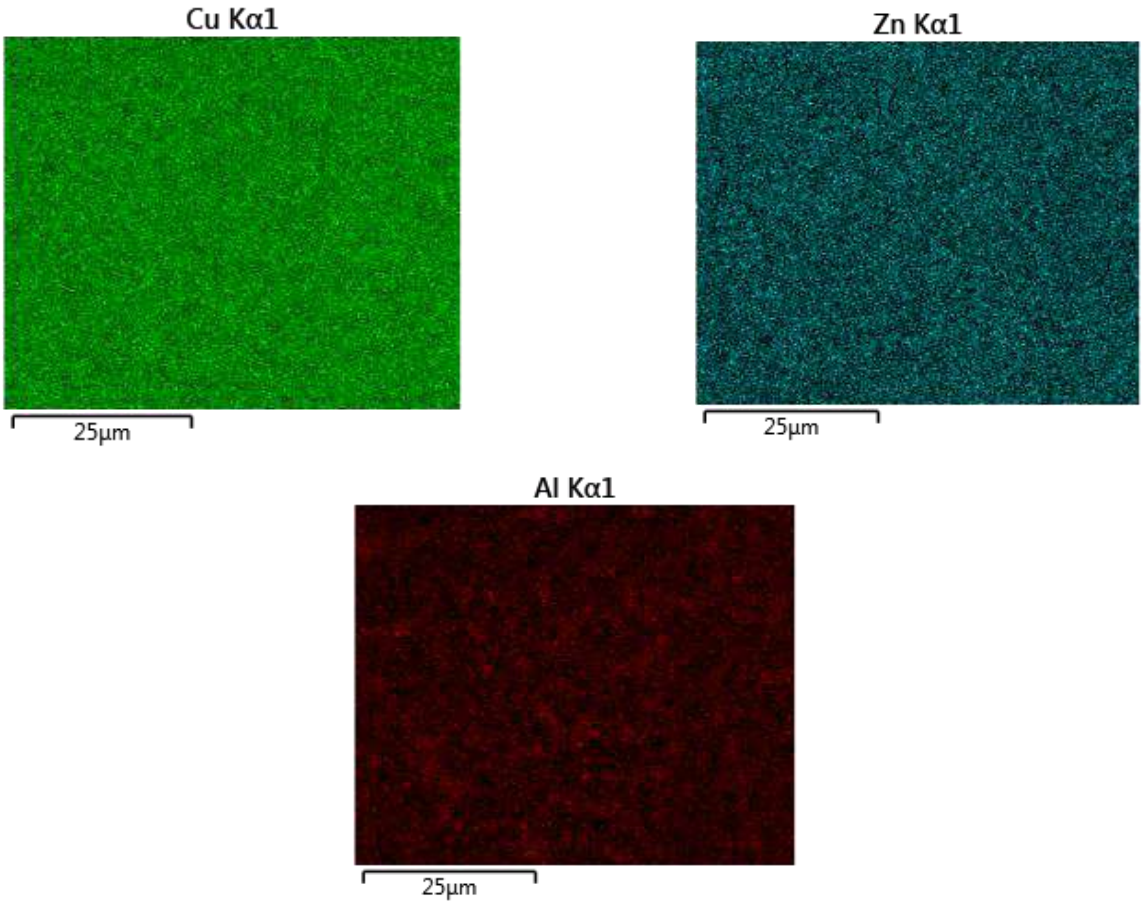

FIGURE 10. SEM MAP OF BASED ELEMENTS OF ALLOY QUENCHED FROM 900 ^{0}C AND AGED AT 400 ^{0}C FOR 1 h

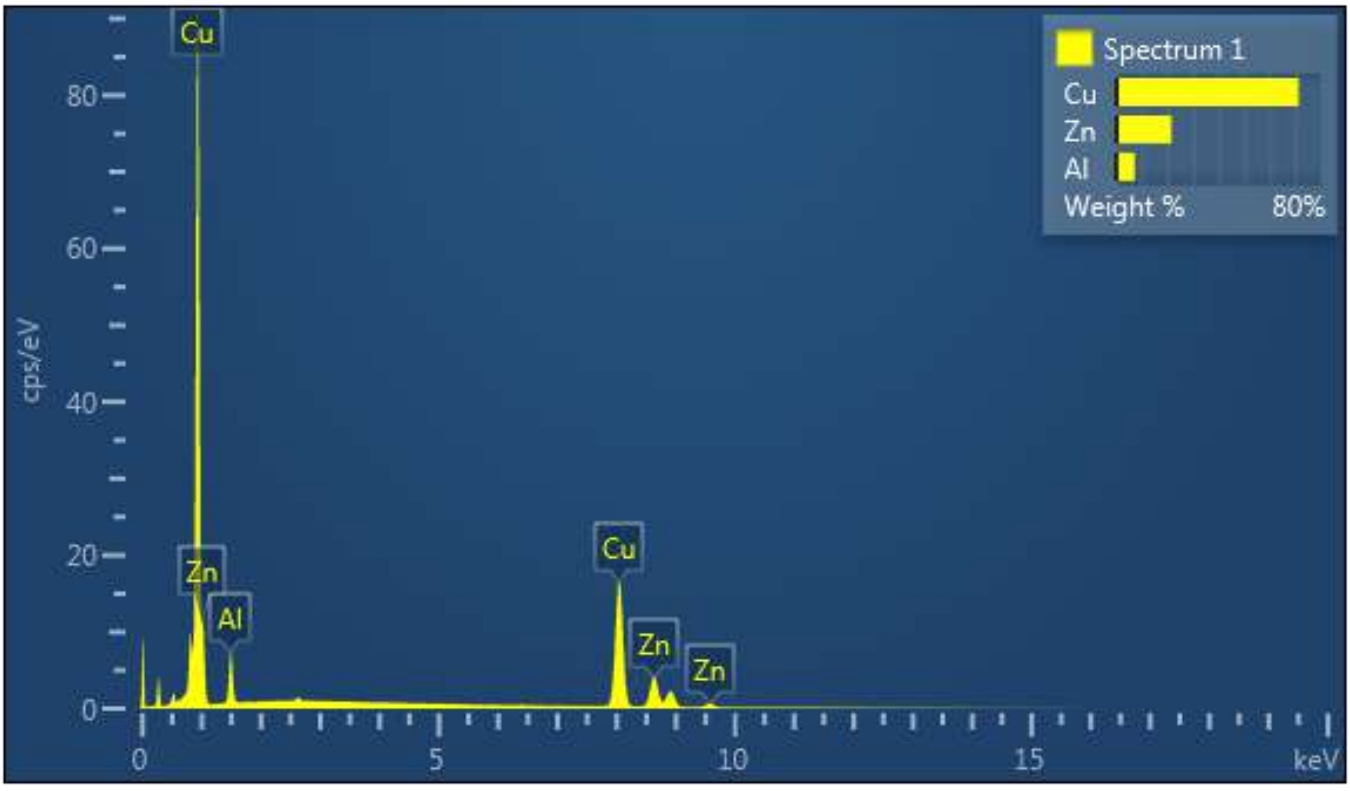

FIGURE 11. EDS ANALYSIS OF THE INVESTIGATED ALLOY QUENCHED FROM 900 ^{0}C AND AGED AT 400 ^{0}C for 1 h

The X-ray diffraction data collected for the quenched sample of alloy, showed in Fig. 12 indicates a predominantly martensitic structure, with the relevant peaks in the 40o to 45o 2θ range.

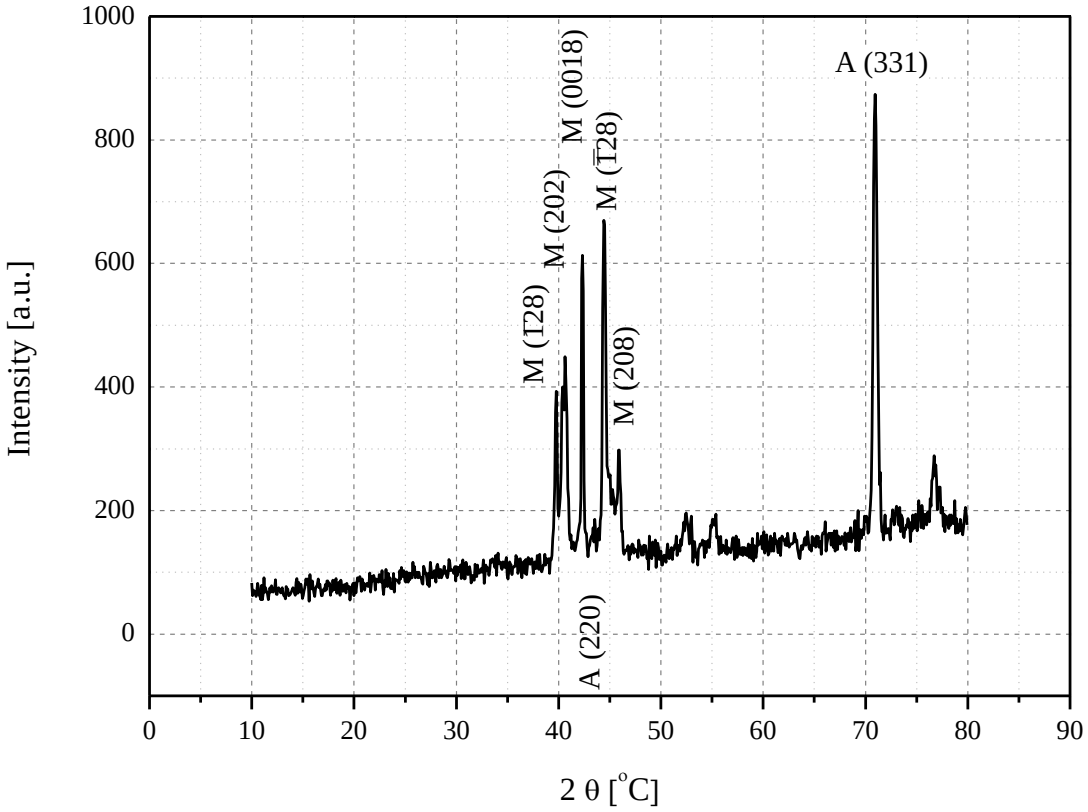

FIGURE 12. X-RAY DIFFRACTOGRAM OF THE QUENCHED ALLOY

V. CONCLUSION

The copper-based shape memory alloys with zinc and aluminum was manufactured, plastically deformed, heat treated and characterized in terms of physic-mechanical, structural and micro-structural analysis.

Quenching in water, following heating at 850 ^{0}C and 900 ^{0}C, lead to the observation of a typical martensitic microstructure, with twins revealed by optical and electron microscopy.

The presence of the martensite in the structure was further confirmed through X-ray diffraction.

Severe plastic deformation lead to an increase of the the hardness compared to the undeformed samples, a more pronounced increase was observed for the quenched samples.

Establishing a correlation between the state of the material, microstructure and mechanical properties it can be concluded that the combination of thermo-mechanical processing regime, can achieve such a state of the material that provides good mechanical properties.

By reducing the particle size α-solid solution of hot processing increases the hardness and impact toughness compared to the as-cast state.

Heat treatment of hot-processed alloy increases the hardness, while the impact toughness gradually decreases as the microstructure can be explained by the appearance of brittle phases, as a result of thermal deposition.

Optimal properties are obtained for the condition of the material that was subjected to heat treatment according to the following scheme: annealing at 850 ^{0}C and 900 ^{0}C (10 min) + quenched in water + aging at 400 ^{0}C (1 hour) + air cooling.

ACKNOWLEDGEMENTS

The authors acknowledge the support by a grant of the Romania-Republic of Serbia IPA Cross-border Cooperation Programme through the Project MIS ETC No. 1328 “Pole of Collaboration in New Functional Alloys”

REFERENCES

[1] Schetky, M.L.: Shape Memory Alloys, Sci. American, 11 (1979) 68-76.

[2] Otsuka, K., Shimizu, K., Suzuki, Y., Sekiguchi, Y., Taki, C., Homma, T., Miyazaki, S.: Splavi s Effektom Pamjati Form, Metallurgija, Moskva, 1990, p. 123. (in Russian)

[3] Wayman, C.M.: Shape Memory Alloys, Journal of Materials, 6 (1980) 129-137.

[4] Guilemany, J.M., Gil, F.J.: Kinetic Grain Growth in Cu-Zn-Al Shape Memory Alloys, Journal of Materials Science, 26 (1991) 4626-4628.

[5] Kostov A., Zivkovic Z.: Thermo-Dilatometry Investigation of the Martensitic Transformation in Copper-Based Shape Memory Alloys, Thermochimica Acta, 291 (1997) 51-57.

[6] Liang H., Chang Y.A.: A Thermodynamic Description for the Al-Cu-Zn System, Journal of Phase Equilibria, Vol.19, No.1 (1998) 25-37.

[7] Arsenovic, M., Kostov A.: Continuous Casting of Small-Cross Section Profiles, Naucna knjiga, Beograd, 2001, (in Serbian).

Simultaneous analysis of nitro compounds by Voltammetric method combined with the partial least squares (PLS) and the principal component regression (PCR)

Khuat Hoang Binh[1], Tran Van Chung[2], Nguyen Thu Huong[3], Ta Thi Thao[4]
[1,2,3]Institute of Chemistry and Material
[4]VNU - University of Science

Abstract**—** *Nitro aromatic compounds exhibit a strong electrochemical behavior on hanging mercury drop electrodes (HMDE). The ability to simultaneously determine 6 nitro compounds including nitrobenzene (NB), 2-nitrophenol (2-NP), 3-nitrophenol (3-NP), 4-nitrophenol (4-NP), 2,4- dinitrophenol (DNP) and trinitrophenol (TNT) in the same samples was investigated by differential pulse Voltammetry. The method is based on the electrochemical process at HMDE in acetate buffer of pH 4.6. It was found that peak potentials of voltammetric reduction waves of NB, 2-NP, 3-NP and 4-NP appeared at - 0.332, - 0.281, - 0.311 and - 0.387 V respectively. Under the same conditions there are three peak potentials at -0.131, - 0.227, - 0.332 V for TNT and two peaks at tại - 0.221, - 0.332V for DNT. The peaks of these compounds are very close together. Due to the serious overlapping of Voltammetric peaks of these compounds in the mixtures, so that by a conventional Voltammetry it not possible to individually determine each compound. In this study, linear multivariate regression methods such as partial least squares (PLS), principal component regression (PCR) was used to resolve the overlapped Voltammograms. The obtained relative standard errors of both methods are within ± 10%. The PLS (10.8% RSEt) results in data better than PCR (11.8% RSEt).*

Keywords**— Nitrobenzene, 2-nitrophenol, 3-nitrophenol, 4-nitrophenol, Dinitrotoluene, Trinitrotoluene.**

I. INTRODUCTION

The simultaneous determination methods of the nitro - compound mixtures in the environmental samples have received considerable attention, because they are widely used to in industries to control the pollution of individual pollutants present in waste water. The high level toxicity of nitro- compounds and their propagation through environment are capable of polluting land, water, air and affecting on human, animal health, fish, aquatic organism and other life forms. There is a variety of analytical methods applied to determine these compounds including performance liquid chromatography (HPLC), UV-vis spectrophotometry and electrochemistry. These methods are often complex and time consuming and requiring sample pretreatments involving separation, extraction before analyzing [3-7]. For the Voltammetric methods, due to the serious overlapping of their reductive peak potentials caused by the general structural formula, the nitro-compounds cannot be quantitatively determined individually. Therefore these methods are usually limited to analyzing a single chemical composition or determining the sum of the nitro compounds in the mixtures [1,2,5-7].

In this study, linear multivariable regression methods such as partial least squares (PLS), principal component regression (PCR), (applying mathematical, statistical, graphics methods, etc) were applied for experimental planning, optimization of obtained experimental data used to resolve the overlapped Voltammograms of nitro-compounds [4]. Based on the PLS and PCR models, each nitro compound such as NB, 2-NP, 3-NP, 4-NP, DNT and TNT was simultaneously determined from Voltammograms of their mixtures.

II. EXPERIMENTAL PART

2.1 Chemicals and apparatus

- **Chemicals**

Chemicals such as TNT, DNT, 2-NP; 3-NP; 4-NP (in solid form) and NB (in liquid) with analytical purity imported from China. The stock solutions contained 100 mg /L of the nitro-compounds (TNT, DNT, 2-NP; 3-NP; 4-NP) were prepared by

accurately weighing 0.100 g of each dissolved them into 1 liter volumetric flask with twice distilled water. NB solution was prepared by adding 83.40 mL NB into 1 liter volumetric flasks with twice distilled water.

The other chemical solutions : NH_4OH, CH_3COOH, CH_3COONH_4 with the analytical purity were available in the LAB.

- **Apparatus**
  - Metrohm 797 Computed Electron Analyzer using three-electrode cell, including an HMDE, an Ag–AgCl reference electrode and a platinum were auxiliary electrode.
  - pH measurements were made with pH INOLAB (Germany).

2.2 Experimental procedures

Add a suitable volume of solution each containing a nitro-compound, 0.1 mL of acetate buffer solution (pH 4.6) into an electrochemical cell and diluted to 10 mL with twice distilled water. The solution was purged with pure nitrogent for 120 s to remove soluble oxygent before analyzing. The electrochemical behaviors as well as optimal condition for the determination by Voltammetry of some nitro- compounds were studied in the previous work [1]. The DPV was applied with the parameters such as the potential range from 0,0 to - 0.6 V; scan rate of 12.5 mV/s; pulse amplitude of 50 mV; stirring rate of 2000 rpm, 4- mercury drop size;15 s rest. The analytical samples were prepared including 6 nitro compounds with the predetermined concentration. The concentration of each of nitro-compound denoted independent variables X, the analytical information of maximum peak current at different potential denoted Y parameters respectively. Basing on the obtained data, a relation function between Y and X was established used for analyzing each component in their mixtures [4]. The PCR is used to process with the signal matrix to find the principle component (PC) number, while PLS model is applied to process both data sets of X and Y independently, then the orthogonal matrix T of X and Y would be found and PC and by this way the regression coefficients of the model might be calculated. For each multivariate regression model, its correctness was established by the following expression.

Relative standard error (RSE):

$$RSE(\%) = 100\sqrt{\frac{(\sum_{j=1}^{N} C_j - \hat{C}_j)^2}{\sum_{j=1}^{N} (C_j)^2}}$$

Here N is the number of samples, C_j is the concentration of the j^{th} compound in the mixture, C_j is the concentration calculated from the regression equation

The sum of the relative standard error (RSEt) of N samples is given as following expression.

$$RSE_t = 100\sqrt{\frac{\sum_{i=1}^{M}\sum_{j=1}^{N} (C_{ij} - \hat{C}_{ij})^2}{\sum_{i=1}^{M}\sum_{j=1}^{N} (C_{ij})^2}}$$

C_{ij} is the concentration of the component i in the sample, $\hat{C}_{ij}$ is the concentration calculated from the regression equation.

III. RESULTS CONCLUSION

3.1 Electrochemical characteristics of the reduction process of nitro - compounds

3.1.1 Electrochemical characteristics

The Voltammograms of the nitro-compounds were measured resulting in (Fig,1)

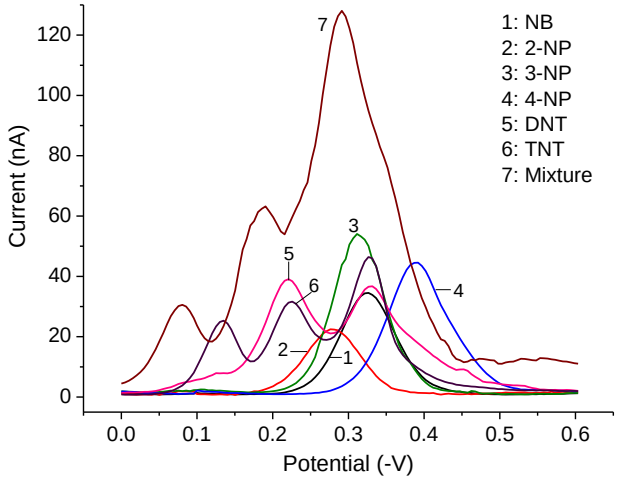

FIG 1: THE VOLTAMMOGRAMS OF NB, 2-NP, 3-NP, 4-NP, DNT, TNT (1PPM) AND THEIR MIXTURES

The Fig.1 showed that electrochemical behaviors of the studied nitro - compounds under the concrete conditions appeared the maximum peak currents such as NB, 2-NP, 3-NP, 4-NP at *0.332, - 0.281, - 0.311 and* - 0.387 V, three TNT peaks at - 0.131 (TNT1), - 0.227 (TNT2), - 0.332 V (TNT3) and two DNT peaks at - 0.221 (DNT1), - 0.332 V (DNT2), respectively.

It can be seen that peak potentials of these components are very close together and there is serious overlapping between the Voltammogram lines so each component can not be individually identified in the same mixture unless combined with the use of linear multivariate regression to simultaneously determine them.

3.1.2 Determination of the linear concentration range of nitro - compounds

Basing on the linear calibration of peak maximum height versus concentration of single nitro – components (not given here), and using the 6.0 Origin software the analytical characteristics of 6 nitro - compounds are presented in Table 1.

TABLE 1
THE LINEAR CONCENTRATION RANGE OF EACH NITRO – COMPOUND

Nitro-compounds	NB	2-NP	3-NP	4-NP	DNT (2peaks)		TNT (3peaks)		
					DNT1	DNT2	TNT1	TNT2	TNT3
Linear range, ppm	0.02-3.0	0.02-3.0	0.02-3.0	0.02-3.0	0.05-1.5	0.05-2.0	0.20-3.0	0.10-3.0	0.10-2.0
R^2	0.998	0.998	0.999	0.998	0.998	0.999	0.997	0.997	0.998
LOD, ppm	0.0045	0.0061	0.0033	0.0021	0.0062	0.004	0.0136	0.0053	0.0064
LOQ, ppm	0.0149	0.0202	0.0111	0.0071	0.0208	0.0132	0.0454	0.0176	0.0215

3.2 Multivariate regression equation

The multivariate regression equation was established based on PCR, PLS models. The concentration matrix (20 x 6) was established from the experimental data of 20 standard samples simultaneously containing 6 nitro- compounds such as NB, 2-NP, 3-NP, 4-NP, DNT and TNT with the concentration range of 0.3-1.2 ; 0.3-1.2 ; 0.9-1.8 ; 0.6-1.5 ; 0.6-1.5 ; 0.9-1.8 ppm respectively. The Voltammetric currents corresponding analyzed concentration were measured at a given potential from 0 to -0.6 V, then basing on the measured signal matrix (PCR, 20 x 120) PLS, 20 X 120) and using MATLAB software the electrolyte concentration in the mixtures would be calculated.

3.3 Evaluation of the validity of the multivariate regression model

3.3.1 Selection of the principle components (PC) of multivariate regression

The selection of PC (n-Factor) was based on building a test matrix containing standard tests with nitro – compounds as following.

A test matrix was constructed to check the validity of the multivariate regression model. The standard tests of 15 samples containing all inclusive NB, 2-NP, 3-NP, 4-NP, DNT and TNT with their known concentrations corresponding the multivariate calibration, Table 2.

TABLE 2
CALIBRATION CONCENTRATION OF NITRO-COMPOUNDS

Samples	Concentrations (Co-ppm)					
	NB	2-NP	3-NP	4-NP	DNT	TNT
1	1.5	1.5	0.9	1.2	0.9	0.6
2	1.8	1.8	1.5	1.5	1.2	0.6
3	1.5	1.2	0.9	0.9	0.6	0.6
4	0.9	1.8	0.6	1.5	1.2	0.9
5	1.5	1.2	1.2	0.6	0.9	0.9
6	1.2	1.5	0.9	1.2	0.6	0.9
7	1.2	1.8	1.2	1.2	0.9	1.2
8	0.9	1.5	1.5	1.5	0.3	1.2
9	1.8	1.8	0.9	1.2	1.2	0.9
10	1.5	1.2	0.6	0.6	0.9	0.3
11	1.2	1.5	0.9	1.0	0.9	0.6
12	1.5	1.2	0.9	1.2	1.0	0.9
13	1.6	1.2	1.0	1.0	0.9	0.9
14	1.0	1.0	0.9	0.9	0.9	1.0
15	1.0	1.2	0.9	1.2	0.9	0.6

The experimental data represented in the signal matrixes PCR (15 x 120) and PLS (15 x 120) and with the Matlab software were used to calculate the concentration of each nitro - compound in their mixtures.

The selection of the principle components was based on the dependence of RSEt (%) versus n factors (Fig.2).

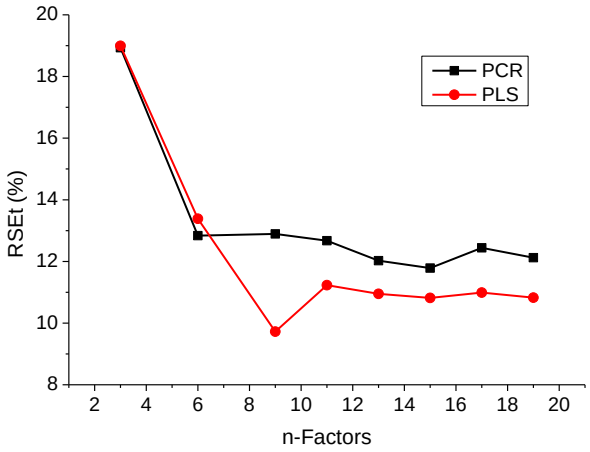

FIG. 2. DEPENDENCE OF RSET ON PC WINT PCR AND PLS

The Fig.2 showed that RSEt (%) values of both models (PCR & PLS) lower sharp from n = 6, when RSEt > 80% and RSEt > 90% from n = 8. The lowest RSEt can be obtained when n = 15 that was selected for further experiments.

3.3.2 Evaluation of the validity of the multivariate regression model

Using PC = 15 for both models PCR and PLS the relative error was calculated resulting in Table 3.

TABLE 3
THE OBTAINED RELATIVE ERRORS CORRESPONDING PC=15

Sample		Concentration (Co-ppm)					
		NB	2-NP	3-NP	4-NP	DNT	TNT
PCR	RSE (%)	11.3	12.8	12.6	12.8	8.0	10.4
	R (%)	104.1	90.4	100.7	90.5	95.9	93.5
	RSEt	**11.78**					
PLS	RSE (%)	10.4	12.1	11.8	9.9	9.7	9.3
	R (%)	105.1	107.4	99.7	94.8	92.4	93.9
	RSEt	**10.82**					

$$R : \text{Recoveries } (\%) = 100 \times \sum_{i=0}^{n} (C \text{ found}/Co)/n$$

The experimental data in Table 2. exhibited that multivariate regression method using PCR and PLS models showed good results. When PC = 15 was selected, the RSE(%) relative error of PCR components ranged from 10.4 to 12.8% and PLS was 9.3 to 12.1% respectively, TNT and DNT gave the lowest error results. The results from PLS method were better than PCR.

IV. RESULTS

The multivariate regression using partial least squared (PLS) and principle component regression (PCR) were successfully applied to simultaneously determine all 6 TNT, DNT, 2-NP compounds , 3-NP, 4-NP and NB by Voltammetric using hanging mercury drop electrodes. The relative standard errors for both methods are within ± 10%. The PLS (10.8% RSEt) has given better results than the PCR (RSEt = 11.8%). As such, PLS and PCR methods can be used to simultaneously analyze TNT, DNT, 2-NP, 3-NP, 4-NP and NB in the same mixture without separating them.

REFERENCES

[1] Khuat Hoang Binh, Tran Van Chung, Ta Thi Thao, Nguyen Thu Huong (2015), Determination of the some nitro - compounds by Voltammetric method, Journal of Chemistry, T.74/53 (5e1) pp.74-77.

[2] Tran Duc Luong, Dao Van Bay, Ho Viet Quy, Tran Van Chung (2013), Determination of nitro -benzene by Voltammetry using hanging mercury drop electrode (HMDE) Journal of Chemistry, VI, (6ABC) pp.568 – 572.

[3] Tu Vong Nghi, Tran Chuong Huyen, Pham Luan (1990), Advanced electro - chemistric analysis, VH2 program , VNU- University of Science, pp. 62-126.

[4] Ta Thi Thao (2005), Book of chemometrics, VNU- University of Science.

[5] Mohammad-Bagher Gholivand , Ali R. Jalalvand, Hector C. Goicoechea, Thomas Skov, (2014), Chemometrics-assisted simultaneous voltammetric determination of ascorbic acid, uric acid, dopamine and nitrite: Application of non-bilinear voltammetric data for exploiting first-order advantage, Talanta 119, Page 553–563.

[6] Yongnian Ni, Li Wang, Serge Kokot, (2001), "Simultaneous determination of nitrobenzene and nitro-substituted phenols by differential pulse voltammetry and chemometrics", Analytica Chimica Acta 431, Page 101–113.

[7] Youngnian Ni, PingQiu, Serge Kokot, (2005), "Simultaneous voltammetric determination of four carbamate pesticides with the use of chemometrics", Analytica Chimica Acta 537, Page 321–330.

MATLAB-Based Standalone Application for Estimation of Growth and Mortality Parameters of Fish

Ivelina Zlateva[1], Nikola Nikolov[2], Mariela Alexandrova[3]

Department of Automation, Technical University of Varna, Bulgaria

Abstract**—** *The exploited fish populations and the fishery dependent on them require regular monitoring and periodical stock assessment. The resource evaluation is crucial for definition of appropriate management strategies for rational exploitation and long-term sustainable development of the exploited stocks.*

The determination of the current state of a given stock is directly related to analysis of historical and present data concerning specific stock parameters which indicates the current status of the stock and suggests relevant definition of healthy exploitation levels. Such key stock parameters are growth and mortality rates, abundance indices, carrying capacity, maturity and reproduction, catch composition and recruitment [1,3,4,6,13,14].

The present article introduces a program system - MATLAB-based standalone application specifically developed to facilitate length-weight relationship of fish analysis outcome, growth and mortality parameters estimates and their confidence limits, normality tests of length-weight-frequency sample data, used in analysis. The proposed system incorporates statistical analysis of the overall significance of the mathematical models and results delivered, as well as methodology to overcome added computational errors in numerical analysis.

Keywords**— *fish stocks, growth and mortality parameters, MATLAB programming environment, standalone application, stock assessment.***

I. INTRODUCTION

Background

The present material introduces a MATLAB-based standalone application specifically developed to support the fish stock assessment procedure. It can be executed in MATLAB environment as well by simply typing the name of the program GR_MORT_PAR_EST in MATLAB workspace. It is focused on length-weight relationship analysis, von Bertalanffy individual growth parameters and mortality parameters estimation, based on length-frequency, length-weight frequency, length-at-age and catch-at-age samples data, by applying variety of methods introduced in fisheries science, which can be selected depending on the input data type and availability. Another incorporated feature is related to validation of the accuracy of the estimates provided by using detailed statistical analysis of the adequacy and the overall significance of the mathematical models obtained, construction of confidence intervals of the parameters estimated and validation of specific distributional assumptions of the sample data under analysis.

The below listed methods can be selected for execution in accordance with the data collected [4, 13]:

II. METHODS

2.1 Length-weight relationship analysis

2.1.1 Investigation of linear length-weight relationship model validity using linear regression analysis of L(x) as independent variable and W(y) – as a dependent variable (direct measurements)

Input Data: Length (cm) and Weight (g) measurements (length-weight frequency samples)

Deliverables: Proves or rejects validity of a linear length-weight relationship model of a kind: $W(i) = a + b * L(i)$, where: W is weight of fish, L is the length of fish and constructs confidence limits for the regression coefficients a and b. Provides graphical representation of the model fit over the actual (measured) data.

2.1.2 Investigation of non-linear length-weight relationship model validity eq. (1.0) by linear transformation of (1.0) an linear regression of log transformed length-weight data, analyzing L(x) as independent variable and W(y) – as a dependent variable

Input Data: Length (cm) and Weight (g) measurements (length-weight frequency samples)

Deliverables: Proves or rejects the validity of a model of kind: $W(i) = q * L(i)^b$, Where: $W(i)$ is the body weight of a fish, $L(i)$ is the total length and q and b are parameters, provides estimates of and q and b, once the validity of the model is justified and constructs confidence limits for the coefficient b. Provides graphical representation of the model fit over the actual (measured) data.

2.2 Estimation of growth parameters by using the Von Bertalanffy equation, which expresses the length, L as a function of the age t of the individual:

$L(t) = L_\infty(1 - exp(-K(t - t_0))$,

Where: L_∞ is the asymptotic length, K is a parameter, which describes how fast the individuals approaching L_∞ and t_0 is the initial condition parameter, or determines the time when the individual has zero length.

Input data: age readings (years) and Length measurements (cm)

Deliverables: Provides estimation of K (coefficient which shows how fast the species investigated approaches the asymptotic (infinite) length L_∞), estimates of the asymptotic length L_∞ and constructs confidence limits for the coefficient K. Provides graphical representation of the model built with the parameters estimated.

Methods for estimation of growth parameters from length at age data:

2.3 Estimation of K and L_∞ with the Gulland Holt Plot

Input data: age readings (years) and Length measurements (cm)

Deliverables: Provides estimation of K (coefficient which shows how fast the species investigated approaches the asymptotic (infinite) length L_∞) , estimation of asymptotic length L_∞ and constructs confidence limits for the coefficient K. Provides graphical representation of the model fit over the actual (measured) data.

2.4 The Ford-Wallford Plot

Input data: age readings (years) and Length measurements (cm)

Deliverables: Provides estimation of K (coefficient which shows how fast the species investigated approaches the asymptotic (infinite) length L_∞) , estimation of asymptotic length L_∞. Provides graphical representation of the model fit over the actual (measured) data.

2.5 The Chapman's method

Input data: age readings (years) and Length measurements (cm)

Deliverables: Provides estimation of K (coefficient which shows how fast the species investigated approaches the asymptotic (infinite) length L_∞) , estimation of asymptotic length L_∞. Provides graphical representation of the model fit over the actual (measured) data.

2.6 Estimation of K and t_0 with the von Bertalanffy plot

Input data: age readings (years), Length measurements (cm) and L_∞ - the asymptotic length must be a priori known

Deliverables: Provides estimation of K (coefficient which shows how fast the species investigated approaches the asymptotic (infinite) length L_∞) and t_0 (the *zero* age for the species under investigation)

Estimation of Mortality Rates

2.7 Estimation of Z (total mortality rate) by using the Linearized Catch Curve based on age composition data

Input data: age groups t (years), numbers caught per year per age groups $C_{(y,t,t+1)}$

Deliverables: Provides an estimate of Z (total mortality rate) and constructs Z confidence limits

2.8 Estimation of Z (total mortality rate) by using the Linearized Catch Curve based on length composition data

Input data: Length groups $(L_1 - L_2)$, catch in numbers per length group $C_{(L_1-L_2)}$, K and L_∞;

Deliverables: Provides an estimate of Z (total mortality rate) and constructs the confidence limits

2.9 Beverton and Holt Z-equation based on age composition data

Input data: Length groups $(L_1 - L_2)$ above chosen length $L^{'}$, catch in numbers per length group $C_{(L_1-L_2)}$, K, L_∞ and $L^{'}$;

Deliverables: Provides an estimate of Z (total mortality rate) and constructs Z confidence limits

2.10 The cumulated curve based on length composition data – The Jones Van Zalinge method

Input data: the lower value of Length groups $(L_1 - L_2)$ intervals L_1, the cumulated catch in numbers per length group $C_{(L_1,L_\infty)}$, K and L_∞

Deliverables: Provides an estimate of Z (total mortality rate)and constructs Z confidence limits

2.11 The Powell-Wetherall Method

Input data: the lower value of Length groups $(L_1 - L_2)$ intervals L_1, and $\bar{L}$ - the mean length of a fish longer than $L^{'}$;

Deliverables: Provides an estimate of Z/K, L_∞ and constructs confidence limits for the regression coefficients obtained

2.12 Estimation of M and q by using fishing effort and Z estimates

Input data: the fishing effort$f(y)$, L_c - the 50% retention length and $\bar{L}_c$ - the mean length of all individuals presented in the catch;

Deliverables: Provides an estimate of M(natural mortality rate) and q - the catchability coefficient, constructs confidence limits for M and q

2.13 Normality test of length frequency samples

Input data: Length (weight) measurements (cm);

Deliverables: the method execution render automatically a statement, based on the χ^2 normality test result for retention or rejection of the null hypothesis H_0, that the sample data follows the normal (Gaussian) distribution as automatic building of histograms and probability plots.

III. CALCULATION PROCEDURES AND ALGORITHMS USED IN THE PROGRAM SYSTEM DEVELOPMENT

Most of the methods described above are based on parameters estimation by applying linear regression analysis (methods 1 – 12) [1,4,6,13,14]. Naturally the models analyzed are best described with non-linear relationships, which are further proved linear in the model coefficients on conditions and after certain linear transformations, hence easily estimable by using regression analysis. Furthermore, regression analysis estimates the parameters of the regression equation that best describes the relationship between two variables. In this case, "best" is defined in terms of the linear regression equation that minimizes the sum of squared errors of prediction and, therefore, maximizes the coefficient of determination. The program system is developed in a manner not only to render automatically parameter estimates and mathematical models, but to investigate further the overall model significance and its validity in terms of determination and adequacy of the models obtained by following the next steps:

3.1 Determine regression coefficients of the model:

$$\hat{y}_j = \sum_{i=0}^{k} b_i * f_{ji} + \varepsilon_j \quad (1)$$

- **Form the input-output data vectors:**

$$x = [x_1, x_2, x_3, \dots x_n]^T \text{ - input vector of the independent variable } x \quad (2)$$

$$y = [y_1, y_2, y_3, \dots y_N]^T \text{ - output vector of the dependent variable } y \quad (3)$$

- **Form the experiment matrix X and the regression matrix F:**

$$X = \begin{bmatrix} x_{11} & x_{12} & \dots & x_{1n} \\ x_{21} & x_{22} & \dots & x_{23} \\ \dots & \dots & \dots & \dots \\ x_{N1} & x_{N2} & \dots & x_{Nn} \end{bmatrix}; F = \begin{bmatrix} f_{10} & f_{11} & \dots & f_{1k} \\ f_{20} & f_{21} & \dots & f_{2k} \\ \dots & \dots & \dots & \dots \\ f_{N0} & f_{N1} & \dots & f_{Nk} \end{bmatrix} \quad (4)$$

- **Determine the coefficients b_i of the model:**

$$b = C * F^T * y \quad (5)$$

where: $C = (F^T * F)^{-1}$ is the covariance matrix, on condition that the determinant of $(F^T * F)$ must be $\neq 0$ and its condition number < 10-10^2 [2,5,11].

If matrix $(F^T * F)$ is identified ill-conditioned during the execution of the program it will automatically standardize (or normalize) the variables used in regression analysis: $x_i^{norm} = \frac{\tilde{x}_i - \bar{x}_i}{\sigma_{\tilde{x}_i}}$, where: $\tilde{x}_i$ is the raw (measured) value of the input variable, $\bar{x}_i$ is the mean and $\sigma_{\tilde{x}_i}$ is the standard deviation [7]. The analysis with implemented normalized variables prove to facilitate condition number of the matrix$(F^T * F)_{norm} < 10 - 10^2$, which in turn leads to conclusion that the algorithm delivers an approximation of the solution whose precision is no worse than that of the data or it does not introduces errors of its own [5,11].

3.2 Analysis of the overall statistical significance of the mathematical model delivered:

- **Calculate the total sum of squares Q:**

$$Q = \sum_{i=1}^{N} (y_i - \bar{y})^2 \quad (6)$$

Where $\bar{y}$ is the mean value of the output variable and is obtained with: $\bar{y} = \frac{1}{N}\sum_{i=1}^{N} y_i$

- **Calculate the partition of the sum of squares:**

$$Q_{part} = \sum_{i=1}^{N} (y_i - \hat{y})^2 \quad (7)$$

Where: $\hat{y}$ are the values of the output variable assessed by the model delivered.

- **Calculate the correlation coefficient R, which is a measure for determination of the mathematical model obtained;**

$$R = \sqrt{1 - \frac{Q_{part}}{Q}} \quad (8)$$

- **F-test of the overall model significance:**

$$F = \frac{R^2(N-k-1)}{(1-R^2)k} \quad (9)$$

The critical value $F_c(\alpha, \vartheta_1, \vartheta_2)$ is found in F-distribution table for significance level $\alpha = 0{,}05$ and degrees of freedom $\vartheta_1 = k$ and $\vartheta_2 = N - k - 1$.

If $F > F_c$, the calculated value of R is assumed significant for $\alpha = 0{,}05$, and proves that the model delivered by using the above described calculation procedure is adequate [7].

The last method of the above listed (13) - Normality test of length frequency samples is developed to justify the assumption that the frequencies in length-frequency samples used for analysis in fish stock assessment procedure follow approximately the normal distribution by using the chi-square normality or goodness of fit test.

The probability density function of the normal distribution is:

$$f(x|M,\sigma^2) = \frac{1}{\sigma\sqrt{2\pi}} exp[-\frac{(x-M)^2}{2\sigma^2}] \quad (10)$$

where: the expectation M (also median and mode) and the standard deviation σ are distribution parameters, which characterize the centre of the distribution and its scale and σ^2 is the variance of M:

$$M = \int_{-\infty}^{\infty} x.f(x)dx \quad (11)$$

$$\sigma^2 = \int_{-\infty}^{\infty}(x-M)^2.f(x) \quad (12)$$

here: $-\infty < x > \infty,\ -\infty < M > \infty,\ \sigma > 0$.

Significant and unbiased estimates of the expectation M and variance σ^2 when the sample is broken to k-intervals (where: $k \approx 1 + 3.22 * log_{10}(n)$ and n is the number of observations) are:

$$\bar{x} = \frac{1}{n}\sum_{i=1}^{k} x_i^* n_i = \sum_{i=1}^{k} x_i^*.P_i \quad (13)$$

where: $P_i = \frac{n_i}{n}$ is the empirical probability distribution function and the calculated variance:

$$S^2 = \frac{1}{n-1}\sum_{i=1}^{k} n_i.(x_i^* - \bar{x})^2 = \frac{n}{n-1}\sum_{i=1}^{k}(x_i^* - \bar{x})^2.P_i \quad (14)$$

Where: x_i^* is the mid-point of the „ *i-th*" interval, and n_i are the observed frequencies in a given interval.

Once the data is processed and the expectation and observed frequencies are calculated as per the above listed mathematical procedure, the theoretical (expected) frequencies n_{i_t} are obtained by solving:

$$f(x) = \frac{n*dl}{s\sqrt{2\pi}} exp[-\frac{(x-M)^2}{2s^2}], \text{ where } dl \text{ is the interval size.}$$

The experimental data is tested further for normality using the chi-square normality test which is being used to test if a sample of data came from a population with a specific distribution [9,10,12]:

$$\chi^2 = \sum_{i=1}^{k} \frac{(n_i - n_{i\_t})^2}{n_{i\_t}} \quad (15)$$

where: n_{i_t} are the theoretical frequencies, n_i are the observed frequencies [8].

If the calculated χ^2 value is below a critical (table) value $\chi_T^2(\nu;p)$ for significance level α, (where ν are the degrees of freedom and p is the probability) the null hypothesis is retained, stating that the sample data is taken from a population with specific distribution (normal distribution).

Algorithm block-diagrams are presented in Fig. 1 for methods 1 to 12 and in Fig. 2 for method 13.

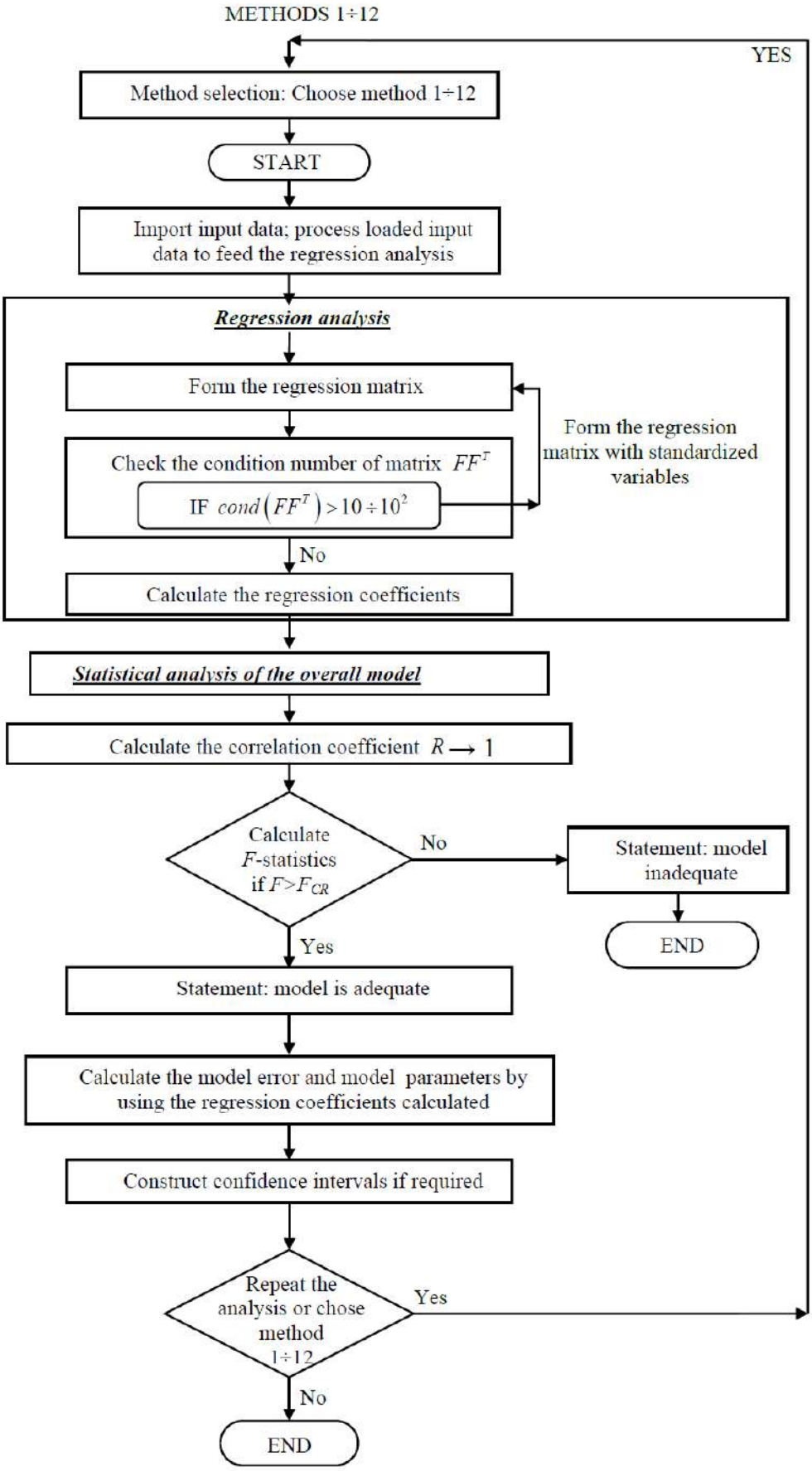

FIGURE 1. ALGORITHM BLOCK-DIAGRAM – METHODS 1 TO 12

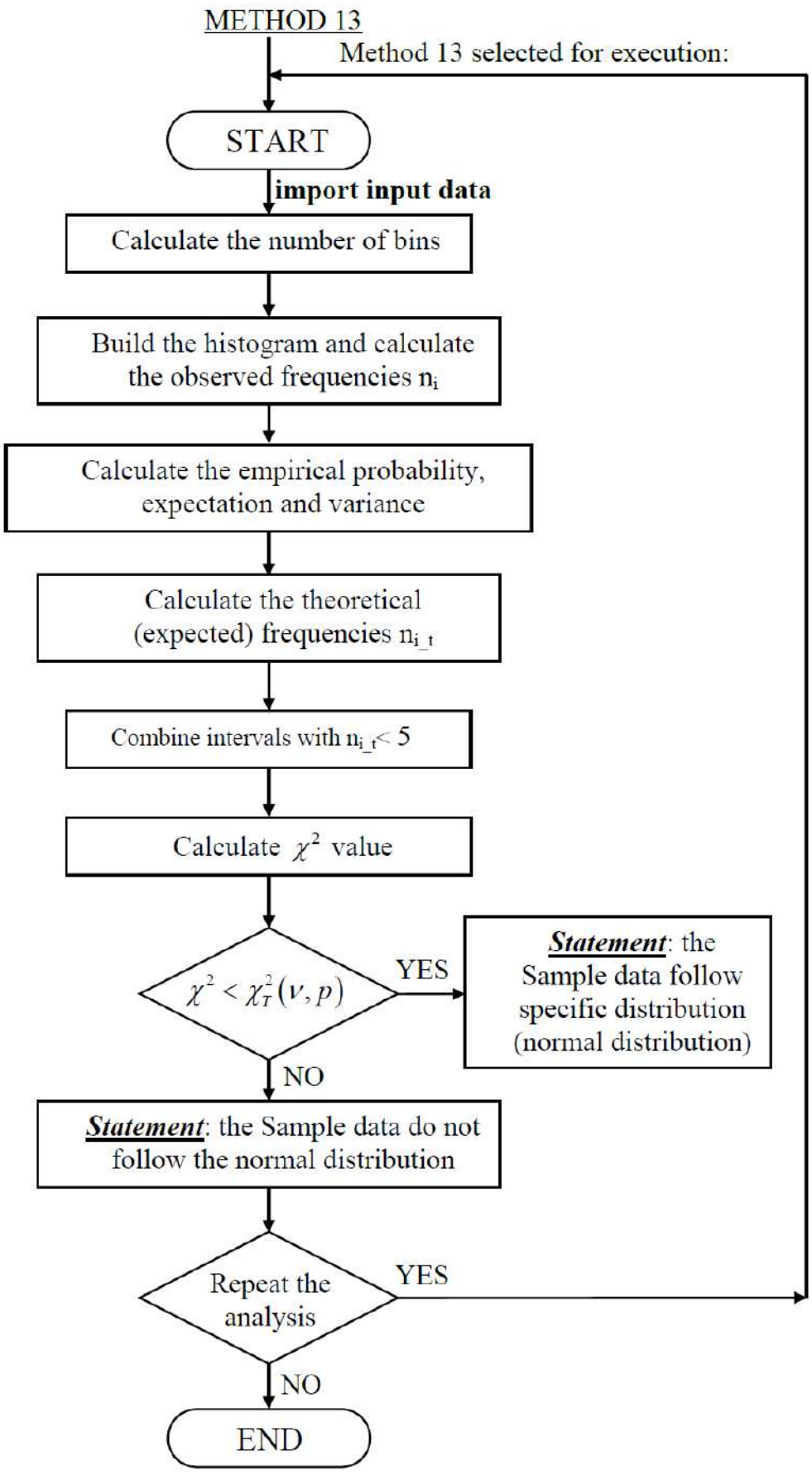

FIGURE 2. ALGORITHM BLOCK-DIAGRAM – METHOD 13

IV. GENERAL PROGRAMMING STRUCTURES IMPLEMENTED IN SCRIPT DEVELOPMENT

The selection of a chosen method is considered an execution of one or several methods selected as per the user's needs by implementation of switch - case structure:

```
SWITCH switch_expr
      CASE case_expr,
           statement, ..., statement
         CASE {case_expr1, case_expr2, case_expr3,...}
           statement, ..., statement
        ...
        OTHERWISE,
          statement, ..., statement
      END
```

Related example is given below:

```
k = input('Choose a method k= ');
switch k
case 1
again = input ('Would you like to continue with another method?(yes/no): ','s');
if( ~ismember(again,{'y','Y','yes','Yes','YES'}) )
break
end
       …….
       Case 13
       end
```

Single method execution can be repeated as many times as needed for the purpose of analysis.

The input data (observations/measurements) is considered preliminary processed and saved in .txt files and further loaded upon execution as per the example given below:

```
L = importdata('C:\Users\USER\Desktop\PS\Lanchovy.txt');%form the input vector L for the regression analysis%
W = importdata('C:\Users\USER\Desktop\PS\Wanchovy.txt');%form the outputvector W for the regression analysis%
```

If the data analyzed need to be processed to form the input-output data to feed further regression analysis, depending on the specifics of the method chosen it will be automatically processed upon execution with `for` loops and/or `if` statements (Example is given below):

```
n = r-1;
for i = 1:n
            GrR(i)=(L(i+1)-L(i))/deltat;%calculate the growth rate for time interval deltat%
            Lmean(i)=(L(i+1)+L(i))/2;%calculate the mean length reached for interval deltat%
End
```

and:

```
if (Cond_FF > maxval)
            disp('Cond FF>10 ==>')
```

```
            txt = sprintf('Cond FF>10 ==> \r\n');
            fprintf(fileID,txt);
            disp('Apply Regression analysis with normalized (standardized) variables')
            txt = sprintf('Apply Regression analysis with normalized (standardized) variables' \r\n');
            fprintf(fileID,txt);
```

The present development aims applicability and usage not only in MATLAB programming environment, but as a standalone executable application without requirements for MATLAB installation. Building a standalone application is possible with MATLAB Compiler, which can generate executable standalone files as command-line executable versions of the MATLAB code or complete applications that use MATLAB graphics and UIs designed with GUIDE. The designer of the applications can himself define the user inputs and choose how the results are presented using all the output formats which are supported by MATLAB (text, numeric, or graphical formats). End users of these applications do not need knowledge to operate in MATLAB programming environment unless they want to modify or design the applications themselves.

The program system developed is functioning as standalone application and records the results of the calculations in designated .txt file, which is organized within the program structure as given below:

```
filename =('C:\Users\USER\Desktop\PS\Results.txt');
        fileID = fopen(filename, 'a');%opens a designated .txt file to record the final and interim results (selected as per their statistical and scientific significance for the provision of the overall analysis goals%
.....
disp('Regression coefficient b1=:')
            txt = sprintf(Regression coefficient b1=: %f \r\n' ,b1);%records the calculated value of the regression coefficient in .txt file for further use and archive of analysis results%
fprintf(fileID,txt)
       fclose(fileID)%closes the file upon completion of the method chosen for execution%
```

The user will be asked to enter table and critical values of variables on purpose – either to deliver statement of the type: "the model obtained is adequate/inadequate", or to be further used for calculation of parameters. Script example is given for F-test:

```
Fcr = input('Enter F-statistics table value Fcr=');
        txt = sprintf('Enter F-statistics table value Fcr=: %f \r\n' ,Fcr);
        fprintf(fileID,txt);

        if (Fn > Fcr)
            disp('The model is statistically significant and adequate')
            txt = sprintf('The model is statistically significant and adequate');
            fprintf(fileID,txt);
        else
            disp('the model is inadequate')
            txt = sprintf('the model is inadequate \r\n');
            fprintf(fileID,txt);
        end
```

The results recorded in the designated .txt file are chosen to be displayed in accordance with the parameters significance and meaning, interim results are only displayed and recorded if they are considered important indicators to prove statistical significance and accuracy of the parameters estimated. Example of data recorded in .txt file for archive or further use and processing of data, depending on the user needs is given below:

b. Statistical analysis

Correlation coefficient value R: 0.920405

F-test the overall model significance

Calculated F-statistics value Fl= 1.263613e+003

Enter critical (table) F-statistics value Fcr=: 3.450000e+000

The model is adequate

The program performance and accuracy is tested with experimental data, simulation data and solved numerical examples [4,13].

V. CONCLUSIONS

The software developed delivers estimates of key growth and mortality parameters to support stock assessment procedure and analysis of historical and present data. It allows analysis of the overall model significance and delivers a statement for the model adequacy.

The program itself does not add computational error to the analysis results and works well with natural, standardized and log-transformed values of the variables under used for the provisions of analysis.

The methods can be repeatedly executed with new or amended data depending on the user's requirements and data availability.

In case that input data is available to feed few models, which deliver estimates of same stock/individual parameters, comparison of the estimates delivered might results in more realistic values to support the analysis.

The program is set as standalone application and it does not require MATLAB software installation to operate. In case the script needs further modifications as per the users demand it can be easily modified in MATLAB programming environment. The graphic representations dispose the same features as regular MATLAB graphs.

The results are recorded in a designated .txt file and can be further processed with other applications depending on the user needs.

REFERENCES

[1] Anderson, R. O., Neumann, R. M. 1996. Length, Weight, and Associated Structural Indices, in: B.E. Murphy and D.W. Willis, (Eds): Fisheries Techniques, 2nd edition, American Fisheries Society, Bethesda, Maryland: pp.447-481

[2] Belsley, D. A., Kuh, E., Welsch, R. E. 1980. The Condition Number. Regression Diagnostics: Identifying Influential Data and Sources of Collinearity. John Wiley & Sons, New York.

[3] Blackwell, B. G., Brown, M. L., Willis, D. W. 2000. Relative Weight (Wr) Status and Current Use in Fisheries Assessment and Management, Reviews in Fisheries Science, 8(1): pp. 1–44

[4] Cadima, E.L. 2003. Fish Stock Assessment Manual. FAO Fisheries Technical Paper. No 393, Rome, FAO, 161p

[5] Cheney, W., Kincaid, D. 2008. Numerical Mathematics and Computing, 6th edition. Thomson Brooks/Cole

[6] Froese, R. 2006. Cube law, condition factor and weight-length relationships: history, meta-analysis and recommendations. Journal of Applied Ichthyology, 22: pp. 241-253.

[7] Genov, D., 2000. Modeling and Optimization of industrial processes Manual Lab, Varna: Technical university-Varna, 192p.

[8] Hahn, G. J. and Shapiro, S.S., 1967. Statistical Modeling in engineering, New York, London, Sydney: John Wiley and Sons Inc., 376p.

[9] NIST/SEMATECH e-Handbook of Statistical Methods, 2003, last updated: 10/30/2013: http://www.itl.nist.gov/div898/handbook/03.11.2017.

[10] Papoulis, A., 2002. Probability, Random Variables and Stochastic Processes (4th Edition). New York: McGraw-Hill Higher Education p. 168.

[11] Pesaran, M. H.. 2015. The Multicollinearity Problem. Time Series and Panel Data Econometrics. New York: Oxford University Press. pp. 67–72

[12] Snedecor G.W and Cochran W.G, 1989, Statistical Methods, 8th Edition, Iowa State University Press, 491p.

[13] Sparre P. and Venema S.C. 1998. Introduction to Tropical Fish Stock Assessment - Part 1: Manual. Rome: FAO Fish Tech. Pap., 306/1 (Rev.2), 407p

[14] Whetherall, J.A., Polovina, J. J, Ralston, S. 1987. Estimating Growth and Mortality in Steady-state Fish Stocks from Lenght-Frequency Data pp 53-74, In D. Pauly and G.R. Morgan (eds.) Length-based methods in Fisheries research. ICLARM Conference proceedings 13, 468p. Safat, Kuwait.

Comparison of K-E Turbulence Model Wall Functions Applied on a T-Junction Channel Flow

G. C. C. Fiuza[1], A. L. T. Rezende[2]

Mechanical and Materials Engineering Department, IME – Military Instituto of Engineering, RJ, Brazil

Abstract**—***The flow acting in a T-junction channel is present in several industrial applications, such as air conditioning systems, water cooling circuits, gas exhaust systems and others. In order to numerically simulate this case, the Average Reynolds Navier-Stokes (RANS) equation is used for a two-dimensional stationary flow using the k-ε model together with wall functions such as standard wall function, Enhanced and Menter-Lechner wall treatments. The moment ratio used is M_R = 2 and the Reynolds number at the inlet of the flow parallel to the channel is Re = 15,000. The results were compared with the literature data using Large Scale Simulation (LES). The results obtained for k-ε model Enhanced and Menter-Lechner wall treatment were satisfactory and close to that found by the LES simulation, however, results obtained from k-ε model standard wall function presented large deviation to literature, mainly in the boundary layer and K production profiles. In general, the results presented small distortions for the profiles of turbulent kinetic energy production near walls, however, they illustrate in an analogous manner to the literature the production of turbulent kinetic energy K concentrated in the shear layers between flows. The main results analyzed in this paper are the length of the recirculation bubble, boundary layer profile, mean velocity magnitude and kinetic energy production k.*

Keywords—Turbulence, RANS, k-ε, T-Junction, Channel, LES.

I. INTRODUCTION

The main objective of the present work is the computational analysis of the geometry of a rectangular T-junction channel. In this situation, a flow parallel to the channel, called "parallel flow", enters the main channel and another flow transversal to the channel, called “jet flow”, enters the jet flow inlet. As the parallel flow approaches the inlet region of the jet stream, it bypasses the jet flow due to the high jet flow momentum. Since the parallel flow cannot penetrate the jet flow, it contours the jet flow as an obstacle. In addition, the jet flow cannot penetrate the parallel flow, curving until it becomes parallel to the parallel flow and the channel. Such changes of direction generate recirculation bubbles close to the inlet of the jet stream to the channel. This phenomenon, as illustrated in Fig. 1, has been extensively studied in the field of fluid dynamics and can be easily found in air conditioning, water cooling circuit in nuclear power plants, exhaust gas recirculation in internal combustion engines among other systems [1].

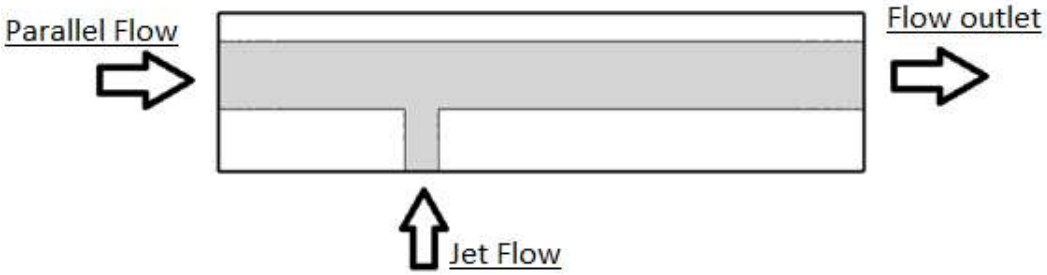

FIGURE 1: CHARACTERISTIC OF A FLOW IN A T-JUNCTION CHANNEL.

The simulations were performed based on the Reynolds Averaged Navier-Stokes (RANS) Equations with Reynolds number Re = 15,000 at the inlet of the parallel flow. The Reynolds number is defined as a function of the channel hydraulic diameter, kinematic viscosity and average flow velocity, given by (1):

$$Re = (U \times d_h)/\upsilon \tag{1}$$

where the hydraulic diameter for a rectangular channel is known according to (2):

$$d_h = (2 * H * L)/(H + L) \tag{2}$$

In order to compare the parallel flow (parallel to the channel) and jet flow (transversal to the channel), the fluid momentum ratio was used. This momentum ratio is defined as a function of the flow velocity, cross-sectional area of the channel and the density of each fluid given by (3):

$$M_R = \frac{(\rho U^2 A)_{Parallel\ \ Flow}}{(\rho U^2 A)_{Jet\ \ Flow}} \tag{3}$$

The performance of the turbulence model used for the case analysed in the present work was evaluated by comparison with the numerical results obtained by [1]. Georgiou and Papalexandris performed a numerical simulation with Re = 15.000 for the parallel flow inlet and used the Large Scale Simulation (LES) model with treatment in regions close to the wall for the analysis of a T-junction channel for flows with moment ratio of M_R= 2 and M_R= 0.5.Based on previous studies, this work presents numerical results of a T-junction channel geometry using the k-ε turbulence model in flows with moment ratio M_R= 2. The results obtained were compared with the analysis of [1].

II. MATHEMATICAL DESCRIPTION

The flow through a T-junction channel is governed by the application of the RANS Equations that describe the incompressible fluid movement. These equations are equations of conservation of momentum and continuity, being presented in (4):

$$\left(\frac{\partial u_i u_j}{\partial x_j}\right) = g_i - \frac{1}{\rho}\frac{\partial p}{\partial x_i} + \frac{\partial}{\partial x_j}\left(\upsilon \frac{\partial u_i}{\partial x_j}\right);\ \frac{\partial u_j}{\partial x_j} = 0 \tag{4}$$

The method of the average Reynolds equations is based on the decomposition of the instantaneous velocity value in the equation $u_i = \overline{u_i} + u_i'$,, where u_i represents the instantaneous velocity value, $\overline{u_i}$ the mean velocity vector and u_i' represents the velocity fluctuation vector [2]. Consequently, the mean momentum equation for non-transient and incompressible flows is given by (5):

$$\frac{\partial \overline{u_i}\overline{u_j}}{\partial x_j} = g_i - \frac{1}{\rho}\frac{\partial \bar{p}}{\partial x_i} + \frac{\partial}{\partial x_j}\left(\nu \frac{\partial \overline{u_i}}{\partial x_j} - \overline{u_i' u_j'}\right);\ \frac{\partial \overline{u_j}}{\partial x_j} = 0 \tag{5}$$

The term $\overline{u_i' u_j'}$ present in (5) is the Reynolds tensor and represents the influence of velocity fluctuations on the mean flow. However, (5) does not represent a closed system of equations, so it is necessary to determine the value of Reynolds turbulent tensor to close the system. For this, an analogy is made to Stokes's Law, based on the Boussinesq hypothesis, where the turbulent stresses are proportional to the mean velocity gradient of the flow. (6) represents the equation of the Reynolds tensor:

$$-\overline{u_i' u_j'} = \upsilon_t \left(\frac{\partial \overline{u_j}}{\partial x_j} + \frac{\partial \overline{u_j}}{\partial x_i}\right) - \frac{2}{3} k \delta_{ij}\ ;\ k = \frac{1}{2}\overline{u_i' u_i'} \tag{6}$$

The term υ_t is characterized as turbulent viscosity and is defined according to models of turbulence. There are several models of turbulence to find the term, but in this work, the k-ε model will be used.

2.1 k-ε Model

The standard k-ε model, developed by [3] and [4], is understood as a turbulence model of two conservation equations. Here two partial differential equations are solved, one for the turbulent kinetic energy k and the other for the dissipation of the turbulent kinetic energy per unit mass ε present respectively in (7) and (8).

$$\rho \frac{\partial k}{\partial t} + \rho \frac{\partial}{\partial x_j}\left(\overline{u_j} k\right) = \frac{\partial}{\partial x_j}\left[\left(\mu + \frac{\mu_t}{\sigma_k}\right)\frac{\partial k}{\partial x_j}\right] + P_k - Y_k \tag{7}$$

$$\rho \frac{\partial \varepsilon}{\partial t} + \rho \frac{\partial}{\partial x_j}\left(\overline{u_j} \varepsilon\right) = D_\varepsilon + P_\varepsilon - d_\varepsilon \tag{8}$$

where the terms P_k and Y_k are respectively the terms of production and destruction of turbulent kinetic energy k, and the terms D_ε, P_ε and d_ε are respectively the terms of diffusion, production and destruction of the specific rate of dissipation of turbulent kinetic energy per unit mass ε and the turbulent viscosity is given in (9) below:

$$\mu_t = \frac{C_\mu k^2}{\varepsilon} \tag{9}$$

C_μ is a constant with a value of 0.09, k is the turbulent kinetic energy and ε is the dissipation of turbulent kinetic energy per unit mass.Although the present model is widely used and obtains good results for simple flows with small pressure gradients, it has low precision in the vicinity of adverse pressure gradients [5].

2.2 Standard Wall Function

Law of the Wall are empirical relations used to connect the calculated quantities in the neighboring cells to the wall and the corresponding quantities in the wall. Experimentally three regions are verified in a turbulent boundary layer according to Fig. 2 below. The first layer located near the wall is called the viscous sub-layer. In this region of the flow the transport of momentum is carried out by means of molecular diffusive effects, resembling a laminar flow. In turn, the region of the logarithmic layer has as its characteristic the equivalence between the molecular and turbulent transport in the flow. Finally, the turbulent layer is fully dominated by the turbulent flow effects [6].

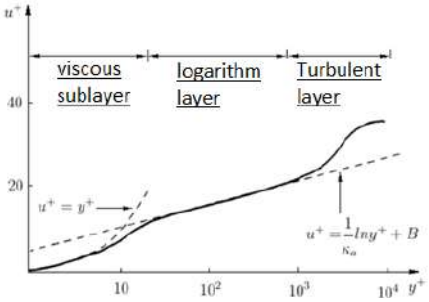

FIGURE 2: BOUNDARY LAYER PROFILE. [6]

The most common approach for near-wall velocity processing with respect to numerical simulations is performed by means of standard wall functions. By means of empirical formulations the flow is modeled in regions near the wall [7]. The standard logarithmic relation for velocity near the wall is given by (10):

$$u^+ = \frac{u_t}{u^*} = \frac{1}{k_a} lny^+ + B \tag{10}$$

where u_t is the tangential velocity to the wall at a distance Δy, k_a is the Karman constant and B is a dimensionless constant. The dimensionless distance to the wall y^+ is given by:

$$y^+ = \frac{u*y}{v} \tag{11}$$

where v is the kinematic viscosity of the fluid.The friction velocity is given by (12):

$$u^* = \sqrt{\frac{\tau_w}{\rho}} \tag{12}$$

τ_w is defined as the shear stress on the wall and ρ is the specific mass of the fluid.

2.3 Enhanced Wall Treatment

Enhanced wall treatment is a near-wall modeling method that combines the two-layer model with enhanced wall functions. If the near-wall mesh is fine enough to be able to resolve the laminar sublayer then the enhanced wall treatment will be identical to the standard two-layer zonal model. However, the restriction that the near-wall mesh must be sufficiently fine everywhere might impose too large computational requirement. Then, it is necessary the introduction of a near-wall formulation that can be used with coarse meshes as well as fine meshes in order to reduce computational costs.

2.3.1 Two-Layer Model

In the Two-Layer Model, the viscosity-affected near-wall region is completely resolved all the way to the viscous sublayer. The two-layer approach is an integral part of the enhanced wall treatment and is used to specify both dissipation of the turbulent kinetic energy per unit mass ε and the turbulent viscosity in the near-wall cells. In this approach, the whole domain is subdivided into a viscosity-affected region and a fully-turbulent region. The demarcation of the two regions is determined by a wall-distance-based, turbulent Reynolds number, Re_y defined according with 13:

$$Re_y \equiv \frac{\rho y \sqrt{k}}{\square} \tag{13}$$

where y is a distance between the wall and the cell center in normal direction given by (14):

$$y \equiv \min_{\vec{r}_w \in \Gamma_w} \|\vec{r} - \overrightarrow{r_w}\| \tag{14}$$

where $\vec{r}$is the position vector at field point, $\overrightarrow{r_w}$is the position vector of the wall boundary and Γ_w is theunion of all the wall boundaries involved.The fully-turbulent region is calculated through the turbulence models, such as k-ε model. The viscous sublayer is completely resolved by the one-equation of [8] model described in (15):

$$\mu_{t,twolaye\ r} = \rho C_\mu l_\mu \sqrt{k} \tag{15}$$

where the length scale l_μ is computed from [9] and is described in (16):

$$l_\mu = y C_l^* \left(1 - e^{-Re_y/A_\mu}\right) \tag{16}$$

The two-layer formulation for turbulent viscosity is used as a part of the enhanced wall treatment, in which the two-layer definition is smoothly blended with the high-Reynolds-number μ_t definition from the outer region, as proposed by [10]:

$$\mu_{t,enh} = \lambda_\epsilon \mu_t + (1 - \lambda_\epsilon)\mu_{t,twolayers} \tag{17}$$

where λ_ϵ is a blending function, is defined such that the function is equal to 1 far from walls and is zero very near to walls.

2.3.2 Enhanced Wall Functions

In order to introduce a formulation to be used in coarse mesh it is necessary to have a method that can extend its applicability throughout the near-wall region and thus its layers, such as laminar sublayer, buffer region, and fully-turbulent outer region. Additionally, it is necessary to formulate the law-of-the wall as a single wall law for the entire wall region. [11] proposed blending linear (laminar) and logarithmic (turbulent) laws-of-the-wall for incompressible and timeless flow using a function described in (18):

$$u^+ = e^{\Gamma} u_{lam}^+ + e^{\frac{1}{\Gamma}} u_{turb}^+ \tag{18}$$

where Γ is the blending function and is given by (19):

$$\Gamma = -\frac{0{,}01(y^+)^4}{1+5y^+} \tag{19}$$

The general equation for the derivative $\frac{du^+}{dy^+}$ is given in (20):

$$\frac{du^+}{dy^+} = e^{\Gamma} \frac{du_{lam}^+}{dy^+} + e^{\frac{1}{\Gamma}} \frac{du_{turb}^+}{dy^+} \tag{20}$$

The enhanced wall functions allow the fully turbulent law to be easily modified and extended to include other effects such as pressure gradients or variable properties. This formula also guarantees the correct asymptotic behavior for large and small values of y^+ and good representation of velocity profiles in the cases where y^+ is inside the wall buffer region ($3 < y^+ < 10$).

2.4 Menter-Lechner Wall Treatment

Although the two-layer approach is most used nowadays in industrial simulation, used in the Enhanced Wall Treatment has some drawbacks such as: the Wolfstein equation is not compatible with the ε-equation pressure gradient flows; the model tends to oscillate for a coarse mesh with a y^+, as it switches back and forth between time steps, preventing convergence; and regions with very low values of turbulence kinetic energy might easily have a small turbulent Reynolds number. Therefore, such regions will be treated with a near-wall formulation, though they might be away from the wall.

According with [12] the Menter-Lechner near-wall treatment has been developed as an alternative solution that is not based on the two-layer approach. It uses a new low-Re formulation that is designed to avoid the deficiencies of the already described two-layer approach. The objective of the Menter-Lechner near wall treatment is the use of a y^+insensitive near-wall treatment that predicts independently the wall shear stress, used as a boundary condition to the turbulence models. This treatment should switch gradually from wall functions to a low-Re formulation when the mesh is refined. This also requires a

blending of various quantities between the viscous sublayer and the logarithmic region. The wall shear stress τ_w is calculated according to the (21):

$$\tau_w = \rho u^* u_\tau \tag{21}$$

where the friction velocities u^* and u_τ are blended between the viscous sublayer and the logarithmic region accordingly with (22) and (23):

$$u^* = \left[\left(\frac{\mu U_{tan}}{\Delta y} + 0{,}3\rho k\right)\frac{1}{\rho}\right]^{1/2} \tag{22}$$

$$u_\tau = U_{tan}\left[(u^+_{lam})^{-4} + (u^+_{turb})^{-4}\right]^{1/4} \tag{23}$$

The Menter-Lechner near-wall treatment adds a source term to the transport equation of the turbulence kinetic energy k that includes near-wall effects. The standard k-ε model is modified as shown in the following equations (24), (25) and (26):

$$\frac{\partial(\rho k)}{\partial t} + \frac{\partial(\rho k u_i)}{\partial x_i} - \frac{\partial}{\partial x_j}\left[(\mu + \mu_t)\frac{\partial k}{\partial x_j}\right] = G_k - \rho\varepsilon + S_{near\ -wall} \tag{24}$$

$$\frac{\partial(\rho\varepsilon)}{\partial t} + \frac{\partial(\rho\varepsilon u_i)}{\partial x_i} - \frac{\partial}{\partial x_j}\left[\left(\mu + \frac{\mu_t}{1{,}3}\right)\frac{\partial k}{\partial x_j}\right] = 1{,}44\frac{\varepsilon}{k}G_k - 1{,}92\rho\frac{\varepsilon^2}{k} \tag{25}$$

$$\mu_t = 0{,}09\rho\frac{k^2}{\varepsilon} \tag{26}$$

The source term $S_{near\ -wall}$ added in the transport equation of k is active only in the viscous sublayer and accounts for low-Reynolds number effects. It automatically becomes zero in the logarithmic region.

III. METHODOLOGY

The present work consists in the development of the 2D geometry of a T-junction channel simulating two flows, one parallel to the channel and another transversal to the channel. The geometry of the channel is described in Fig. 3. The dimensions presented here are based on those used by [1] and are related to the width of the entrance of the jet stream δ. The value of δ used in this work is equal to 1 m. For the simulation, only the momentum ratio of $M_R = 2$ was considered. The relationship between the values of δ is present in Fig. 4, originating from the work of [1].The geometry described in Fig. 3 differs from the geometry shown in Fig. 4 in its dimension, where it is analysed here in two dimensions, and in the distance between the inlet of the parallel flow and the inlet of the jet stream and between the junction T and the inlet of the flow jet. In the present work, both distances between the inlets of both flows are 100δ and the channel thickness is 0.12m. Such a gap between the entrances is necessary for the flow to become fully developed.

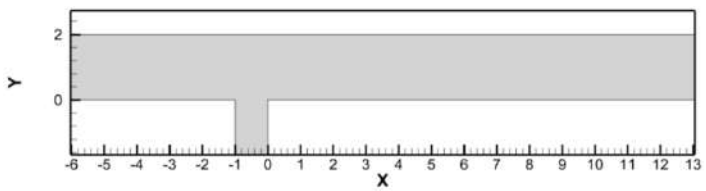

FIGURE 3: GEOMETRY USED IN THE PRESENT WORK.

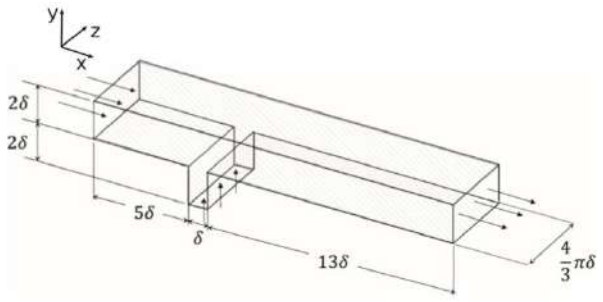

FIGURE 4:3D GEOMETRY USED IN THE WORK OF GEORGIOU E PAPALEXANDRIS (2017).

The present simulation was performed in the ANSYS FLUENT® software, where the flow velocity inlet of the parallel flow is 1 m/s, the outlet pressure of both flows is 0 Pa and kinematic viscosity of the fluid is 0.000111 m² s for all wall functions simulated. The origin point of the simulation is located at the vertex of the jet flow inlet. For the moment ratio $M_R = 2$, the inlet velocity of the jet flow is equal to the inlet velocity of the parallel flow of 1 m/s. The number of Reynolds Re used in this work is 15.000 at the entrance of the parallel flow, the same used in the works of [1]. The domain of the simulation is shown in Fig. 5, where A is the parallel flow inlet, B is the channel walls, C is the jet flow inlet and D is the mixed flow outlet.

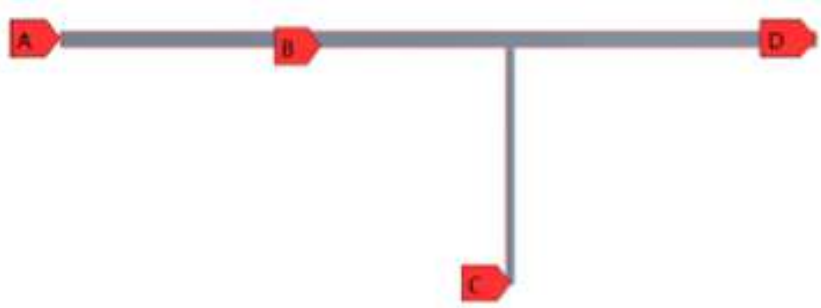

FIGURE 5:DOMAIN OF THE PRESENT SIMULATION

All the simulated cases in the present work use the finite volume method to discretize the governing equations. The interpolation scheme used is QUICK [13] and the SIMPLE scheme was used in pressure and velocity coupling. For the resolution of the system of linear equations the Multigrid technique was used [14]. For the simulation 500.000 iterations were used and was considered converged when all the residues were smaller than 10^{-12}.

The results for 5 different meshes with 200.000, 400.000 and 700.000, 1.000.000 and 1.503.400 elements in each mesh was analysed. Generally, all meshes used in the simulation for all k-ε model can be illustrated according to Fig. 6a and in more detail in Fig. 6b. The meshes present in this study were refined in the regions near the walls and at the vertices of the inlet channel of the jet stream. The selection of such regions was based on the studies of [1],[15], [16], [17] which indicate the appearance of recirculation bubbles at the edges of the jet flow inlet.

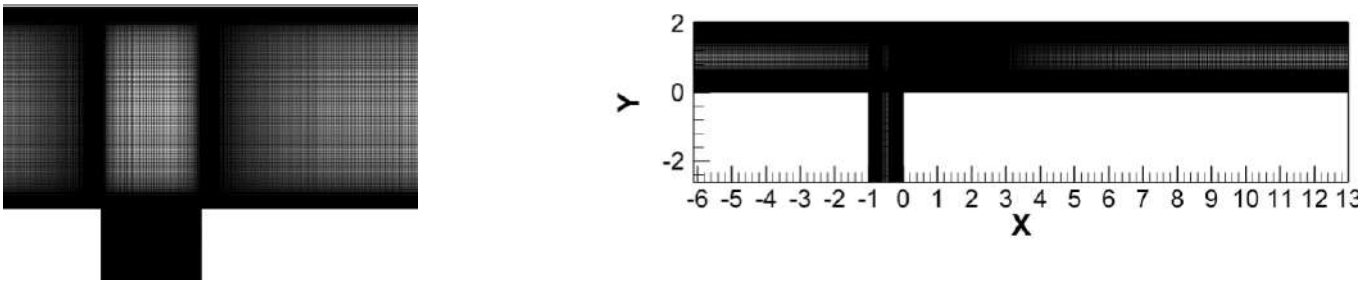

(a) (b)

FIGURE 6: STANDARD MESH USED IN THE SIMULATION OF THE PRESENT WORK.

To analyse the convergence of the result a mesh with 1.503.400 elements were used due to the higher computational precision of the mesh.

IV. RESULTS

The results obtained in the simulations of the present work were calculated through the turbulence model k-ε for different wall functions. The results were compared with the LES simulation performed by [1] using their own software. In this section, important parameters are discussed such as recirculation bubble size, u-velocity vector profile, velocity u^+ profiles, turbulent kinetic energy production and streamlines.

4.1 Streamlines and the recirculation bubble size

The study of the average velocity stream lines is of most importance, since through its analysis, the behaviour of the flows can be identified, for example: mixing zones and layers of separation of the flows. Figure 7 shows the streamlines found in the work of [1] (a) and the those found in k-ε models: Standard Wall Function (b), Enhanced Wall Treatment (c) and Menter-Lechner Wall Treatment (d).Some important characteristics of the flow are described in Fig. 7. According to [1], for the parallel flow, the velocity profile remains unchanged before the jet flow inlet region. However, as the parallel flow approaches the jet flow inlet region, the flow lines of the parallel flow tilt in a vertical direction, since the parallel flow cannot pass through the jet stream. In this way, the parallel flow bypasses the jet stream as an obstacle. The same occurs or the jet flow, as it cannot penetrate the parallel flow it tilts until it is becomes parallel to the channel.

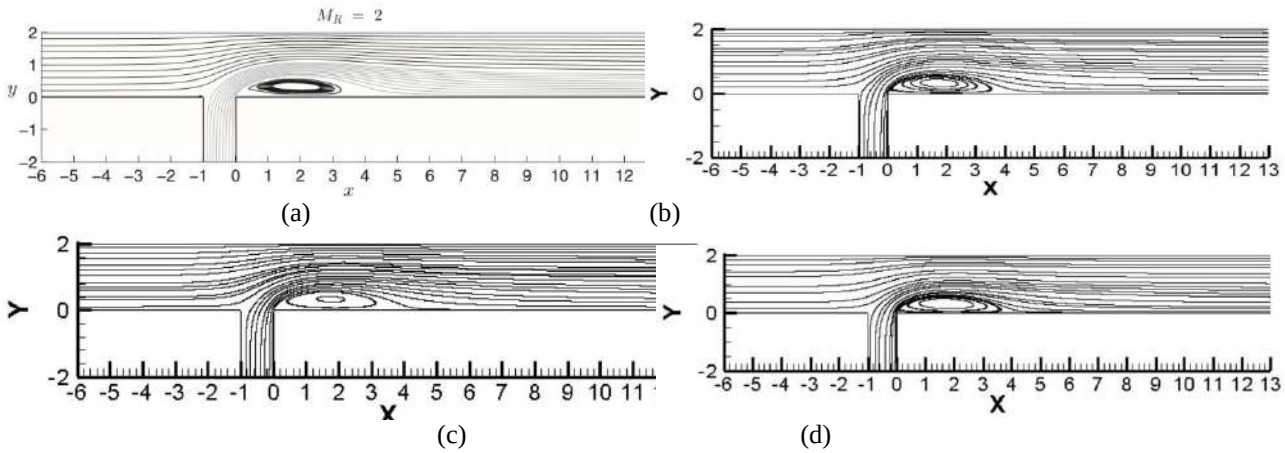

FIGURE 7: STREAMLINES FROM THE WORK OF GEORGIOU E PAPALEXANDRIS (a) AND FROM THE PRESENT WORK (b,c,d).

The slope of the jet stream generates the recirculation bubble downstream of the inlet of the jet stream. The shear layer between the flows can be easily visualized in Fig. 7 (b,c,d). According to Fig. 7 (a), it is possible to ascertain the size of the recirculation bubble in the work of [1] in which the bubble extends to the value of approximately x = 5.

4.2 Contour of the average magnitude velocity

Figure8 shows the contour of the field of magnitude of velocity between the work of [1] and the present simulation.

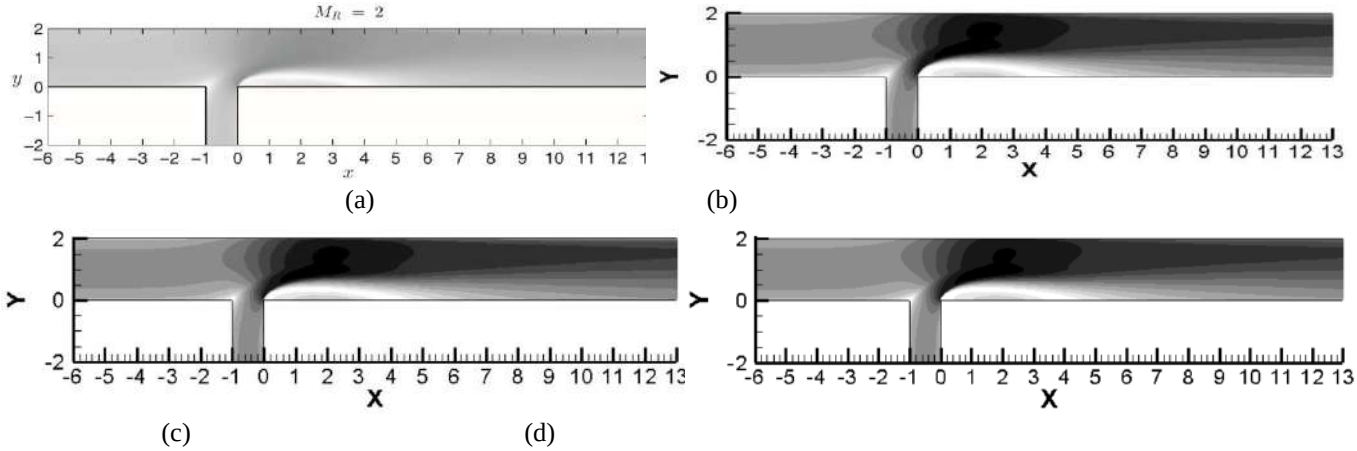

FIGURE 8: CONTOUR OF THE AVERAGE MAGNITUDE VELOCITY FOUND IN THE WORK OF [1] (a) AND K-E MODEL STANDARD WALL FUNCTION (b), K-E MODEL ENHANCED WALL TREATMENT (c), K-E MODEL MENTER-LECHNER WALL TREATMENT (d).

For both results, a second recirculation bubble was found at the vertex upstream of the inlet of the jet stream. The two structures were also found in the results of [18] and [19] and are typical of jets in unconfined parallel flows. In the same work of [20] flow characteristics were found for T-channel. Analysing Fig. 8, the equality in the results can be observed. It is also possible to identify a progressive increase in the magnitude of the velocity from the inlet of the parallel flow once the particles of the parallel flow accelerate while circumventing the jet flow in all results. Such acceleration occurs due to the reduction of the cross-sectional area of the parallel flow due to the Venturi effect. In addition, the jet flow also has a strong acceleration bypassing the parallel flow since the jet flow is limited in the upper part by the parallel flow and in the lower part by the recirculation bubble, reducing the cross-sectional area of the jet stream and increasing its acceleration also through the Venturi effect. It is also possible to notice the occurrence of a second recirculation bubble upstream of the entrance of the jet stream in the channel for all situations analysed. The appearance of the second recirculation bubble can be attributed to the adverse pressure gradient present at the recirculation bubble area, generating the second separation region present in Fig. 8.

4.3 U velocity profile

The profiles of the medium velocity component u (mean velocity U) are described in Fig. 9. The graphics show the comparison between the velocity profile graphs found in the present work, using the stationary k-ε models: Standard Wall Function (b), Enhanced Wall Treatment (c) and Menter-Lechner Wall Treatment (d), and the work of [1], and the transient model LES.

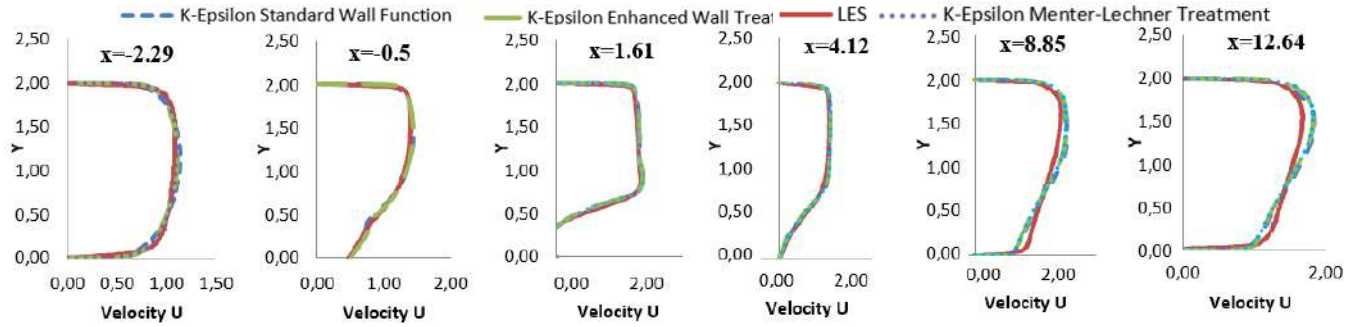

FIGURE 9: COMPARISON OF THE AVERAGE VELOCITY U BETWEEN THE PRESENT WORK AND THE WORK OF [1] FOR DIFFERENT VALUES OF X.

Figure 9 clearly demonstrates the Venturi effect and the increase of velocity of both the parallel and jet streams. For x = -2.29, the region of the parallel flow inlet shows a symmetrical velocity profile, typical of a fully developed flow. When advancing to the inlet region of the jet stream, the symmetry of the velocity profile is lost. At the beginning of the bubble, for x = 1.61, the mean velocity profile is typical of medium velocity profiles containing recirculation bubble. After the recirculation region, the restablishing of the channel flow occurs, however for all the k-ε models, such restablishing occurs more slowly.

4.4 Turbulent Kinetic Energy K Production Profile

The profiles of the turbulent kinetic energy production K are described in Fig. 10. The comparison between the graphs of K production profiles found in the present work, using the stationary k-ε models: Standard Wall Function, Enhanced Wall Treatment and Menter-Lechner Wall Treatment, and the work of [1], and the transient model LES.

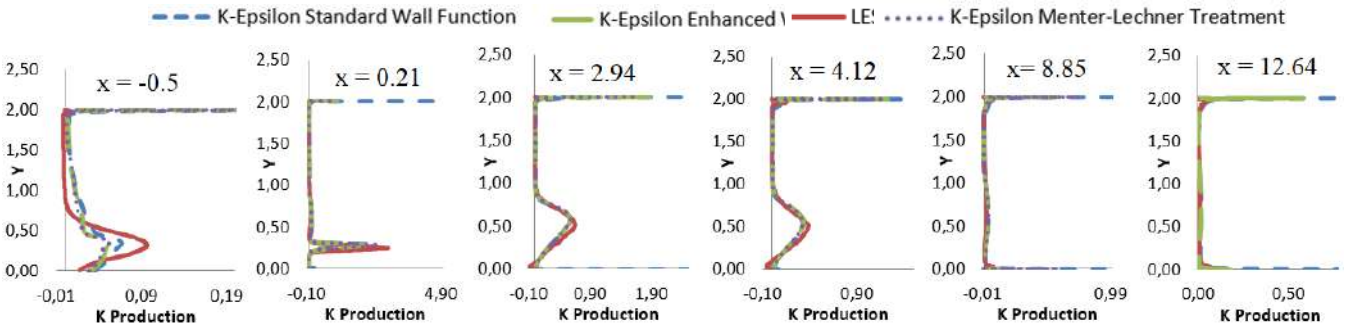

FIGURE 10: COMPARISON OF THE PRODUCTION K BETWEEN THE PRESENT WORK AND THE WORK OF [1] FOR DIFFERENT VALUES OF X.

In addition, the negative K production values found by [1] were not found in the current simulation. However, the higher production values of K coincided with the location of the shear layer between the flows, which leads to conclusion that the production of turbulent kinetic energy comes precisely from the region of the shear layer between the flows. This fact was also found in the study by [1].

4.5 U+ Velocity Profile

Figure 11 shows the comparison between the profiles of u+ at the bottom wall from the present work and the data from the literature at three different streamwise regions: one region upstream the jet and close to the inlet of the crossflow at x = -4,3 and one region downstream the large separation bubble at x = 8,66 and another region further distant from the large separation bubble x = 12,64.According to the results shown in Fig.11 (a), the u^+velocity profile from the k-ε models at x = -

4,3 have a good agreement with the theoretical law of the wall. This is to be expected because at this location, the crossflow remains unaffected by the incoming jet. Additionally, this agreement with the law of the wall indicates the good quality of the results presented by all k-ε models with the exception of the k-ε model standard wall function since its result does not present good agreement with the theoretical law of the wall. The results from all k-ε models at the nearest region downstream the separation bubble in Fig.11 (b), at x = 8.66, deviate considerably from the law of the wall. Specifically, the profiles from the literature and from the k-ε model show an inflection point in the log-law region. This profile behaviour is typical of wall-bounded flows with large separation zones and its occurrence is due to the adverse pressure gradients that are developed downstream those zones as described by [1].There is also can be seen, in Fig.11 (c) that the deviation from the law of the wall exists at the regionx = 12.64, however, this deviation is smaller than at x = 8.66. Such behaviour confirms that further downstream the T-junction and the jet flow inlet, a channel flow will be re-established.

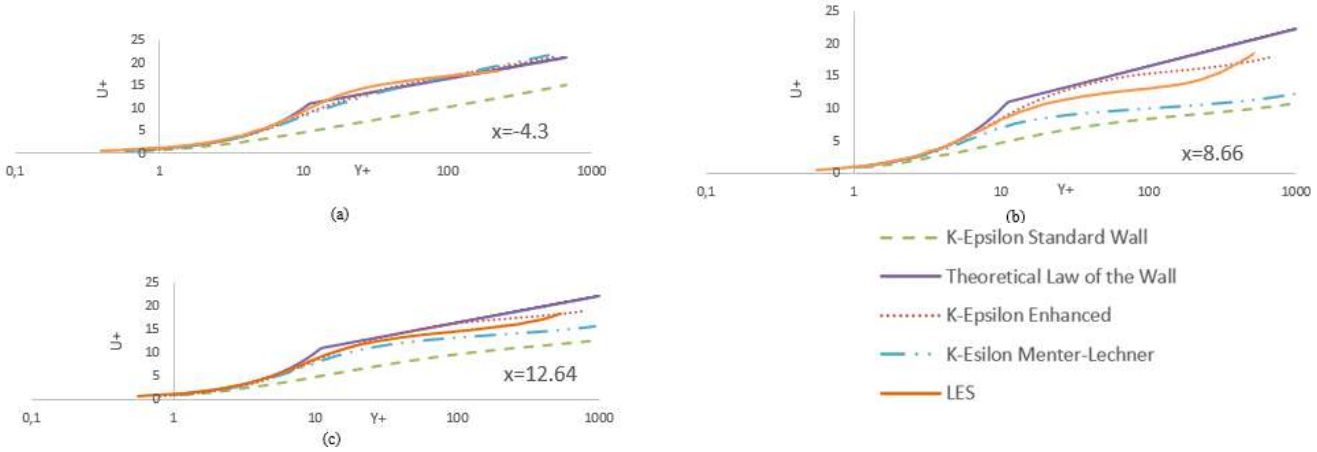

FIGURE 11: COMPARISON U+PROFILES AT THE CHANNEL BOTTOM WALL FROM THE PRESENT WORK AND THE WORK [1] FOR DIFFERENT X VALUES.

Comparing the profiles from each of k-ε turbulence model, the k-ε model Enhanced wall treatment showed best results for all regions, as the k-ε model Menter-Lechner wall treatment displayed larger deviation at x = 8.66. The k-ε model standard wall function diverged significantly from the results obtained by both the other models analysed and by the theoretical curves of the wall law in the turbulent region.

Figure12 shows profiles of u^+at the upper wall and at three different streamwise regions: one region upstream the jet and close to the inlet of the cross flow at x = -4.3 and one region near downstream the jet flow inlet at x = 0.21 and another region further distant from the large separation bubble x = 12.64.

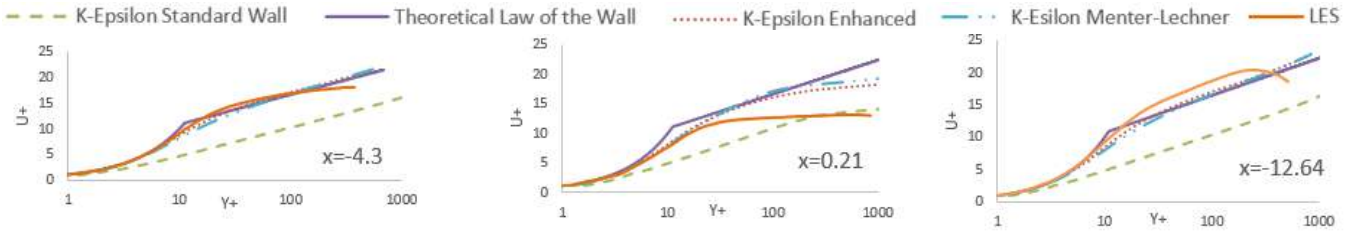

(a) (b) (c)

FIGURE 12: COMPARISON U+ PROFILES AT CHANNEL BOTTOM WALL FROM THE PRESENT WORK AND THE WORK OF [1] FOR DIFFERENT X VALUES.

As in the case of the bottom wall previously described, in Fig.12 (a) at x = -4.30, the top-wall profile follows the theoretical law of the wall. However, at the second region in Fig.12 (b), x =0.21, the deviation from the universal law of the wall is larger. However, u+ maintains a small logarithmic growth. This behaviour can be seen in all models here described, thus in agreement with literature. Such behaviour is attributed to the strong favourable pressure gradient that results from the Venturi effect, that is, the decrease in the cross-sectional area and the ensuing acceleration of the crossflow. Also, as before, in Fig.12 (c) the deviation from the law of the wall that exists at the region x = 12.64 is smaller than at x = 8.66 confirming that further downstream the T-junction and the jet flow inlet, a channel flow will be re-established. Comparing the profiles from each of k-ε turbulence model, the results remain almost the same as for the bottom wall, the k-ε model Enhanced and Menter-

Lechner wall treatment showed best results for all regions. The k-ε model standard wall function diverged significantly from the results obtained by both the other models analysed and by the theoretical curves of the wall law. The results from both walls corroborate to the fact that the turbulence model of two k-ε differential equations with standard wall function does not show good performance in cases with adverse pressure gradient and flow separation, especially in those regions near the wall are regions of great interest.

V. CONCLUSION

In the present work, the turbulence model based on the Average Reynolds Equations (RANS) was used: k-ε model with different wall treatments such as standard wall function, Enhanced Wall Treatment and Menter-Lechner Wall Treatment to analyse the turbulent flow in a T-junction channel having two flows, a flow parallel to the channel and another jet flow, perpendicular to the channel. The results were compared with the studies realised by [1], using the Large Scale Simulation (LES) model. The present work found two recirculation bubbles, one primary bubble downstream of the inlet of the jet stream and another smaller secondary bubble upstream of the jet stream. The same results were found by [1].

The results from all turbulence models are mostly in agreement with the data found by [1], however the k-ε model standard wall functions presented larger deviations for the K production, u^+. The production of turbulent kinetic energy in the wall region was higher in comparison to the result found in the LES simulation for all models. Additionally, the production of turbulent negative kinetic energy was not perceptible, as found by [1]. The k-ε model Enhanced Wall Treatment presented the best results, in accordance with the literature. All models presented smaller length of the recirculation bubble in comparison with literature.

The results presented from the models here analysed indicate that the turbulence model of two k-ε differential equations with standard wall function does not show good performance in cases with adverse pressure gradient and flow separation, especially in those regions near the wall are regions of great interest. Additionally, better results near the wall region were found by the use of k-ε model Enhanced Wall Treatment and Menter-Lechner Wall Treatment.

REFERENCES

[1] M. Georgiou and M. V. Papalexandris . "Numerical study of turbulent flow in a rectangular T-junction". Physics of Fluids APE. (2017).J.ClerkMaxwell, A Treatiseon Electricity and Magnetism,3rded.,vol.2.Oxford:Clarendon,1892,pp.68–73.

[2] Rezende, A.L.T., 2009. Análise numérica da bolha de separação do escoamento turbulento sobre placa plana fina inclinada. Departamento de Engenharia Mecânica, Pontifícia Universidade Católica, Rio de Janeiro.

[3] Jones, W. P.; Launder, B. E. Prediction of laminarization with a two-equation model of turbulence. International Journal of Heat and Mass Transfer. v. 5, p. 31-34, 1972.R.Nicole, "Title of paper with only first word capitalized," J.Name Stand.Abbrev.,inpress.

[4] Launder, B. E.; Sharma, B. I. Application of the energy-dissipation model of turbulence to the calculation of flow near a spinning disk. Letters in Heat and Mass Transfer, v. 1, p. 131-138, 1974

[5] Wilcox, D.C. Reassessment of the Scale-Determining Equation for Advanced Scale Models. AIAA Journal 26(11): 1299-1310, 1988.

[6] Wilcox, D. C. Comparison of two-equation turbulence models for boundary layers with gradient. AIAA journal, v. 31, n. 8, p. 1414–1421, 1993.

[7] Launder, B. E.; Spalding, D. B. The numerical computation of turbulent flows. Computer methods in applied mechanics and engineering, Elsevier, v. 3, n. 2, p. 269–289, 1974.

[8] M. Wolfstein. The Velocity and Temperature Distribution of One-Dimensional Flow with Turbulence Augmentation and Pressure Gradient. Int. J. Heat Mass Transfer, 12:301-318, 1969.

[9] H. C. Chen and V. C. Patel. Near-Wall Turbulence Models for Complex Flows Including Separation. AIAA Journal, 26(6):641-648, 1988.

[10] T. Jongen. Simulation and Modeling of Turbulent Incompressible Flows. PhD thesis, EPF Lausanne, Lausanne, Switzerland, 1992.

[11] B. Kader. Temperature and Concentration Profiles in Fully Turbulent Boundary Layers. Int. J. Heat Mass Transfer, 24(9):1541-1544, 1981.

[12] Inc. ANSYS, "ANSYS Fluent Theory Guide - Release 17.2," 2016. [Online]. Available: https://support.ansys.com/AnsysCustomerPortal/en_us/Knowledge+Resources/Online+Documentation/Previous+Releases/17.2/Fluid+Dynamics/ANSYS+Fluent/Fluent+Theory+Guide?doc_link=/prod_docu/17.2/html/flu_th/flu_th.html..

[13] Leonard, B. P, 1979. A Stable and Accurate Convective Modelling Procedure Based on Quadratic Upstream Interpolation.Computer Methods in Applied Mechanics and Engineering, p. 59-98.

[14] Hutchinson B. R., Raithby G. D, 1986. A Multigrid Method Based on the Additive Correction Strategy. Numerical Heat Transfer, p. 511-537.

[15] Hirota M., Asano H., Nakayama H., Asano T., and Hirayama S., Three Dimensional Structure of Turbulent Flow in Mixing T-junction, JSME Int. J., Ser. B 49, 1070–1077 (2006).

[16] M. Hirota, E. Mohri, H. Asano, and H. Goto, "Experimental study on turbulent mixing process in cross-flow type T-junction," Int. J. Heat Fluid Flow 31, 776–784 (2010).

[17] A. Kuczaj, E. Komen, and M. Loginov, "Large-eddy simulation study of turbulent mixing in a T-junction," Nucl. Eng. Des. 240, 2116 2122 (2010).

[18] S. Muppidi and K. Mahesh, "Study of trajectories of jets in crossflow using direct numerical simulations," J. Fluid Mech. 530, 81–100 (2005).

[19] R. Kelso, T. Lim, and A. Perry, "An experimental study of round jets in cross-flow," J. Fluid Mech. 306, 111–144 (1996).

[20] N. Fukushima, K. Fukagata, N. Kasagi, H. Noguchi, and K. Tanimoto, "Numerical and experimental study on turbulent thermal mixing in aT-junction flow," in The 6th ASME-JSME Thermal Engineering JointConference (American Society of Mechanical Engineers, 2003), pp. 16–20.

Design of RF Transmitter with high speed for Magnetic Resonance Imaging (MRI) using 8-Core DDS System of FPGA

Dontabhaktuni Jayakumar[1], B Pulla Rao[2], B Satyanarayana[3]

Department of ECE, Asst Prof, Holy Mary Institute of Technology and Science, Bogaram, Keesara, Secundrabad, Telangana.

Abstract— *An overall goal of the research is to investigate a new approach to the MRI RF Transmitter. Design a high-speed MRI RF transmitter. The goal is to explore the potential of a built-in DDS core of an FPGA chip to generate a dual-channel output at a 1 GHz sampling frequency of each. This output will be processed by a dual-input DAC chip for a total of 2 GHz sampling rate. The entire system should be able to generate the output signal ranging from 100 kHz to 750MHz. To accomplish this goal, it is necessary to study and to investigate the structures of these features to see how they could be utilized as a main core in a pulse generator*

According to the datasheet provided by Xilinx, a DDS core has a single sine or/ and cosine output signal. The DDS core can operate at a maximum clock of 250 MHz. A 250 MHz clock speed is insufficient to generate outputs at 1 GHz sampling frequency. Consequently, the proposed custom DDS system is expected to quadruple the clock speed of the system by implementing multiple DDS core modules within the system.

Keywords— Direct Digital Synthesis.

I. INTRODUCTION

1.1 Introduction of Magnetic Resonance Imaging

MRI spectroscopy is a technique used to study the physical, chemical and biological properties of materials by probing the nuclear dipole moments in the material. It was found and measured using molecular beams by Isidor Rabi in 1938. He received the Noble Prize in Physics in 1944 for his work. Two years later, Felix Bloch and Edward Mills Purcell expanded the technique to liquids and solids. They used it as an analytical tool in chemistry and physics in 1946.

An overall goal of the research is to investigate a new approach to the MRI RF Transmitter. The detail research objectives are as below:

Design a high-speed MRI RF transmitter: The goal is to explore the potential of a built-in DDS core of an FPGA chip to generate a dual-channel output at a 1 GHz sampling frequency of each. This output will be processed by a dual-input DAC chip for a total of 2 GHz sampling rate. The entire system should be able to generate the output signal ranging from 100 kHz to 750MHz. To accomplish this goal, it is necessary to study and to investigate the structures of these features to see how they could be utilized as a main core in a pulse generator. However, due to the limitations of FPGA to go beyond an allowable clock speed in DDS, the challenges of this problem lead to four objectives as below:

a) Design a new topology for an MRI RF transmitter by using Matlab-Simulink. The Simulink is used to design the structures of a high-speed RF transmitter. The structures are verified through the Matlab-Simulink simulation.

b) Simulate the designs in 1.3(a) above in the register-transfer level (RTL-level) simulation by using the Xilinx Verilog compiler. The simulations in Matlab do not consider the timing constraints within the DDS system. Matlab simulations are used to verify the functionality of the design and to analyze the flow from input to output. Therefore, it is necessary to simulate the design in RTL-level to ensure the behavioral structures meet the timing constraints.

c) Design a new methodology to run a dual-output DDS module at 1 GHz each. The 1GHz frequency is beyond the clock limitation of an internal DDS core in an FPGA chip.

According to the datasheet provided by Xilinx, a DDS core has a single sine or/ and cosine output signal. The DDS core can operate at a maximum clock of 250 MHz. A 250 MHz clock speed is insufficient to generate outputs at 1 GHz sampling frequency. Consequently, the proposed custom DDS system is expected to quadruple the clock speed of the system by implementing multiple DDS core modules within the system.

II. MATERIAL AND METHODS

2.1 Magnetic Resonance Imaging System

An MRI spectrometer requires a magnet, a coil, and some electronic systems such as a transceiver and a computer. These instruments provide the stimulus and to be subsequent detect the FID signal. First diagram figure 1 refers to the enlarged view of MRI system and figure2 refers to the block diagram of MRI Transmitter system.

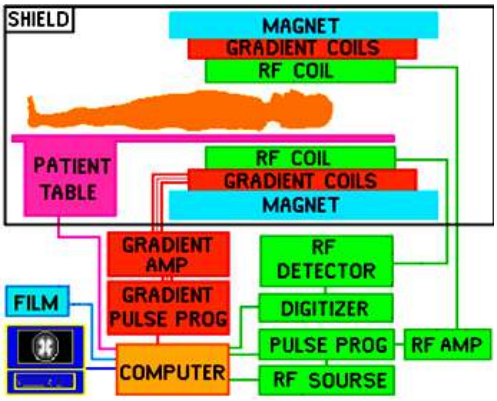

FIGURE 1: ENLARGED VIEW OF MRI SYSTEM

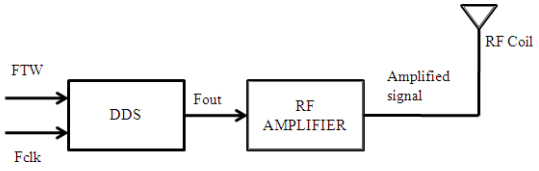

FIGURE2: BLOCK DIAGRAM OF MRI TRANSMITTER SYSTEM

Typically, the most expensive and difficult part of the system is the magnet system. The cost of the system is proportional to the magnetic strength. The better the sensitivity and spectral resolution of the system, and hence more expensive is the magnet.

The first block in Figure 1 refers to the DDS (Direct Digital Synthesis) block, which is used to generate the required output frequency upon providing the corresponding FTW (Frequency Tuning Word) and clock frequency. Thus the generated output frequency is fed to an RF Amplifier in order to amplify the signal to the desired level. Later the amplified signal is transmitted through RF Coil for further processing.

2.2 Direct Digital Synthesis

DDS usually refers to look-up table (LUT) based sinusoid generators. A DDS is a technique to generate frequency- and phase-tunable output signals.

It uses digital data processing blocks with a fixed-frequency precision clock to generate a sinusoidal signal. In Figure 2 a simple DDS can be created with a precision reference clock, an address counter, a Programmable Read-Only Memory (PROM) LUT and a DAC chip. In this basic system, PROM stores the amplitudes of a complete sine-wave. The address counter is used to generate memory addresses to access the PROM. A memory address is an identifier for a memory location in the PROM. The memory address will retrieve the digital amplitude from the PROM to the DAC chip. The advantage of using the DDS based system is that the simplistic architecture of the DDS system is less susceptible to the tuning flexibility. The reason is the output frequency can only be changed by modifying the system clock speed or by re-programming the step size in the PROM.

2.3 Phase Accumulator

The main part of the DDS system is the phase accumulator whose contents are updated once on each clock cycle. Each time the phase accumulator is triggered, the tuning word or phase increment, M is added to the contents of the phase accumulator. Let us assume that the initial content of the phase accumulator is 00…00 and M=00… 01. The phase accumulator is updated by 00…01 on each clock cycle. A phase accumulator replaces the address counter in Figure 2 to introduce a function known as a ‘phase wheel’.

Hence, a sine LUT is used to convert the output phases to sine-wave digital amplitudes. A DAC chip is then used to convert these amplitudes to an analog signal. However, the Nyquist sampling theory dictates a complete sine-wave must have at least two samples per cycle to construct the output waveform. Thus, the maximum frequency of an output sine wave is half of the DDS system clock.

In summary, the frequency of a sine-wave signal can be expressed by the equation below:

$$f_{out} = \frac{M}{2^N} f_{system} \quad (2.0)$$

$$M = \frac{f_{out} \times 2^N}{f_{system}} \quad (2.1)$$

f_{out} = the frequency of an output sine wave signal

M = frequency tuning word

N = N-bit of a phase accumulator

f_{system} = system frequency

'M' is also known as a digital number for phase hopping in an accumulation. 'N' is the total bits of a phase accumulator, so 2^N is the amount of steps available in the accumulator.

The division of 'f_{system}' by 2^N represents the frequency resolution of the system.

2.4 Phase-to-Amplitude Converter

In this thesis, the phase-to-amplitude converter or LUT is configured as a sine LUT. If B represents the width of a truncated phase, a sine LUT can be simply a read-only memory containing 2^B samples that create the sample-domain waveform from the truncated phase received from the phase accumulator. In other words, it converts phases from a phase accumulator to amplitudes. These digital phases are also the memory addresses used to retrieve the corresponded amplitudes from the sine LUT.

A PROM can be used to implement a sine LUT. A PROM based LUT is easily implemented due to the simplicity of the PROM circuit. A LUT contains one complete cycle of the waveform to be generated.

The LUT translates the truncated phases into the sample amplitudes which are then converted to an analog signal by DAC.

If a high precision signal is required, the LUT needs a very large capacity as more bits are required to store the amplitudes. This increases the hardware cost and the implementation is limited by the capacity of the PROM. Practically, only the 'high bits' of an accumulated phase are used as a memory address to access the LUT. Generally, these high bits are known as the truncated phase. The size of a LUT is 2^B words, therefore B <N; N is the width of accumulated phases.

2.5 Taylor Series Corrected DDS

In the Taylor series corrected DDS; the previously discarded fractional bits have been used to calculate corrections to the phases. The corrections are added to the look-up table values to produce outputs with very high spurious free dynamic range (SFDR). This noise shaping technique can maintain the LUT to a reasonable size. The Taylor series corrected approximation is the expansion of a function of:

$$f(x) = f(a) + f'(a)\frac{(x-a)}{1!} + f''(a)\frac{(x-a)^2}{2!} + \ \ldots \quad (2.1)$$

Hence, the Taylor expansion of $\sin\left(\frac{\pi}{2}\ q\right)$ (quarter-wave storage in LUT) is as below:

$$\sin\left(\frac{\pi}{2}\ q\right) = \sin\left(\frac{\pi}{2}r\right) + k_1(q-r)\cos\left(\frac{\pi}{2}r\right) - \frac{k_2\,(q-r)^2 \sin\left(\frac{\pi}{2}r\right)}{2} + \ldots \quad (2.2)$$

The total q-bit phase is divided into the upper phase 'r' and the lower phase 'q-r'. After the phase truncation, only the upper phase 'r' is used for the phase information, so the Taylor series is performed around 'r'.

The phase values have angular units so the constant k_n (n=1, 2, 3…) is used to adjust the units of each series term. k_n includes a multiple of $\pi/2$ to compensate for the phase units.

It is also used to make sure the expression is always positive. From equation, k_1 is $\pi/2$=1.57 and k_2 is $-(\pi/2)^2$ = -2.47. The Taylor series approximation takes up to three terms. In fact, additional terms can be employed but the contribution to the accuracy is very small. This architecture needs two read-only memory (ROM) blocks to store $\sin(\pi r/2)$ and $\cos(\pi r/2)$. The unit conversion factor k_n is included in the values stored in the sine and cosine ROMs

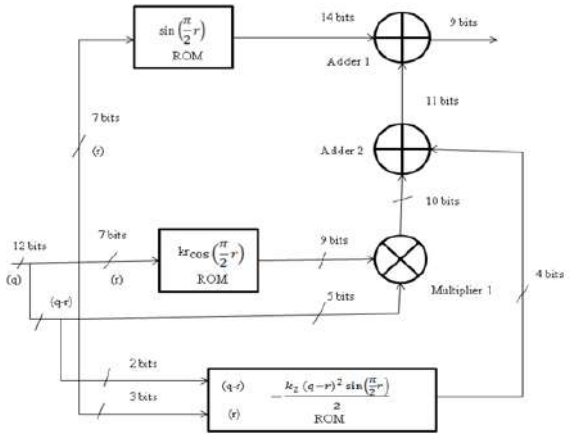

FIGURE 3A: TAYLOR'S SERIES APPROXIMATION FOR QUARTER SINE WAVE.

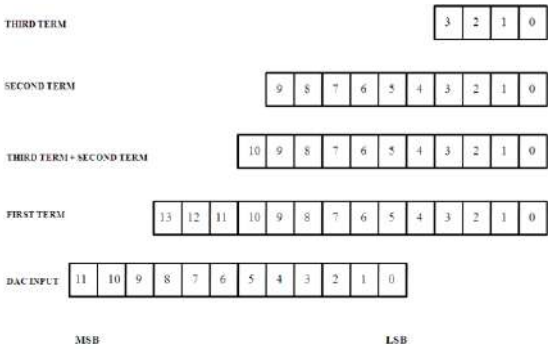

FIGURE 3B: RELATIVE BIT POSITION OF DATA WORD IMPLEMENTED

For example, an input phase (q) has 12 bits as shown in Figure 3. The upper 7 bits of 'q' are used as the upper phase increment 'r'. This 'r' is transferred to both sine ROM and cosine ROM at the same time. The upper 7 bits are the address signals and hence determine the number of entries in the ROMs. More bits in the upper phase address result in a larger LUT with decreased speed and greater cost.

The sin (πr/2) ROM is the first term of the Taylor series expansion. The output from the sine ROM will then sum the other terms from the expansion to re-construct the final phase (Adder 1).

The output of the cos (πr/2) is configured to incorporate the predetermined unit conversion value k_1. The cosine ROM is less significant than the amplitude term. Thus, the output can be at lower accuracy and so 9-bit output number is used. The lower 5 bits (q-r) are used to compute the other two terms used in the Taylor series expansion. The 'q-r' is multiplied with the output from cosine ROM to generate the second term (Multiplier 1). The second term has 10-bit output number.

The MSB of output from the 'multiplier 1' has a bit alignment with the DAC input Least Significant bit (LSB). Because of the alignment, the output number ranges from 1 LSB to 1/1024 LSB of the final 10-bit DAC input used. Not all the bits after the 'multiplier 1'are needed to maintain the accuracy of the system.

Therefore, the system truncates the multiplication product to 10 bits. In any case, truncation to 10 bits after 'multiplier 1'was used in the example in Figure 3. Any bit widths can be used as desired as long as the principles of the design are met. The third expansion term is computed in a ROM by combining the derivative of sin (πr/2) and $(q-r)^2$. This is done by selecting the upper 2 bits of 'q-r' and the lower 3 bits of 'r' as a portion of the address for the ROM. This is possible because the last expansion term only contributes roughly 1/4 LSB to the DAC input as shown in Figure 3B. In Figure 3, only the 'r' is needed for this degree of accuracy. Finally, the third term ROM output will combine with the 'multiplier 1' output in 'Adder 2'. Subsequently, the result will combine with the first term ROM output in the 'Adder1'.

III. SIMULATION RESULTS

3.1 Matlab-Simulink Simulation Results

15 MHz is randomly chosen as the frequency to test a single DDS core and few random frequency signals are used to test the 8 core DDS System. Finally a 64MHz frequency signal has been generated using 8 Core DDS System.

3.2 Simulation Results of a Single DDS Core

The purpose of running the simulation on a standard DDS core is to observe the relationship between the phases and the amplitudes generated by the core. The explicit sample period of the phase accumulator and LUT is set to 8 in order to standardize the sampling period between a single DDS core and an 8-core DDS module. Consequently, the outputs of both simulations can be compared (both outputs have the same sampling period). The simulation is based on the Simulink design in Figure 4.1. The parameters of the simulation are:

F_{out}	:	15000000 Hz
Phase Accumulator System Clock, f_{system}	:	250 MHz

Explicit Sample Period of Phase Accumulator core : 1

Simulation Period : 500 units

The simulation period is set to 500 units of time so that the design system can generate a couple of complete of sine-waves within this period. When the simulation is executed, 15000000Hz is converted to the frequency tuning word in the phase register block. The step-size of the output equals the phase increment of the output frequency. Based on equation (2.0), the tuning word is 2013265. Hence, the step size is 2013265. The frequency resolution is fixed at 7.45Hz for a Single DDS core with 250MHz system clock and 25-bit phase accumulator. The simulation results of Single DDS stage by using MATLAB are shown in Figure 4A and Figure 4B.

Tuning word=15000000 x 2^{25}/250MHz =2013265

Step size=2013265 / 1=2013265

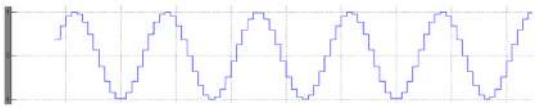

FIGURE 4A: 15MHZ SINE WAVE (RF) SIGNAL (MATLAB)

FIGURE 4B: PHASE OF 15MHZ SINE WAVE (RF) SIGNAL (MATLAB)

The System Generator tool converts the design of Xilinx Blockset based Single DDS into Verilog HDL. In the design of Xilinx Blockset based Single DDS the inputs are 'clock (250MHz)', 'rst' and phase_in' which is 25- bit binary data. The output 'sine' is a 14-bit binary data and 'phase' is 25 bit binary data. The input 'phase_in' is the phase accumulator input (holds the FTW) .The outputs 'sine' is the digital amplitude sine wave signal and 'phase' is the phase of the signal. The simulation results of Single DDS stage by using Xilinx ISE tool is shown in Figure 5.

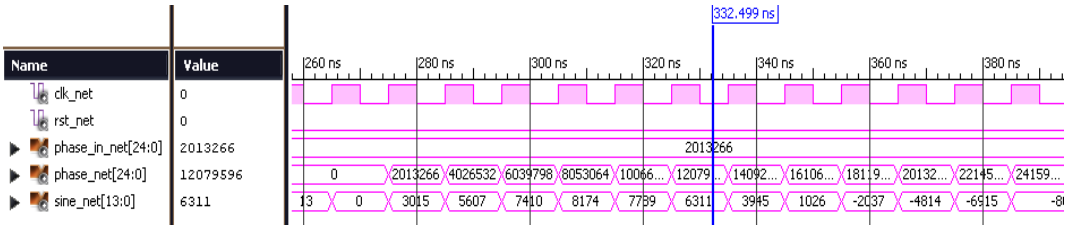

FIGURE 5: SIMULATION OF 15MHZ SINE WAVE (RF) SIGNAL (XILINX)

With reference to the Figure Simulation of 15MHz sine wave (RF) signal (Xilinx , the phase_in (FTW) for 15MHz signal is calculated based on equation (2.0) is given as input to the phase accumulator block in the DDS core. Upon pos-edge 'clk' and active low 'rst', the phase accumulator increments its value to FTW. Further these values are given as input to Sine LUT in DDS core, which performs phase to amplitude conversion.

The normalised tuning word on the phase register block is measured as 0.25 (Display_tw). This 0.25 is divided by eight (denominator) to produce 0.03125 (normalised step size) via a divider block. 0.03125 is then multiplied by 2x D2, 3x D3, 4x D4, 5x D5, 6x D6, 7x D7 and 8x D8 to produce 2^{nd} to 8^{th} phase offsets. Each phase offset is combined with an accumulated phase from the 'phase_out' through the respective Adder1 until Adder8. This methodology generated eight continuous samples 'Out1' to 'Out8' over a unit time. The results are shown in Table1.

TABLE 1

COMPARISON BETWEEN SIMULINK AND MATHEMATICAL CALCULATION RESULTS

Display	Simulink	Mathematical Calculation (Integer)
Display_tw	0.25	0.25 x 2^{25} ≈ 8589934
Display_Offset1	0.03125	0.03125 x 2^{25} ≈ 1073741
Display_Offset2	0.0625	0.0625 x 2^{25} ≈ 2147482
Display_Offset3	0.09375	0.09375 x 2^{25} ≈ 3221223
Display_Offset4	0.125	0.125 x 2^{25} ≈ 4294964
Display_Offset5	0.15625	0.15625 x 2^{25} ≈ 5368705
Display_Offset6	0.1875	0.1875 x 2^{25} ≈ 6442446
Display_Offset7	0.21875	0.21875 x 2^{25} ≈ 7516187
Display_Offset8	0.25	0.25 x 2^{25} ≈ 8589934

The results from the Simulink and mathematical calculations are identical. The normalised outputs can be restored to their original values by multiplying each normalised result with 2^{25} (inverse of gain factor).

The System Generator tool converts the design of Xilinx Blockset based Phase Accumulator block into Verilog HDL. In the design of Xilinx Blockset based Phase Accumulator block, the inputs are 'clock(250MHz)','rst' and 'tuningword' which is 25- bit binary data and 8-sets of phase offsets as 'offset1,offset2....offset8'. The outputs 'phaseout1, phaseout2...phaseout8' are 25 bit binary data. The input 'tuning word' is the phase accumulator input (holds the FTW) and 'offset1, offset2...offset8' holds the phase offset. The outputs are 'phaseout1, phaseout2...phaseout8' holds the 25 bit sample output phases.

The simulation results of Phase Accumulator block by using Xilinx ISE tool is shown in Figure6

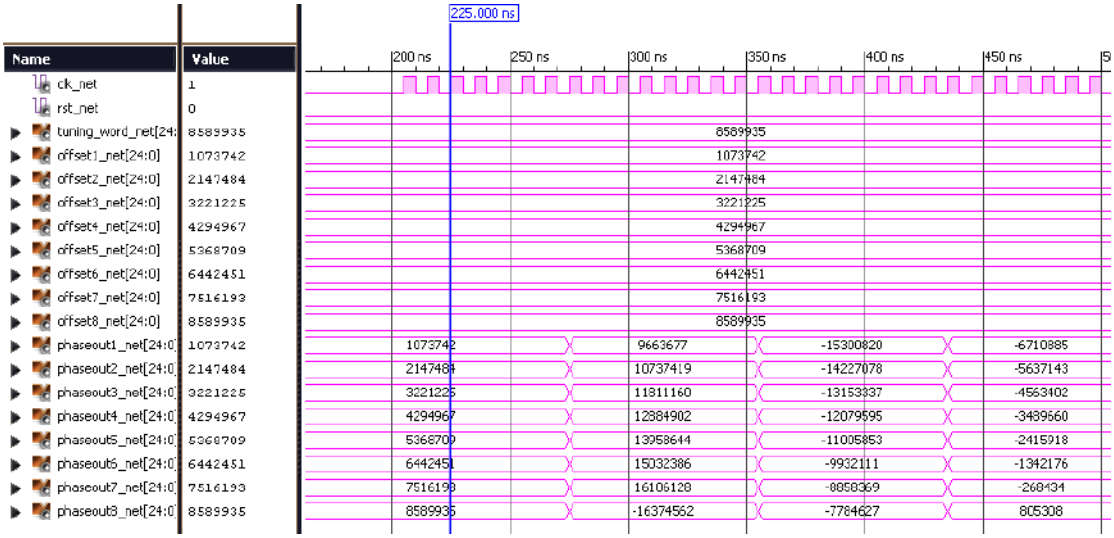

FIGURE 6: SIMULATION RESULTS OF 2 GHZ PHASE ACCUMULATOR (XILINX)

3.3 Implementation results of Single DDS

The figure below shows the bus plot view of single DDS using chipscope.

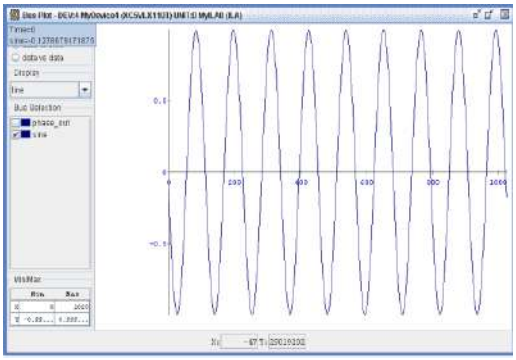

FIGURE 7: SINGLE DDS IMPLEMENTATION USING CHIPSCOPE

IV. CONCLUSION

The RF Transmitter for Magnetic Resonance Imaging (MRI) is designed using 8-Core DDS System by Simulink Block set and Xilinx Block set. The System Generator tool converted the design into Verilog HDL. All these designs are simulated by using Xilinx ISE Simulator and then Synthesized by using Xilinx Synthesis Tool. All these designs are prototyped on Virtex-5 LX110T FPGA board. The RF Transmitter for Magnetic Resonance Imaging (MRI) is designed using 8-Core DDS System by Matlab Simulink Library and System Generator Tool. The design is simulated for functionality by using Xilinx ISE simulator tool.

The synthesized RF Transmitter for Magnetic Resonance Imaging (MRI) using 8-Core DDS System has 1099 LUT slices, 719 slice registers and 2 buffers. Timing analysis results show that the critical path is 3.091 ns i.e., the maximum clock frequency is 323.520MHz. The synthesized RF Transmitter for Magnetic Resonance Imaging (MRI) using 8-Core DDS System was successfully implemented on Xilinx Virtex 5 FPGA.

The RF Transmitter for Magnetic Resonance Imaging (MRI) can be extended to multi-frequency RF Generator. The design can cover the frequency range from 100 KHz to 750MHz.

REFERENCES

[1] Ji Liao, Xiaoming Ye, Xiaoguang Hu and Dan Sun (June 19-21, 2013), "Research and Implementation on Multi-DDS Technology in High Performance Digital Up-conversion", In Industrial Electronics and Applications (ICIEA).

[2] Agilent Technologies (April 11, 2011), "Development of 1-GHz NMR Spectrometer-Collaboration with Bridge12 Technologies on DNP Technology", Retrieved from http://www.agilent.com/about/newsroom/presrel/2011/11apr-ca11027.html

[3] Agilent Technologies, "Waveform Phase Continuity", Retrieved From http://wireless.agilent.com/wireless/helpfiles/n5106a/waveform_phase_contin uity.html

[4] Analog Devices (1999), "A Technical Tutorial on Digital Signal Synthesis", Retrieved from http://www.analog.com/static/importedfiles/tutorials/450968421DDS_Tutorial_rev12-2-99.pdf

[5] Analog Devices (2009), "Datasheet: AD9739, 14 Bit, 2500 MSPS RF DAC", Retrieved from http://www.analog.com/static/importedfiles/data_sheets/AD9739.pdf

[6] Kerr. R.J., Weaver, L.A (1988), "High Resolution Phase-to-Sine Amplitude Conversion", PCT Application Number: PCT/US1988/004622.

[7] Liu, Y., and Li, G. (May 16-18, 2008), "A Microprocessor-Based Nuclear Magnetic Resonance Spectrometer", In International Conference on Bioinformatics and Biomedical Engineering, pp. 2264 – 2265.

[8] Liu, Z., Zhao, C., Zhou, H., and Feng, H. (August 30 - September 3, 2006), "A Novel Digital Magnetic Resonance Imaging Spectrometer", In IEEE Conference on Engineering in Medicine and Biology Society, pp. 280 - 283.

[9] Xilinx (April 28, 2005), "DS246: Logic Core IP DDS v5.0", Retrieved from http://www.xilinx.com/support/documentation/ip_documentation/dds.pdf

[10] Xilinx (April 28, 2005), "DS275: Sine/Cosine Look-Up Table v5.0", Retrieved from http://www.xilinx.com/support/documentation/ip_documentation/sincos.pdf

[11] Xilinx (March 16, 2012),"Virtex 5 User Guide" Retrieved from http://www.xilinx.com/support/documentation/user_guides/ug190.pdf

[12] Xilinx (March, 2008), "System Generator for DSP Reference Guide" Retrieved from www.xilinx.com/support/sw_manuals/sysgen_ref.pdf

[13] Xilinx (April 24, 2012), "System Generator for DSP User Guide" Retrieved from www.xilinx.com/support/documentation/sw_manuals/.../sysgen_user.pdf

AD Publications
Sector-3, MP Nagar, Bikaner,
Rajasthan, India
www.adpublications.org, info@adpublications.org